TECHNISCHE UNIVERSITÄT DRESDEN

Investigation of the AWW kernel for describing the excited meson spectrum in a combined Dyson-Schwinger – Bethe-Salpeter approach

Master Thesis
for the acquisition of the academic degree
Master of Science

submitted by

Robert Greifenhagen
born on August 28$^{\text{th}}$, 1990
in Annaberg-Buchholz

TU Dresden, Institute of Theoretical Physics
and
Institute of Radiation Physics
Helmholtz-Zentrum Dresden - Rossendorf
2016

submitted on November 1st, 2016

Primary Reviewer: Prof. Dr. Burkhardt Kämpfer
Secondary Reviewer: Prof. Dr. Dominik Stöckinger

Zusammenfassung

Im Zusammenhang mit dem Dyson-Schwinger- und Bethe-Salpeter-Ansatz wurde das Spektrum von Mesonen als Bindungszustände der Quantenchromodynamik untersucht. In der vorliegenden Arbeit werden die Ergebnisse für Grundzustandsmassen und die Massen radialer Anregungen von pseudoskalaren- und Vektormesonen präsentiert. Für die Berechnungen wurde das Regenbogen-Leiter-Trunkierungsschema mit einem modellierten Wechselwirkungskern genutzt. Die trunkierte Quark-Dyson-Schwinger-Gleichung und die trunkierte Bethe-Salpeter-Gleichung wurden iterativ im Euklidischen Raum gelöst. Der genutzte Formalismus wurde auf höherenergetische Bindungszustände erweitert, indem die auftretende Pol-Struktur explizit unter Zuhilfenahme von Methoden der Funktionentheorie behandelt wurde. Des weiteren wurden die Zerfallskonstante des Pions, das chirale Kondensat sowie die Regge-Trajektorien der pseudoskalaren Bindungszustände betrachtet. Die Ergebnisse wurden genutzt um Aussagen über den Parameterraum der modellierten Wechselwirkung machen zu können.

Abstract

Within the combined Dyson-Schwinger and Bethe-Salpeter approach the spectrum of mesons as QCD boundstates has been investigated. In this thesis the results for groundstate masses and masses of radially excited states of pseudoscalar and vector mesons are presented. For the explicit calculations the rainbow-ladder truncation scheme has been used with a modelled interaction kernel. The truncated quark Dyson-Schwinger equation and the truncated Bethe-Salpeter equation have been solved iteratively in the Euclidean space. The used formalism has been extended to higher-energy boundstates by treating the arising pole structure explicitly using methods from complex analysis. Further it has been taken a look at the pion decay constant, the chiral condensate and the Regge trajectories of the pseudoscalar boundstates. The results are used to discuss the parameterspace of the model interaction.

Contents

1 | Introduction

For investigating the phenomenas of small particles at high energies it is common to make use of the standard model of particle physics . It is the quantum field theory which describes elementary particles best with the largest coincidence compared to experimental data. It can be divided into the electroweak theory and quantum chromodynamics (QCD). Quantum chromodynamics is the quantum field theory for describing strong interaction phenomena. It was formulated by Gell-Mann, Fritzsch and Leutwyler and can be seen as an analogon to quantum electrodynamics (QED). Instead of leptons and photons QCD contains quarks and gluons and describes the interaction among them. Quarks are fermions which can be divided in three families (analogue to leptons). Each family contains two quarks, which results in six quark flavours: up u, down d, strange s, charm c, bottom b and top t. Furthermore QED is an Abelian gauge theory with symmetry group U(1), while QCD is a non-Abelian gauge theory with symmetry group SU(3), which results in eight gauge bosons, called gluons, and leads to the self interaction of them.

A consequence of the latter is the different behaviour of the running coupling compared to QED. Running coupling means, that the interaction strength depends on the energy scale of the examined processes. In QED the interaction is weak at low energies. In QCD the interaction is weak at large energies, which is known as asymptotic freedom. In that regime processes can be evaluated by perturbation theory very well. For low energies the interaction strength of QCD becomes very large, which results in confinement. It can be visualised in such a manner that the force between quarks rises if one tries to separate them and the energy of the gluon field increases until it is high enough to create a new quark-antiquark pair, so the quarks will never appear free but they are always bound into boundstates.

The boundstates of QCD are called hadrons. They are composite objects containing two or more quarks and anti-quarks, respectively. They can contain three quarks (baryons), three anti-quarks (anti-baryons), one quark and one anti-quark (mesons) or higher numbered combinations of quarks and anti-quarks (exotica, like tetraquarks or pentaquarks). The constituent quarks have the introduced flavours instead of top t, which is to heavy to form observable boundstates. Baryons and mesons can be arranged by their quantum numbers (charge Q, spin S, hypercharge Y, isospin I, ...) and depicted in multiplets, see Fig. 1.1.
In this thesis the interest lies on the boundstate masses of mesons. A common categorisation of mesons is to consider the quantum numbers $J = L + S$ (total angular momentum), P (parity) and C (charge parity), where $J^{PC} = 0^{-+}$ denotes pseudoscalar, $J^{PC} = 0^{++}$ scalar, $J^{PC} = 1^{--}$ vector, $J^{PC} = 1^{+-}$ and $J^{PC} = 1^{++}$ pseudovector and $J^{PC} = 2^{++}$ tensor mesons for all possible combinations with angular momentum $L \in \{0, 1\}$. An overview of experimental values of hadron masses is exhibited in Fig. 1.2.

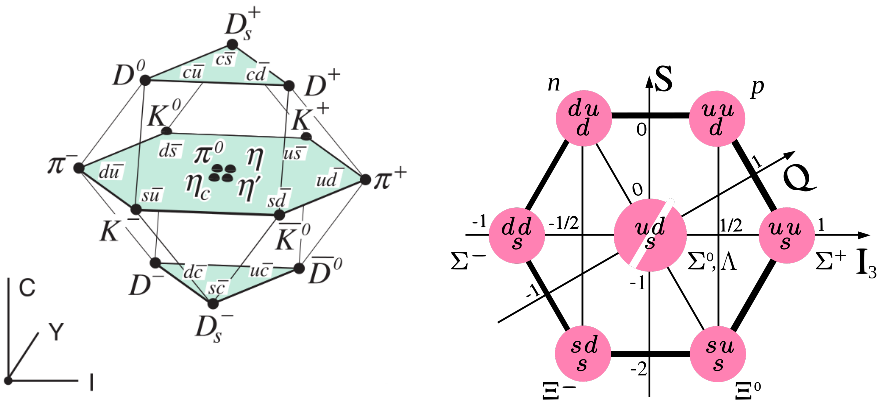

Source: `http://tinyurl.com/zashyop`

(a)

Source: `http://tinyurl.com/jhsk25x`

(b)

Figure 1.1: Hadron multiplets; left panel: multiplet of pseudoscalar mesons containing u, d, s and c quarks. The charmness C denotes the number of c quarks, right panel: baryon octet containing u, d and s quarks. The strangeness S denotes the number of c quarks.

The energy scale of meson boundstates is quite low compared to modern high-energy scattering experiments and the coupling strength is large, related to the strong interaction, which implies that naive perturbation theory is not

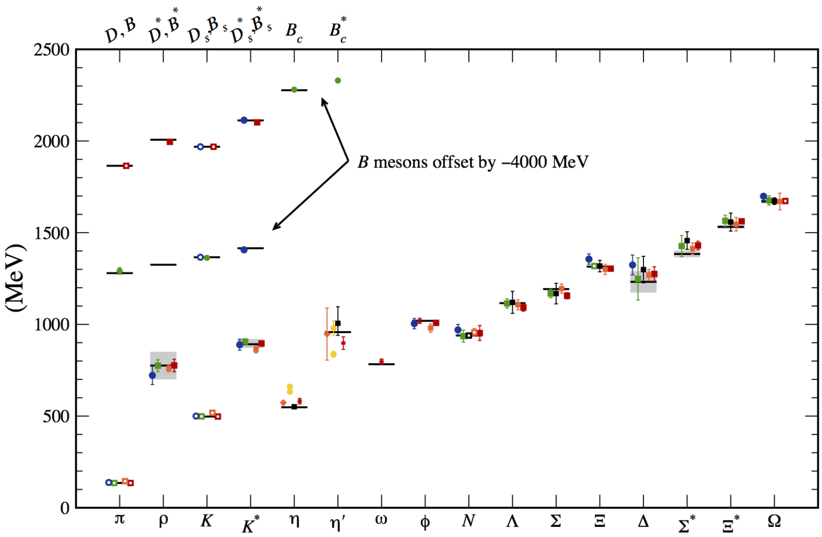

Source: `http://tinyurl.com/hmm43tq`

Figure 1.2: Spectrum of light mesons and baryons. Black bars: experimental values, coloured symbols: different lattice calculations results.

applicable. To describe the spectrum of meson boundstate masses and other properties, like decay constants and form factors, another method must be chosen. A popular non-perturbativ approach is to define and solve quantum chromodynamics on a grid,which is called lattice QCD [11, 19, 24]. It has the disadvantage of losing relativistic covariance and having a huge demand on computer power. Nevertheless it can provide good results, e.g. reproducing experimental hadron masses (see Fig. 1.2).

Another possibility is to use a recursive integral equation for evaluating propagators and interaction amplitudes among quarks and gluons and extracting the meson properties from this quantities. It is made use of a combined consideration of the Dyson-Schwinger equation for quarks and gluons and the Bethe-Salpeter equation for boundstates of two quarks which is also known as the integral approach of QCD. This approach grants relativistic covariance. In the past this approach has been used successful to obtain electromagnetic properties of nuclei, like the deuteron [29, 57], and to reproduce partly the spectrum of known meson masses. The approach is able to generate dynamical masses for describing the relative high constituent quark mass compared to their bare masses and it can describe pions in a correct way, which are much lighter than the sum of two constituent quarks. It means that this integral approach includes another effect of the strong interaction very well, the dynamical chiral symmetry breaking (DCSB), which has been modeled, e.g. by the linear sigma model.

Unfortunately inside this integral approach a couple of additional approximations have to be done to solve the infinite number of recursive steps. This approximations must guarantee that the integral equations produce results with good accuracy after a few steps. Usually the full integral equations were truncated at any point and this truncated Dyson-Schwinger and Bethe-Salpeter equations are evaluated by a model interaction. A common truncation scheme is the rainbow-ladder truncation, used in many models [2, 6, 40, 46, 49]. This parameter dependent models provide a quite good description of masses and decay constants of several pseudoscalar and vector meson groundstates compared to experimental values. Unfortunately the spectrum of radially excited boundstates does not coincide with the experimental data. It also turned out that within this models the propagators of the quarks have a non-physical pole structure, which limits the evaluation of the spectrum of meson masses by a maximal value. There are already some attempts made to bypass this pole structure and make predictions for higher meson boundstates [4, 34]. One goal of this thesis is to handle this pole structure explicitly to evaluate the higher meson boundstates directly. This seems to be possible by using methods from complex analysis and first progress was made in [10]. In this thesis emphasis lies on the model of R. Alkofer and his colleagues [2]. The model they used is simple compared to the other models [6,40,46,49] and it seems to be outmoded for doing meson spectroscopy with high accuracy. Otherwise this model provides a couple of advantages concerning the technical implementation of finding meson observables and handling the pole structure. Further, the results of the groups who used this interaction model [2, 6] seem to be very exemplary for certain points in the four-dimensional parameter space of this model. So the second goal of this thesis is, to go systematically through this parameter space to give a better overview over the found meson spectrum.

In the second chapter the Dyson-Schwinger equations, the Bethe-Salpeter equation, the truncation scheme and the used interaction model are introduced. Further a few comments about Regge trajectories are made. In the third chapter the technical details for evaluating iterative the truncated Dyson-Schwinger equation are discussed. It is shown how the pole structure of the propagator functions could be found. The truncated Bethe-Salpeter equation is expanded into a few series and it is explained how the meson masses can be extracted without the necessity of finding the Bethe-Salpeter amplitudes. Further a parametrisation is introduced to bring the truncated Bethe-Salpeter equation in a convenient form for handling the quark propagator pole structure and it is explained how to do latter. In the fourth chapter the resulting meson spectrum of pseudoscalar and vector mesons containing u, d, s and c quarks has been compared to the results of other groups. Mesons containing b quarks have been neglected, because in this thesis the mesons including c quarks, $D, D_s, \eta_c, D^*, D_s^*$ and J/ψ, are representative for the problematic of describing light, heavy and heavy-light mesons within the same interaction model. The results have been tested on the independence of the numerical parameters. Then the model parameters have been systematically varied to see how the meson observables change and to find optimal sets of parameters for different condition. The obtained meson spectrum has been analysed in sense of finding Regge type behaviour, a principle of ordering eigenstates of a quantum system with its origin in string theory. Beside meson masses the pion decay constant and the chiral condensate for massless quarks have been calculated. At last the constraints of the applied approximations and methods are discussed and an outlook to improve them is given.

2 | Dyson-Schwinger and Bethe-Salpeter approach

2.1 The quark Dyson-Schwinger equation

The Dyson-Schwinger equations [1] (DSEs) are a couple of integral equations, which can be seen as the integral formulation in equivalence to full quantum chromodynamics. They connect the Green's functions of the QCD and give expressions for the dressed quark propagator S, the dressed gluon propagator $\mathcal{D}_{\mu\nu}$, the quark-gluon vertex Γ^μ and, if needed, the ghost propagator and vertices. Furthermore, two more equations exist for the gluon self-interaction, one for the three-point function and one for the four-point function. QCD as a non-Abelian gauge theory is treated with ghost fields c^a, which couple to the gluon. Therefore two more Dyson-Schwinger equations appear, one for the ghost propagator and one for the ghost-gluon vertex [54].

In the end there are seven integral equations to solve and each expression is connected to each other expression of them, which results in an infinite tower of integral equations. To reach a solvable form it is inevitable till now to cut this expressions at a suitable point and do so called truncations.

In this thesis we are going to find a solution of the dressed quark propagator S. The Dyson-Schwinger equation reads

$$S^{-1}(p) \;=\; S_0^{-1}(p) - \int \frac{d^4k}{(2\pi)^4}[-ig\gamma^\nu \frac{\tau^a}{2}]\mathcal{D}_{\mu\nu}(p,k)\Gamma^{\mu,a}(p,k)S(k), \qquad (2.1)$$

where S_0 is the undressed quark propagator, γ^ν are the Dirac matrices with $\{\gamma^\mu, \gamma^\nu\} = 2g^{\mu\nu}$, τ^a are colour matrices, p and k are four-momenta and g is

[1] The Dyson-Schwinger equations have been introduced by F. Dyson and J. Schwinger [12, 51, 52]; surveys can be found in [1, 48].

the QCD coupling constant. An illustration of Eq. (2.1) is shown in Fig. 2.1. For solving this equation, expressions for $\mathcal{D}_{\mu\nu}$ and Γ^μ have to be specified.

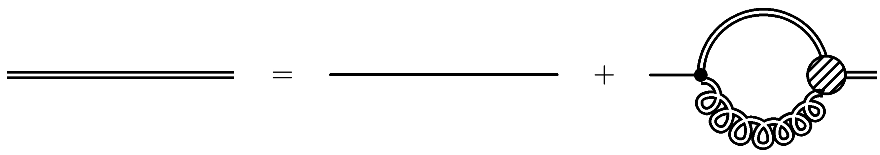

Figure 2.1: Diagrammatic representation of the quark Dyson-Schwinger equation. Double lines represent dressed propagators, single lines are undressed propagators. The vertex with the shaded blob is a dressed quark-gluon vertex and the black dot is an undressed one.

First the so called rainbow truncation [41] is applied

$$\Gamma^{\mu,a}(p,k) \Rightarrow -ig\gamma^\mu \frac{\tau^a}{2}. \tag{2.2}$$

To illustrate the nomenclature of this approximation it is useful to insert Eq. (2.1) iterative into itself. The resulting Feynman diagrams look like rainbows, if the fermion is drawn as a straight line (i.e. all Feynman diagrams with crossing gluon lines vanish). The rainbow approximation is applicable for processes with low energy. Concerning $q\bar{q}$ boundstates with masses smaller than 4 GeV this approximation is supposed to work. However, there are also significant problems associated with the rainbow approximation, like the loss of gauge covariance and the appearance of an unphysical singularity structure in the solution of the quark propagators [48]. The last one takes up an important role in this thesis and is considered more in detail below.

Secondly, the gluon propagator can be written as [48]

$$g^2\mathcal{D}_{\mu\nu}(k) = \left(g_{\mu\nu} - \frac{k_\mu k_\nu}{k^2}\right) D(k^2) + \alpha \frac{k_\mu k_\nu}{k^4}, \tag{2.3}$$

where $D(k^2) = 1/(k^2[1+\Pi(k^2)])$ is the scalar kernel function with the gluon self-energy $\Pi(k^2)$ and α is the gauge parameter. In this thesis $\alpha = 0$, so called Landau gauge, is chosen, because it is argued that the calculations in this thesis are numerically reliable in this gauge [20]. The resulting truncated Dyson-Schwinger equation (tDSE) for the quark propagator reads [9]

$$S^{-1}(p) = S_0^{-1}(p) \; + \; \frac{4}{3}\int \frac{d^4k}{(2\pi)^4}[g^2\mathcal{D}_{\mu\nu}(p-k)]\gamma^\mu S(k)\gamma^\nu \tag{2.4}$$

with the undressed quark propagator

$$S_0^{-1}(p) = \not{p} \; + \; m. \tag{2.5}$$

The summation over the colour matrices contributes with the Casimir factor $C_F = 4/3$ for number of colours $N_C = 3$ [48], m is the current quark mass (also called naked quark mass or bare quark mass) and $\not{p}$ denotes $\gamma^\mu p_\mu$. Eq. (2.5) is often denoted by gap equation. An illustration of the truncated Dyson-Schwinger equation is shown in Fig. 2.2.

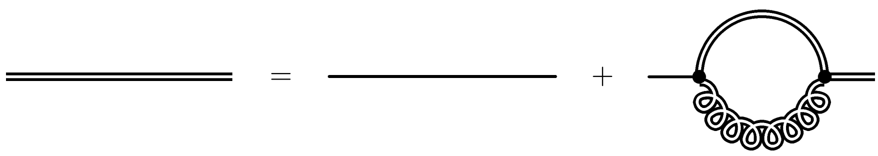

Figure 2.2: Diagrammatic representation for the truncated quark Dyson-Schwinger equation in rainbow approximation. Line codes as in Fig. 2.1.

2.2 Bethe-Salpeter equation for mesons

To find the mass of a quark-antiquark boundstate it is necessary to solve the Bethe-Salpeter equation [2] (BSE). In Minkowski space the homogeneous BSE has the general form [25]

$$\Gamma(P,p) = i\int \frac{d^4k}{(2\pi)^4}K(P,p,k)S(k_1)\Gamma(P,k)S(k_2), \tag{2.6}$$

[2] The Bethe-Salpeter equation has been introduced in [50] to formulate an approach to relativistic two-body boundstates (The relativistic three-body problem is dealt with the Faddeev equation [14]). It has been first used for mesons in [5]. It has been successfully used for describing e.g. the properties of deuteron [29, 57]. For a survey see [42].

where $\Gamma(P,p)$ is the Bethe-Salpeter vertex function, $K(P,p,k)$ is the interaction kernel and $S(k)$ is the quark propagator from Eq. (2.5). k_1 and k_2 are the quark momenta; the total momentum P and the relative momentum k are defined by $P = k_1 + k_2$ and $k = (k_1 - k_2)/2$.

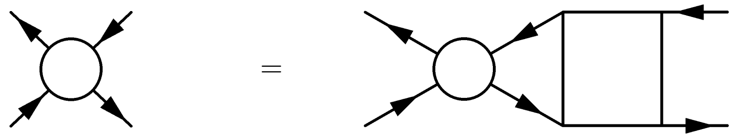

Figure 2.3: Diagrammatic representation of the homogeneous Bethe-Salpeter Eq. (2.6). The blob is the Bethe-Salpeter vertex function $\Gamma(P,p)$ and the rectangle is the interaction kernel $K(P,p,k)$.

In Fig. 2.3 the corresponding diagrammatic illustrations are exhibited.

For solving the Dyson-Schwinger equation and the Bethe-Salpeter equation in a consistent manner for both the same interaction model with the same truncations has to be used [47]. The introduced rainbow truncation (2.2) implies the ladder approximation, justified by the manifestation of the Goldstone theorem [3]. The rainbow-ladder truncation is consistent with the axial-vector Ward-Takahashi identity (AVWTI) [39], which gives a relation between the vertex functions Γ and the quark propagator S. Practically it means that the interaction of the two quarks in the diquark boundstate is approximated by an infinite number of one-gluon exchanges. The interaction kernel $K(P,p,k)$ in rainbow-ladder truncation reads [39]

$$K(P,p,k) = -g^2 \mathcal{D}_{\mu\nu}(p-k)\Big(\gamma^\mu \frac{\tau^a}{2}\Big)\Big(\gamma^\nu \frac{\tau^a}{2}\Big), \tag{2.7}$$

where τ^a are colour matrices and $g^2\mathcal{D}_{\mu\nu}(p-k)$ is given in Eq. (2.3). An illustration of the first three Feynman diagrams which contribute to the interaction kernel in rainbow-ladder truncation is shown in Fig. 2.4; in Fig. 2.5 two examples for Feynman diagrams which do not contribute in rainbow-ladder truncation are displayed.

For solving the truncated Bethe-Salpeter equation (tBSE) it is useful to switch from Minkowski space to the Euclidean space, because common approaches for the interaction kernel are formulated in Euclidean space [2, 40,

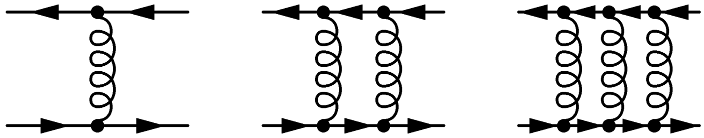

Figure 2.4: A few Feynman diagrams which contribute to the interaction kernel within the rainbow-ladder approximation.

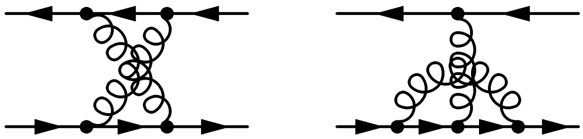

Figure 2.5: Feynman diagrams which do not contribute to the interaction kernel within the rainbow-ladder approximation.

46]. After using the simple transition rules from Appendix C and summing up over all colour matrices the tBSE in the Euclidean space reads [10, 20]

$$\Gamma(P,p) = -\frac{4}{3}\int \frac{d^4k}{(2\pi)^4}\gamma^\mu S(k_1)\Gamma(P,k)S(k_2)\gamma^\nu[g^2\mathcal{D}_{\mu\nu}(p-k)]. \tag{2.8}$$

The summation over the colour matrices again contributes with the Casimir factor $C_F = 4/3$. For solving both, the tDSE and the tBSE, the kernel $D(k^2)$ has to be specified. A common and often used one is introduced in [40], the so called Maris-Tandy (MT) kernel,

$$D^{\mathrm{MT}}(k^2) = \left(\frac{4\pi^2 Dk^2}{\omega^2}e^{-\frac{k^2}{\omega^2}} + \frac{8\pi^2\gamma_m F(k^2)}{\ln[\tau + (1+\frac{k^2}{\Lambda^2_{\mathrm{QCD}}})^2]}\right), \tag{2.9}$$

where D is a parameter for the interaction strength, ω is a parameter for the interaction range, $\gamma_m = 12/(33-2N_f)$, N_f is the number of quark flavours, $\tau = e^2 - 1$, $F(k^2) = [1 - exp(-k^2/[4m_t^2])]/k^2$ and the chosen values of the parameters are $m_t = 0.5\,\mathrm{GeV}$, $N_f = 4$ and $\Lambda_{\mathrm{QCD}} = 0.234\,\mathrm{GeV}$. This kernel contains two terms. The first term is called infrared (IR) term and gives the main contribution for small values of k up to 2 GeV. It is a model term which is discussed explicitly in [40]. The second term is called ultraviolet (UV) term and contains the exact contribution for large momenta k, calculated in perturbation theory at one-loop order. Anyway, it is argued that this UV term does not contribute too much to the observables of boundstates. Within the introduced rainbow approximation the focus is already located on the low energy scale, where the UV term is less important. It seems possible to neglect this term, which provides a few advantages in the subsequent calculations of this thesis. Integrals related to the IR part converge rather fast for large momenta k and the necessity of a cutoff of the momentum integration vanishes. Further, the logarithm in the nominator of the UV term can lead to additional singularities when calculations are shifted to the complex momentum space. The IR part of the MT kernel is known as Alkofer-Watson-Weigel (AWW) kernel, introduced and used in [2]:

$$D^{\mathrm{AWW}}(k^2) = \frac{4\pi^2 D k^2}{\omega^2} e^{-\frac{k^2}{\omega^2}}. \tag{2.10}$$

This kernel is used for the calculations in this work and has to be inserted into Eq. (2.3); It provides several numerical advantages (e.g. expansion in a series of harmonics) and is used by several groups [2, 6]. An illustration of the kernels 2.9 and 2.10 is given in Appendix A.

For avoiding misunderstandings here are a few words about the notion "kernel". In principle it comes from the type of integral equation which has to be solved. For the Fredholm type tDSE (2.5) the kernel would be the combination of $g^2\mathcal{D}_{\mu\nu}(p-k)$ and the Dirac matrices γ^μ and γ^ν, for the Fredholm type tBSE the kernel would be the same plus additional the two propagators $S(k_1)$ and $S(k_2)$. According to the nomenclature of [40] the scalar kernel functions (2.9) and (2.10) are called kernel till the end of this thesis.

2.3 Regge behaviour

Regge behaviour is a property of the eigenstates of a quantum system. They have this property, if the eigenstates are located on a so called Regge trajectory,

$$M(J)^2 = M^2(0) + \beta J, \tag{2.11}$$

where J is the quantum number of the angular momentum of the boundstate, $M(0)$ the groundstate mass and β the constant slope of the Regge trajectory. Following the particle data group (PDG) nomenclature [44], hadrons are characterised, besides masses M, by J^{PC}, with $P = \pm 1$ as parity and $C = \pm 1$

as charge parity. For mesons in direction of J within the MT model (2.9) Regge behaviour is explored in [34] with emphasis on light mesons ($u\overline{u}$, $u\overline{s}$ and $s\overline{s}$ boundstates).
In the present thesis the Regge behaviour in radial direction is considered for pseudoscalar mesons, where at least three eigenstates could be found. The Regge trajectory for radially excited meson boundstate has been introduced e.g. in [13] with a few comments on its origin in string theory.

3 | Numerical Implementation

3.1 Solving the Dyson-Schwinger equation

The techniques used for this thesis can be found very detailed in [9]; the main steps and some extensions are introduced in this section.

3.1.1 Solution on the positive real axis

The dressed quark propagator S depends on two functions, the renormalisation constant Z and the self-energy $\Sigma(p)$. Instead of these functions the propagator can be expressed via two other functions $A(p)$ and $B(p)$ or alternatively $\sigma_s(p)$ and $\sigma_v(p)$. With these quantities the dressed propagator reads [38]

$$\begin{aligned} S^{-1}(p) &= \quad i\not{p}A(p) &+ B(p), \\ S(p) &= - \; i\not{p}\sigma_v(p) &+ \sigma_s(p), \end{aligned} \tag{3.1}$$

where the propagator functions $\sigma_v(p)$ and $\sigma_s(p)$ are related to the functions $A(p)$ and $B(p)$ via

$$\begin{aligned} \sigma_v(p) &= \frac{A(p)}{p^2A^2(p)+B^2(p)}, \\ \sigma_s(p) &= \frac{B(p)}{p^2A^2(p)+B^2(p)}. \end{aligned} \tag{3.2}$$

Inserting Eq. (3.1) and the kernel (2.10) into Eq. (2.5), taking once directly the trace and twice multiplying with $\not{p}/p$ and executing then the trace it results the following coupled system of equations:

$$\begin{aligned} pA(p) &= p \quad + \iint \frac{dkk^3}{3\pi^3} dt \sqrt{1-t^2} D(p,k,t) \frac{kA(k)}{k^2A^2(k)+B^2(k)} \\ &\qquad \times \left(t + 2\frac{(p-kt)(pt-k)}{p^2+k^2-2pkt} \right), \\ B(p) &= m_q \quad + \iint \frac{dkk^3}{\pi^3} dt \sqrt{1-t^2} D(p,k,t) \frac{B(k)}{k^2A^2(k)+B^2(k)}, \end{aligned} \tag{3.3}$$

where m_q is the current quark mass and $D(p,k,t)$ is defined in Eq. (2.10) and has the argument p^2+k^2-2pkt with the hyperangle $t = cos(\chi_{pk})$. The propagator functions do not depend on the hyperangle so the integration over t can be done numerically without problems and two one-dimensional integral equations remain. They can be solved numerically by an iteration method, which turned out to converge rather fast with practically no dependence on the choice of the trial start functions $A(p)$ and $B(p)$. The three independent parameters are m_q, ω and D. The solutions of the tDSE $A(p)$ and $B(p)$ are smooth, positive and finite functions, where $A(p)$ converges to 1 and $B(p)$ converges to m_q for $p \to \infty$. In Appendix E the propagator functions of Eq. (3.1) are exemplary shown for $\omega = 0.5\,\mathrm{GeV}$, $D = 16\,\mathrm{GeV}^{-2}$ and several quark masses m_q.

3.1.2 Solution in the complex plane

In the previous section the propagator functions have been found for positive real momenta p. From Eq. (2.6) it can be seen that the integration domain, where the propagator functions are needed, is bounded by a parabola and k_1 and k_2 in Euclidean space read

$$\tilde{k}^2_{1/2} = \tilde{k}^2 - \eta^2_{1,2} M^2_{q\bar{q}} \pm 2i\eta_{1,2} M_{q\bar{q}} \tilde{k} \cos\chi, \tag{3.4}$$

where $\eta_{1,2}$ is the momentum partitioning parameter with $\eta_1 + \eta_2 = 1$) and $\tilde{k}$ is the modulus of an Euclidean four-vector $k^E = (k_4, \vec{k})$ with $\tilde{k} = \sqrt{k_4^2 + \vec{k}^2}$. Therefore the propagator functions (3.1) must be found for complex arguments. Different methods exist for evaluating the tDSE in the whole complex plane [26]. Here, a selection is listed, but only the relevant ones which are

needed in this thesis are precisely described.
The most straight forward way is to use the method introduced in [2], called "brute force". In Eq. (3.3) the propagator functions $A(k)$ and $B(k)$ on the right side only depend on the real internal (under the integral) momentum k. It follows that for complex arguments p the real solutions of $A(p)$ and $B(p)$ can be used to solve Eq. (3.3) everywhere in the complex plane. Although this method seems to provide the propagator functions everywhere in a simple way it has some disadvantages. First it works only for kernels with an innocent structure like the AWW kernel (2.10). The full MT kernel (2.9) is an example where the "brute force" method does not work at all in the complex plane (see Appendix A). However, in this thesis calculations are restricted to the AWW kernel. Secondly, if the imaginary part of the argument p becomes too large, the numerical integration gets worse caused by oscillations of the integrand. The oscillating term is located in the kernel (2.10) and is studied more closely in Appendix B. Thirdly, the method includes two numerical integrations, which costs some computing time. Especially for the mentioned problem with higher imaginary parts of the arguments the accuracy of the calculation has to be improved, which means that the number of mesh points increases continuous, see again Appendix B.

A method for finding the solution of the propagator functions in the complex plane is to solve Eq. (3.3) once along a closed contour $\mathcal{C}$ with the "brute force" method and then using Cauchy's theorem

$$A(z) = \frac{1}{2\pi i} \oint_{\mathcal{C}} \frac{A(\xi)}{\xi - z} d\xi \tag{3.5}$$

to calculate the needed quantities at any point inside this contour [17]. Compared to Eq. (3.3) this method is practically reduced by one numerical integration and therefore much faster than the "brute force" method. The initialising computation on the contour $\mathcal{C}$ is negligibly short if the number of evaluated points inside the contour is adequately high. The contour is shown in Fig. 3.1 (violet parabola with vertical boarder), the numerical integration is done with a mapped Gaussian mesh; the number of integration points on each branch and on the vertical line depend on the size of the contour $\mathcal{C}$.

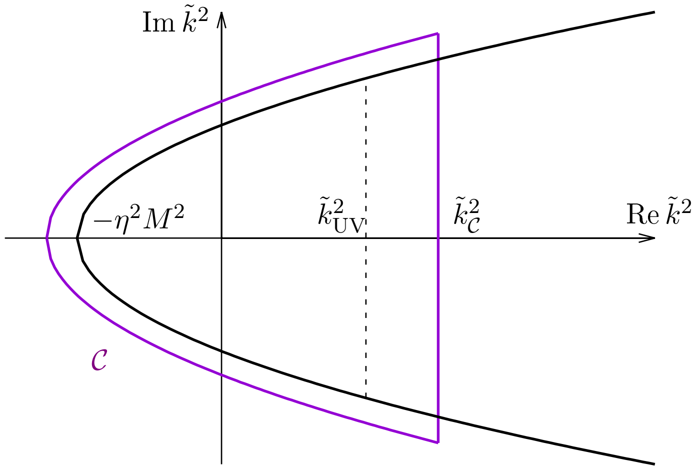

Figure 3.1: Integration domain of the tBSE (2.8) in the complex $\tilde{k}^2$ plane in Euclidean space (black parabola, compare Eq. (3.4)). For momenta smaller than $\tilde{k}^2_{\mathrm{UV}}$ Cauchy's theorem (3.5) is applied using the violet parabolic contour. For momenta larger than $\tilde{k}^2_{\mathrm{UV}}$ the parametrisation (3.6) is used.

Another possibility to determine the propagator functions in the complex plane is to use a parametrisation. If an appropriate choice of such a parametrisation is found, the solution on the real axis will be fitted to it with a suitable algorithm and then the fit can be used to find the solution for complex arguments. Of course, such a fit can not reflect the exact analytically continuation. But it has been found that for "good fit functions" and moderately large imaginary parts the fitted results are almost identical with the values found with the "brute force" method. To improve the quality of the parametrisation in the deep complex plane (for larger imaginary parts) it is useful to use not only the solution on the real axis for fitting, but also several points in the complex domain, where the fit will be applied.

One advantage of such a fit is, to avoid the above mentioned oscillations (Appendix B). As seen from Eq. (3.4) for larger values of $\tilde{k}$ the imaginary part of $\tilde{k}_{1/2}$ raises linearly and it is inevitable to use a convenient fit function. For smaller values of $\tilde{k}$ where $\mathrm{Re}(\tilde{k}_{1/2}) \leq 0$ it is useful to use the Cauchy's theorem method with a parabolic contour like the one exhibited in Fig. 3.1.

In this thesis the parametrisation function is chosen as in [53]:

$$\sigma_\kappa(\tilde{k}^2) = \sum_i^3 \Big(\frac{\alpha_i(\kappa)}{\tilde{k}^2 + \beta_i^2(\kappa)} + \frac{\alpha_i^*(\kappa)}{\tilde{k}^2 + \beta_i^{*2}(\kappa)} \Big), \tag{3.6}$$

where $\kappa \in [s, v]$ and α_i and β_i^2 are complex parameters. In contrast to [53], each of the propagator functions $\sigma_{s,v}(\tilde{k}^2)$ has its own set of parameters. The number of parameters is the same as in [53], but in principle chosen at will. Only using two of each parameters α_i and β_i seems to be insufficient. With three parameters the reproduced propagator functions are precise enough for the necessary subsequent calculations in the tBSE. An advantage of this parametrisation is that it reflects the homogeneity regarding to the complex conjugation of the propagator functions $\sigma_{s,v}(p)$ by definition, i.e. the property $\sigma_{s,v}(z^*) = \sigma_{s,v}^*(z)$. Another important fact is that this fitting structure can be used to do all angular integrations in the tBSE analytically as will be shown below.

3.1.3 Appearance of poles

To make use of Eq. (3.5) the necessary function must be analytically everywhere inside the integration contour $\mathcal{C}$. To check this the Cauchy integral

$$\frac{1}{2\pi i} \oint_{\mathcal{C}} A(p^2) dp^2 \tag{3.7}$$

is used. If $A(p^2)$ is analytically, the contour integral (3.7) must be zero. Calculations of $\sigma_s(p^2)$ and $\sigma_v(p^2)$ for certain model parameters ω and D and quark mass parameters m_q had shown that, depending on the integration contour $\mathcal{C}$, the Cauchy integral is zero or not, and if not it has discrete values. This indicates the appearance of poles in the propagator functions, hence $[p^2 A^2(p^2) + B^2(p^2)]$ becomes zero at certain points p_i^2. Expression (3.7) can be written as

$$\frac{1}{2\pi i} \oint_{\mathcal{C}} \sigma_{s/v}(p^2) dp^2 \;=\; \sum_i^{N_{\text{poles}}} \text{res}[\sigma_{s/v}(p_i^2)] \tag{3.8}$$

and, if the positions of the singularities are precisely known, Eq. (3.5) can be rewritten as

$$\sigma_{s/v}(k^2) = \frac{1}{2\pi i}\oint_{\mathcal{C}} \frac{\sigma_{s/v}(p^2)}{p^2-k^2}dp^2 + \sum_{i}^{N_{\text{poles}}} \frac{\text{res}[\sigma_{s/v}(p_i^2)]}{k^2-p_i^2} \tag{3.9}$$

$$= \tilde{\sigma}_{s/v}(k^2) + \sum_{i}^{N_{\text{poles}}} \frac{\text{res}[\sigma_{s/v}(p_i^2)]}{k^2-p_i^2}, \tag{3.10}$$

where $\tilde{\sigma}_{s/v}(k^2)$ is an analytical function and $\text{res}[\sigma_{s/v}(p_i^2)]$ is the residue of $\sigma_{s/v}(p^2)$ at $p^2 = p_i^2$. The sums are over all poles inside the integration contour and vanish automatically if no singularities are located inside.
To locate the poles numerically exactly it is useful to apply the argument principle of complex analysis (also referred as Rouché's integral [9, 10]),

$$\frac{1}{2\pi i}\oint_{\mathcal{C}} \frac{f'(z)}{f(z)}dz = N_Z - N_{\text{poles}}, \tag{3.11}$$

where N_{poles} is the number of poles and N_Z the number of roots. If the function $f(p^2) = [p^2A^2(p^2) + B^2(p^2)]$ is analytically everywhere inside the integration contour $\mathcal{C}$, which can be checked with

$$\oint_{\mathcal{C}} [p^2A^2(p^2) + B^2(p^2)]dp^2 = 0, \tag{3.12}$$

the number of poles N_{poles} is zero and only N_Z remains.
Eq. (3.8), (3.9) and (3.11) can be evaluated for any closed contour $\mathcal{C}$ and, if Rouché's integral is nonzero, this contour can be systematically scaled down. The procedure has been described in [9, 10, 26]. Worth to mention is that all poles are located in the region $\text{Re}(p^2) < 0$. This can be shown by rotating the integration variable k of the system of equations (3.3) with a phase $e^{i\phi}$ where $\phi \in [-\pi/2, \pi/2]$ (see [9, 26]).

With Eq. (3.4), the parabolic integration domain of the tBSE is specified. After finding the first poles $\tilde{k}_{0,i}^2$ with the introduced procedure they can be inserted in Eq. (3.4) to find the corresponding parabolas

$$\tilde{k}_{0,i}^2 = \tilde{k}^2 - \chi_i^2 \pm 2i\chi_i\tilde{k}, \tag{3.13}$$

where $\chi_i = M_{q\bar{q}}\eta_i$ with the partitioning parameter η_i of quark q_i, $i \in \{1,2\}$. That means Eq. (3.13) describes the parabola on which the pole $\tilde{k}^2_{0,i}$ is located. Comparing Eq. (3.4) and (3.13) leads to an upper limit for the product $\eta M_{q\bar{q}}$. That means, to make sure that the propagator functions $\sigma_s(p^2)$ and $\sigma_v(p^2)$ are analytically everywhere inside the integration region of the tBSE, the lowest $\chi_i \equiv \chi$ has to be found and then η and $M_{q\bar{q}}$ must be chosen in such a way that

$$\eta M_{q\bar{q}} \;\leq\; \chi. \tag{3.14}$$

The quantity χ_i of a pole $\tilde{k}^2_{0,i}$ can be calculated by

$$\chi_i = \sqrt{-\frac{\mathrm{Re}(\tilde{k}^2_{0,i})}{2} + \sqrt{\left(\frac{\mathrm{Re}(\tilde{k}^2_{0,i})}{2}\right)^2 + \left(\frac{\mathrm{Im}(\tilde{k}^2_{0,i})}{2}\right)^2}}. \tag{3.15}$$

Worth to mention is that each pole of $\sigma_s(p^2)$ and $\sigma_v(p^2)$ in the complex plane arises as pair of poles, i.e. if $\tilde{k}^2_{0,i}$ is a pole, than $\tilde{k}^{2*}_{0,i}$ is a pole, too, due to the fact that $\sigma_{s,v}(p^{2*}) = \sigma^*_{s,v}(p^2)$.

3.2 Solving the Bethe-Salpeter equation

In general the solving procedure for the tBSE of this thesis follows mainly [10]; the main steps with some important details and some necessary extensions are introduced in this section.

3.2.1 Spin-angular harmonics

The Bethe-Salpeter vertex functions Γ, introduced in Eq. (2.6), are 4×4 matrices in Dirac space. For spinor particles the general structure of them for boundstates has been investigated, for example, in [33]. So the vertex function Γ can be expanded into so called spin-angular harmonics, i.e. functions which are determined by parity and angular momentum of the corresponding meson [10]:

$$\Gamma(p) = \sum_\alpha \Gamma_\alpha(p) = \sum_\alpha g_\alpha(p)\,\mathcal{T}_\alpha(\vec{p}). \tag{3.16}$$

The functions g_α fulfil the orthogonality relation

$$g_\alpha(p) = \int d\Omega_{\vec{p}} \ \mathrm{Tr}[\,\Gamma(p)\mathcal{T}^\dagger_\alpha(\vec{p})\,]. \tag{3.17}$$

For pseudoscalar mesons ($J^{PC} = 0^{-+}$), the number of independent spin-angular harmonics α_{max} is reduced to four and the set is chosen as [10]

$$\begin{aligned}
\mathcal{T}_1(\vec{p}) &= \frac{1}{\sqrt{16\pi}}\gamma^5 &&= && \mathcal{T}^\dagger_1(\vec{p}),\\
\mathcal{T}_2(\vec{p}) &= \frac{1}{\sqrt{16\pi}}\gamma^0\gamma^5 &&= - && \mathcal{T}^\dagger_2(\vec{p}),\\
\mathcal{T}_3(\vec{p}) &= -\frac{1}{\sqrt{16\pi}}\not{n}_{\vec{p}}\gamma^0\gamma^5 &&= && \mathcal{T}^\dagger_3(\vec{p}),\\
\mathcal{T}_4(\vec{p}) &= -\frac{1}{\sqrt{16\pi}}\not{n}_{\vec{p}}\gamma^5 &&= && \mathcal{T}^\dagger_4(\vec{p}),
\end{aligned} \tag{3.18}$$

and for vector mesons ($J^{PC} = 1^{--}$, α_{max} is reduced to eight)

$$\begin{aligned}
\mathcal{T}_1(\vec{p}) &= \sqrt{\frac{1}{16\pi}}\not{\xi}_{\mathcal{M}} &&= - && \mathcal{T}^\dagger_1(\vec{p}),\\
\mathcal{T}_2(\vec{p}) &= -\sqrt{\frac{1}{16\pi}}\gamma^0\not{\xi}_{\mathcal{M}} &&= && \mathcal{T}^\dagger_2(\vec{p}),\\
\mathcal{T}_3(\vec{p}) &= -\sqrt{\frac{3}{16\pi}}(n_{\vec{p}}\,\xi_{\mathcal{M}}) &&= && \mathcal{T}^\dagger_3(\vec{p}),\\
\mathcal{T}_4(\vec{p}) &= \sqrt{\frac{3}{32\pi}}\gamma^0[-(n_{\vec{p}}\xi_{\mathcal{M}}) + \not{n}_{\vec{p}}\not{\xi}_{\mathcal{M}}] &&= - && \mathcal{T}^\dagger_4(\vec{p}),\\
\mathcal{T}_5(\vec{p}) &= \sqrt{\frac{1}{32\pi}}[\not{\xi}_{\mathcal{M}} + 3(n_{\vec{p}}\,\xi_{\mathcal{M}})\not{n}_{\vec{p}}] &&= - && \mathcal{T}^\dagger_5(\vec{p}),\\
\mathcal{T}_6(\vec{p}) &= \sqrt{\frac{1}{32\pi}}\gamma^0[\not{\xi}_{\mathcal{M}} + 3(n_{\vec{p}}\,\xi_{\mathcal{M}})\not{n}_{\vec{p}}] &&= && \mathcal{T}^\dagger_6(\vec{p}),\\
\mathcal{T}_7(\vec{p}) &= -\sqrt{\frac{3}{16\pi}}\gamma^0(n_{\vec{p}}\,\xi_{\mathcal{M}}) &&= && \mathcal{T}^\dagger_7(\vec{p}),\\
\mathcal{T}_8(\vec{p}) &= \sqrt{\frac{3}{32\pi}}[-(n_{\vec{p}}\,\xi_{\mathcal{M}}) + \not{n}_{\vec{p}}\not{\xi}_{\mathcal{M}}] &&= - && \mathcal{T}^\dagger_8(\vec{p}).
\end{aligned} \tag{3.19}$$

All the scalar products are written here in Minkowski space; $n_{\vec{p}}$ is the unit vector defined as $n_{\vec{p}} = (0, \vec{p}/|\vec{p}|)$, $\xi_{\mathcal{M}}$ is the polarisation vector $\xi_{\mathcal{M}} = (0, \vec{\xi_{\mathcal{M}}})$ fixed by $\vec{\xi}_{+1} = -(1, i, 0)/\sqrt{2}$, $\vec{\xi}_{-1} = (1, -i, 0)/\sqrt{2}$, $\vec{\xi_0} = (0, 0, 1)$ and slashed quantities $\not{x}$ represent $\gamma^\mu x_\mu$.

3.2.2 The hyperspherical decomposition

For reducing the dimension of the integral in Eq. (2.8) the partial amplitudes $\Gamma_\alpha(p)$ and the interaction kernel (2.10) are decomposed over the basis of spherical harmonics $Y_{lm}(\theta,\phi)$ and normalised Gegenbauer polynomials $X_{nl}(\chi)$ of the hyperangle χ [10]. The usual hyperharmonic basis reads

$$Z_{nlm} = X_{nl}(\chi)Y_{lm}(\theta,\phi) \tag{3.20}$$

$$= \sqrt{\frac{2^{2l+1}}{\pi}\frac{(n+1)(n-1)!l!^2}{(n+l+1)!}}\sin^l\chi G_{n-l}^{l+1}(\cos\chi)Y_{lm}(\theta,\phi), \tag{3.21}$$

with the familiar Gegenbauer polynomials $G_{n-l}^{l+1}(\cos\chi)$. The hyperangle χ is defined by $\cos\chi = p_4/\tilde{p}$ and $\sin\chi = |\vec{p}|/\tilde{p}$, where $\tilde{p} = \sqrt{p_4^2+\vec{p}^2}$ is the modulus for an Euclidean four-vector $p=(p_4,\vec{p})$. The partial decomposition of $\Gamma_\alpha(p)$ and $D^{AWW}(p-k)$ read as

$$\Gamma_\alpha(p) = \sum_n \varphi^n_{\alpha,l_\alpha}(\tilde{p})X_{nl_\alpha}(\chi_p)\mathcal{T}_\alpha(\vec{p}), \tag{3.22}$$

$$D(p-k) = 2\pi^2\sum_{\kappa\lambda\mu}\frac{1}{\kappa+1}V_\kappa(\tilde{p},\tilde{k})X_{\kappa\lambda}(\chi_p)X_{\kappa\lambda}(\chi_k)Y_{\lambda\mu}(\Omega_p)Y^*_{\lambda\mu}(\Omega_k), \tag{3.23}$$

where $V_\kappa(\tilde{p},\tilde{k})$ are the partial kernels and $\varphi^n_{\alpha,l_\alpha}(\tilde{p})$ are the expansion coefficients of the partial amplitudes. Actually l_α is restricted by the corresponding orbital momentum encoded in $\mathcal{T}_\alpha(\vec{p})$. For $\mathcal{T}_{1,2}(\vec{p})$ from Eq. (3.18) $l_\alpha=0$, while for $\mathcal{T}_{3,4}(\vec{p})$ $l_\alpha=1$. In analogy for vector mesons (see (3.19)), $l_\alpha=0$ for $\mathcal{T}_{1,2}(\vec{p})$, $l_\alpha=1$ for $\mathcal{T}_{3,4,7,8}(\vec{p})$ and $l_\alpha=2$ for $\mathcal{T}_{5,6}(\vec{p})$.
After changing the integration variables to the hyperspace,

$$d^4k = \tilde{k}^3\sin^2\chi_k\sin\theta_k d\tilde{k}d\chi_k d\theta_k d\phi_k, \tag{3.24}$$

inserting Eq. (3.22) and (3.23) into (2.8) and performing the necessary angular integration a system of integral equations for the expansion coefficients $\varphi^n_{\alpha,l_\alpha}(\tilde{p})$ remains:

$$\varphi^n_{\alpha,l_\alpha}(\tilde{p}) = \sum_\beta\sum_{m=1}^{\infty}\int d\tilde{k}\tilde{k}^3 S_{\alpha\beta}(\tilde{p},\tilde{k},m,n)\varphi^m_{\beta,l_\beta}(\tilde{k}). \tag{3.25}$$

The explicit expressions for $S_{\alpha\beta}(\tilde{p},\tilde{k},m,n)$ read

$$S_{\alpha\beta}(\tilde{p},\tilde{k},m,n) = \sum_{\kappa} \int \sin^2\chi_k d\chi_k X_{ml_\beta}(\chi_k) X_{\kappa\lambda}(\chi_k) \sigma_{s,v}(\tilde{k}_1^2)\sigma_{s,v}(\tilde{k}_2^2) \times A_{\alpha\beta}(\tilde{p},\tilde{k},\kappa,\chi_k,n), \tag{3.26}$$

where $\tilde{k}_{1,2}^2$ is given in Eq. (3.4). The expressions $A_{\alpha\beta}(\tilde{p},\tilde{k},\kappa,\chi_k,n)$ result from calculations of traces and angular integrations and have the form

$$\begin{aligned} A_{\alpha\beta}(\tilde{p},\tilde{k},\kappa,\chi_k,n) = \int & \sin^2\chi_p d\chi_p d\Omega_p d\Omega_k V_\kappa(\tilde{p},\tilde{k}) \\ & \times X_{nl_\alpha}(\chi_p) X_{\kappa\lambda}(\chi_p) Y_{\lambda\mu}(\Omega_p) Y^*_{\lambda\mu}(\Omega_k) \\ & \times \mathrm{Tr}[d_{\mu\nu}((p-k)^2)\gamma^\mu ... \mathcal{T}_\alpha(\vec{p}) ... \mathcal{T}_\alpha(\vec{p})\gamma^\nu]. \end{aligned} \tag{3.27}$$

They are separated in Eq. (3.26), because all angular integrations in Eq. (3.27) can be done analytically.
In explicit calculations, the sum over m in Eq. (3.25) is cut at a finite value N_{gegbau}, which means that relativistic covariance is broken. It must be checked whether the series converges and how large N_{gegbau} has to be chosen to obtain meaningful results. This may be a disadvantage of the hyperspherical decomposition. A big advantage is the reducing of at least three numerical angle integrations, which means explicitly for the calculations of this thesis a reduced computing time by a factor between 150 and 1200.

3.2.3 Extracting the meson mass eigenstates

In the previous section, the tBSE has been expanded into partial integral equations, which have to be solved. As mentioned above, Eq. (3.27) can be integrated analytically. Eq. (3.26) can be integrated numerically, where a Gauss-Chebyshev quadrature is used to provide all numerical angular integrations in this thesis. Later on in this chapter a method is introduced, where the integration over χ_k can be done analytically, too. The integration over $\tilde{k}$ in Eq. (3.25) is performed by a Gauss-Legendre quadrature, mapped over the interval $[0,\infty]$. Using numerical Gauss quadrature methods effects that the integral is replaced by a sum over well defined integration mesh points $\tilde{p}_i$, determined by the size of the mesh N_G. Taking this into account Eq. (3.25) can be seen as a matrix equation of the form

$$X = SX. \tag{3.28}$$

The vector X is the sought solution and reads as

$$X^T = ([\{\varphi_1^n(\tilde{p}_i)\}_{i=1}^{N_G}]_{n=1}^{N_{gegbau}}, \dots, [\{\varphi_{\alpha_{max}}^n(\tilde{p}_i)\}_{i=1}^{N_G}]_{n=1}^{N_{gegbau}}). \tag{3.29}$$

It has the total dimension N. The matrix S is of dimension $N \times N$ and is determined by Eq. (3.26), the Gaussian weights and the Jacobian of the mapping. The total dimension N depends on the number of spin-angular harmonics α_{max} (Equations (3.18) and (3.19)), the number of Gegenbauer polynomials N_{gegbau} and the size of the Gaussian integration mesh N_G with $N = \alpha_{max} \times N_{gegbau} \times N_G$.

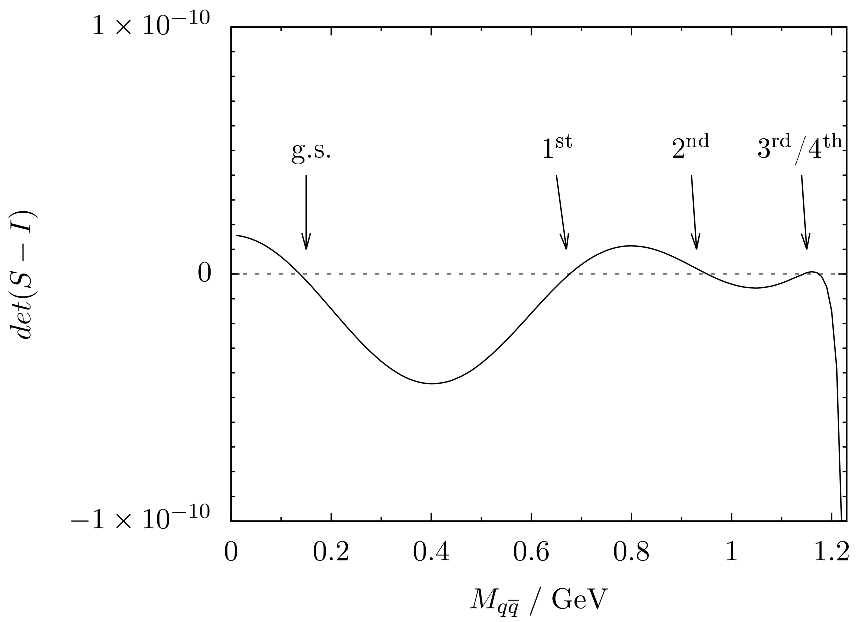

Figure 3.2: Smooth determinant function $det(S - \mathbb{1})$ as a function of $M_{\bar{q}q}$ for the pion ($m_u = 0.005\,\text{GeV}$). For $\omega = 0.3\,\text{GeV}$ and $D = 205.761\,\text{GeV}^{-2}$. The arrows denote the masses of groundstate (g.s.), first excited state (1^{st}), second excited state (2^{nd}), third and fourth excited state (3^{rd}, 4^{th}).

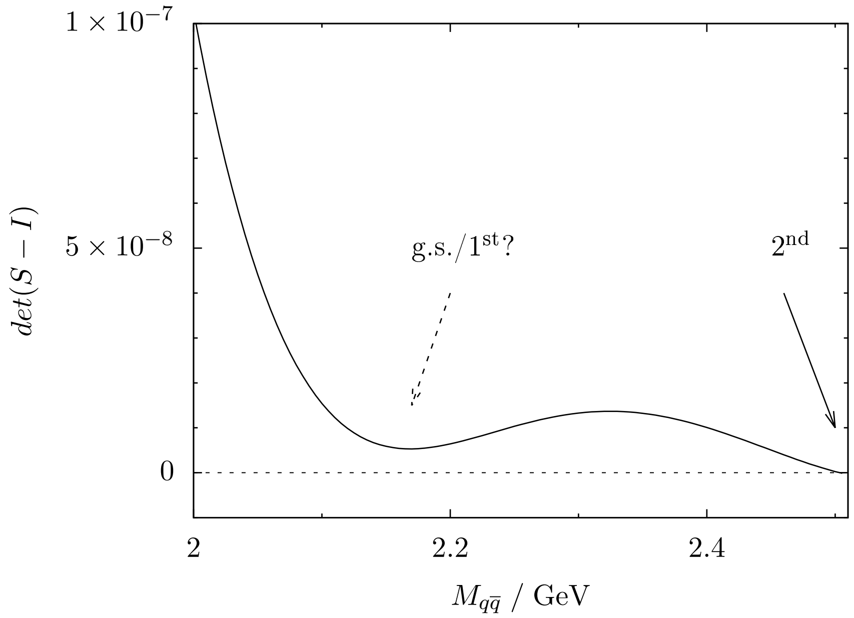

Figure 3.3: Smooth determinant function $det(S - \mathbb{1})$ as a function of $M_{\bar{q}q}$ for the D_s meson ($m_s = 0.115\,\text{GeV}$, $m_c = 1.130\,\text{GeV}$). For $\omega = 0.4\,\text{GeV}$ and $D = 48.828\,\text{GeV}^{-2}$. The first local minimum is above the x-axis (dashed arrow), the first root near $\text{M}_{\text{q}\bar{\text{q}}} = 2.5$ GeV belongs systematically to the second excited state (2^{nd}).

To obtain the boundstate mass $M_{q\bar{q}}$ the condition

$$det(S - \mathbb{1}) = 0 \tag{3.30}$$

is used, which can be applied since the system of equations (3.28) is homogeneous. For finding the determinant of condition (3.30) a *LU* decomposition function was implemented combined with a pivoting method. The determinant $det(S - \mathbb{1})$ as a function of $M_{q\bar{q}}$ is a smooth function, exemplary exhibited in Fig. 3.2 and Fig. 3.3 for particular model parameters. The roots of this function correspond to the condition (3.30) and represent the boundstate masses and excited states. That means, the leftmost root is the groundstate mass and the right-hand following roots are the first excited state, the second excited state and so on. The form of this determinant function depends on the model parameters D, ω, m_{q_1} and m_{q_2}, and, if they are slightly varied, the peaks and roots of the determinant function change their positions continuously. It can happen that two roots suddenly vanish

or arise because one peak of the determinant function moves across the x-axis, as depicted in 3.3. In such a case the following root is by convention counted as second excited state, to sort all boundstates in this thesis in a systematically way in dependence of the model parameters.
The obtained boundstate masses $\mathrm{M_{q\bar{q}}}$ can be used to solve iterative Eq. (3.25). For evaluating the meson mass spectrum this is not necessary, but for calculating e.g. decay constants and form factors of mesons. In Appendix E exemplary the solution of Eq. (3.25) for $\omega = 0.5\,\mathrm{GeV}$, $D = 16\,\mathrm{GeV}^{-2}$ and $m_{q_1} = m_{q_2} = 5\,\mathrm{MeV}$ ($\mathrm{M_{q\bar{q}}} = 0.137\,\mathrm{GeV}$) is depicted.
The arguments of the determinant function are limited by the appearance of poles (see Eq. (3.14)). If these poles are not taking into account yet the determinant function is a good indicator for the existence of them. Up to $M_{q\bar{q}} = M_{q\bar{q},max} = min(\chi_i/\eta_i)$ the determinant function is smooth, as in Fig. 3.2 and Fig. 3.3. For larger values of $M_{q\bar{q}}$ the determinant function is no longer smooth and has parts with asymptotic behavior and jumps. This is reasoned by the applied numerical methods, which, if possible, have to be be adjusted at the pole positions. In the next two sections methods are introduced, to increase the value of $M_{q\bar{q},max}$.

For completeness it should be mentioned that another common method exists for finding the boundstate masses [4, 15]. It is known as exhausting method or depletion method. The equation system (3.28) is solved as the eigenvalue problem

$$X = \lambda(M_{q\bar{q}})SX, \tag{3.31}$$

where $\lambda(M_{q\bar{q}})$ is the eigenvalue as a function of the boundstate mass $M_{q\bar{q}}$. The groundstate mass $M_{q\bar{q},gr}$ can be found at $\lambda(M_{q\bar{q},gr}) = 1$.

3.2.4 The momentum partitioning method

A good introduction for the topic of this section can be found in [26].

As long as no additional schemes have been introduced for handling the poles the integration domain of the tBSE is restricted by condition (3.14), that means for given partitioning parameter η it exists a maximal mass $M_{q\bar{q}}$. Because the tBSE depends on two quarks there are two conditions, one with

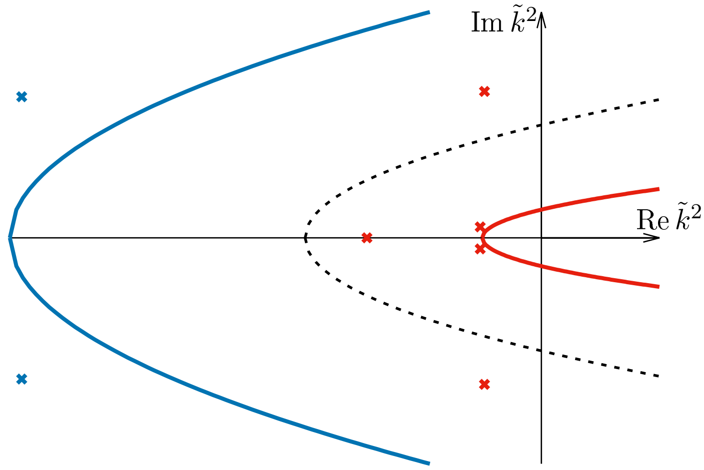

Figure 3.4: Parabolas (curves) and poles (symbols) for asymmetric partitioning (red and blue) in case of different quark masses. The dotted line is for $\eta = 0.5$ and includes three poles of the light quark in the integration domain of the tBSE.

$\chi_{m_{q_1}}$ and one with $\chi_{m_{q_2}}$. To calculate the matrix S of Eq. (3.28) for given $M_{q\bar{q}}$ it is important to check whether both conditions are fulfilled.

Generally it is of interest to find the largest mass $M_{q\bar{q},max}$ for which the poles are outside of the integration domain of the tBSE. Converting condition (3.14) for $\chi_{m_{q_1}}$ and $\chi_{m_{q_2}}$,

$$\eta_1 M_{q\bar{q}} \leq \chi_{m_{q_1}}, \tag{3.32}$$

$$\eta_2 M_{q\bar{q}} = (1-\eta_1) M_{q\bar{q}} \leq \chi_{m_{q_2}}, \tag{3.33}$$

leads to

$$M_{q\bar{q},max} = \chi_{m_{q_1}} + \chi_{m_{q_2}}, \tag{3.34}$$

$$\eta_1 = \frac{\chi_{m_{q_1}}}{\chi_{m_{q_1}} + \chi_{m_{q_2}}}, \tag{3.35}$$

$$\eta_2 = \frac{\chi_{m_{q_2}}}{\chi_{m_{q_1}} + \chi_{m_{q_2}}}. \tag{3.36}$$

The partitioning parameter defined in Eq. (3.35) will be called optimal η, η_{opt}, in this thesis. If the constituent quarks have equal masses, the pole structure is the same for both and therefore $\chi_{m_{q_1}} = \chi_{m_{q_2}}$. This means η_{opt} is 0.5 and the maximal mass is just fixed by $M_{q\bar{q},max} \leq 2\chi$. For non-equal quark masses the pole structure of each quark is different and for larger quark masses χ becomes larger. Therefore it is possible to increase η to catch higher masses up to $M_{q\bar{q},max}$ as defined in Eq. (3.34), see Fig. 3.4. The limit of the tBSE calculations is not determined by the lighter quark, but by the combination of both quarks. This procedure is called momentum partitioning method and has two important applications in this thesis. On the one hand side the calculated groundstate masses and excited states of the mesons must not depend on the momentum partitioning parameter η, otherwise Poincaré covariance will be violated [2]. Especially, the hyperspherical decomposition from Section 3.2.2 for finite N_{gegbau} violates relativistic covariance [2]. To check whether this is the case and how large N_{gegbau} has to be chosen the boundstate masses are calculated for different $\eta \in [0,1]$ and the variations of the results are considered. On the other hand side it turned out that $\chi_{m_{u/d}} \leq 0.65$ GeV in the considered parameter space of this thesis, which corresponds to a maximal mass of $M_{q\bar{q},max} = 1.3$ GeV for $\eta = 0.5$. To find masses and excited states of D mesons it is necessary to evaluate the tBSE at masses in the region of 2 GeV ($M_D = 1.870$ GeV [44]). With $\chi_{m_c} \geq 1.5$ GeV and the momentum partitioning method it is possible to find the required boundstates. The same problem appears for s quarks ($\chi_{m_s} \approx 0.75$ GeV) and D_s mesons ($M_{D_s} = 1.968$ GeV [44]).

3.2.5 Catching poles of the quark propagator

One of the goals of this thesis is to find the excited state spectrum of the considered mesons beyond the limitation of the quark propagator poles.

In [4, 15] a procedure is introduced to find excited states in the pole region. For finding the meson masses the exhausting method (3.31) is used up to the maximal mass $M_{q\bar{q},max}$ limited by the poles. The eigenvalues λ are smooth functions of $\mathrm{M_{q\bar{q}}}$. If they are plotted over $M^2_{q\bar{q}}$ they are almost linear functions. It is possible to extrapolate this functions beyond the pole limit, to find the intersection with $\lambda = 1$ and to obtain the sought masses of the excited meson states. The procedure seems to work well for mesons with equal quark masses. But there are some disadvantages of this method.

First, the linear behavior of λ vanishes for unequal quark masses. Secondly, the extrapolation method is afflicted by uncertainties, which are small just behind the pole limit, but become larger in the deep pole region (i.e. at higher energies). Thirdly, in general it is not clear whether the calculations continue in a linear form when poles appear in the integration domain.
In this thesis, it is tried to catch the poles explicitly and find a method to integrate over them, following substantially [10]. To apply this, the form of the propagator functions $\sigma_{s,v}(\tilde{k}^2)$ is important. As introduced in Section 3.1.2 the necessary propagator functions for the tBSE are calculated with two different methods (Eq. (3.6) and (3.9)) in two different areas (see Fig. 3.1). Looking at these two equations it can be seen that the summands of the second term in Eq. (3.9) have the same structure [1] as the summands in Eq. (3.6). The first term of Eq. (3.10), $\tilde{\sigma}_{s,v}(\tilde{k}^2)$, is a smooth function which can be parametrised easily in the same way as Eq. (3.6). Now all propagator functions $\sigma_{s,v}(\tilde{k}^2)$ can be expressed as a sum over components of the form

$$\frac{a_i}{\tilde{k}^2 - b_i^2}, \tag{3.37}$$

where a_i and b_i^2 are either the residues and the positions of the propagator poles $\tilde{k}_{0,i}^2$ or the parameters α_i and β_i^2 of the introduced parametrisation (3.6).
In the tBSE the propagator functions appear solely pairwise, which results in a sum over products of two expressions of the form (3.37) and can be cast in the following form:

$$\begin{aligned}
&\frac{a_i}{\tilde{k}_1^2 - b_i^2}\frac{a_j}{\tilde{k}_2^2 - b_j^2} = \left[\frac{a_i}{\mathrm{Re}(\tilde{k}_1^2) + 2\eta_1 i\,\mathrm{M}_{q\bar{q}}\,\tilde{k}t - b_i^2}\right]\left[\frac{a_j}{\mathrm{Re}(\tilde{k}_2^2) - 2\eta_2 i\,\mathrm{M}_{q\bar{q}}\,\tilde{k}t - b_j^2}\right] \\
&= \frac{a_i a_j}{4\eta_1\eta_2\,{\mathrm{M}_{q\bar{q}}}^2\,\tilde{k}^2} \\
&\times \left[\frac{1}{t - i(\mathrm{Re}(\tilde{k}_1^2) - b_i^2)/(2\eta_1\,\mathrm{M}_{q\bar{q}}\,\tilde{k})}\right]\left[\frac{1}{t - i(-\mathrm{Re}(\tilde{k}_2^2) + b_j^2)/(2\eta_2\,\mathrm{M}_{q\bar{q}}\,\tilde{k})}\right] \\
&= \frac{a_i a_j}{i\Delta z_{ij} 4\eta_1\eta_2\,{\mathrm{M}_{q\bar{q}}}^2\,\tilde{k}^2}\left[\frac{1}{t - iz_i^{(1)}} - \frac{1}{t - iz_j^{(2)}}\right],
\end{aligned} \tag{3.38}$$

[1] It is worth to remember that the poles appear only as pair with a self-conjugated partner which means $\sigma(\tilde{k}^2) = \sum_i \frac{a_i}{\tilde{k}^2 + b_i^2} + c.c.$

with $\mathrm{Re}(\tilde{k}_{1,2}^2) = -\mathrm{M_{q\bar{q}}}^2/4 + \tilde{k}^2$, $t = \cos\chi_k$, $\Delta z_{ij} = z_i^{(1)} - z_j^{(2)}$ and $z_{i,j}^{(1,2)} = (\pm\mathrm{Re}(\tilde{k}_{1,2}^2) \mp b_{i,j}^2)/(2\eta_{1,2}\,\mathrm{M_{q\bar{q}}}\,\tilde{k})$. The angular integration over χ_k in Eq. (3.26) can be done explicitly with the main integral

$$\begin{aligned}\mathcal{L}_{mn}^{\lambda}(z) &= \int_{-1}^{1} dt(1-t^2)^{\lambda-\frac{1}{2}} G_m^{\lambda}(t) G_n^{\lambda}(t) \frac{1}{t-iz} \\ &= \frac{2\sqrt{\pi}}{\Gamma(\lambda)2^{\lambda-\frac{1}{2}}} e^{(\frac{1}{2}-\lambda)i\pi}(-z^2-1)^{\frac{2\lambda-1}{4}} G_{min}^{\lambda}(iz) Q_{max+\lambda+\frac{1}{2}}^{\lambda-\frac{1}{2}}(iz),\end{aligned} \tag{3.39}$$

where $\Gamma(\lambda)$ is the gamma function, $G_m^{\lambda}(t)$ are the usual Gegenbauer polynomials and $Q_m^{\lambda}(t)$ are the Legendre functions of the second kind. The integral (3.39) is smooth and continuous as long as the nominator does not vanish. The nominator vanishes for certain t, if iz becomes purely real and $iz \in [-1, 1]$. Compared to the definition of z this is the case, if $\mathrm{Re}(\tilde{k}_{1,2}^2) = \mathrm{Re}(b_{i,j}^2)$ and $2\eta\,\mathrm{M_{q\bar{q}}}\,\tilde{k} \geq \mathrm{Im}(b_i^2)$. It can be shown that this constraint is equivalent to the condition for the maximal parabolic integration region of the tBSE (3.14) if $b_{i,j}^2$ represents one of the propagator singularities $\tilde{k}_0^2$. In contrast to the above introduced numerical integration procedure the integral (3.39) is well defined by a principal value for $\tilde{k}^2 = \eta^2\,\mathrm{M_{q\bar{q}}}^2 - \mathrm{Re}(\tilde{k}_0^2) =: \tilde{k}_{crit}^2$. Worth to mention is that the crossing from $\tilde{k}_{crit}^2 - \epsilon$ to $\tilde{k}_{crit}^2 + \epsilon$ is not continuous, but has a finite jump, that means to the left and to the right of $\tilde{k}_{crit}^2$ the integral (3.39) yields two different finite values. Numerically, this is treated by splitting the Gaussian mesh of $\tilde{k}$ into two parts, one from 0 to $\tilde{k}_{crit}$ and the other from $\tilde{k}_{crit}$ to ∞. With such a splitting for each pole $\tilde{k}_{0,i}^2$ located inside the integration domain the integration over all singularities can be done well controlled and correctly.

One special case appears if $z_i^{(1)} = z_j^{(2)}$ and therefore $\Delta z_{ij} = 0$ (for example, if $m_{q_1} = m_{q_2}$ and $\eta_1 = \eta_2 = 0.5$). Equation (3.38) has no longer an integrable form if $2\eta\,\mathrm{M_{q\bar{q}}}\,\tilde{k} \geq \mathrm{Im}(b_{i,j}^2)$ (the case when poles are present in the integration domain of the tBSE). To avoid this problem the partitioning parameters η has to be chosen unequal 0.5 for mesons with two equal constituent quarks.

4 | Results

From Eq. (2.10), (2.5) and (2.8) it is seen, that the approach of the interaction model introduces four parameters, ω, D, m_{q1} and m_{q2}, which must be adjusted. That set of parameters must be found which reproduces experimental values as good as possible. For realising this in a well structured way, at first ω and D have to be fixed at a benchmark, and afterwards m_{q_1} and m_{q_2} are chosen in such a way to compare the obtained results for the meson masses with results from other groups. Then the quark masses m_{q_1} and m_{q_2} were varied continuous. After finishing this we defined paths in the ω - D parameter space, on which several meson masses are obtained. Finally, it is attempted to expand the calculations to a continual finite part of the parameter space finding meson masses and other observables for certain quark masses.

4.1 Meson spectrum at common benchmark

To check the numerical implementation of the techniques from the previous chapter it is highly recommend to recalculate values from other groups, which were using the same model. A convenient set of parameters is $\omega = 0.5$ GeV and $D = 16$ GeV^{-2}, which has been used by different groups, e.g. [2, 26]. The quark masses are set to $m_u = m_d = 5$ MeV, $m_s = 115$ MeV and $m_c = 1130$ MeV. In the following always the relation $m_u = m_d$ is used and when speaking on u quarks it is also concerned to d quarks. The obtained results for groundstate masses and excited-state masses for pseudoscalar and vector mesons are summarised in Tab. 4.1 and Tab. 4.2.
The chiral condensate $\langle q\overline{q}\rangle^{m_q=0} = \langle q\overline{q}\rangle^0$ was found with

$$\langle q\overline{q}\rangle^{m_q=0} = (-251\text{GeV})^3, \qquad (4.1)$$

Table 4.1: Mass spectrum of pseudoscalar boundstates, $J^{PC} = 0^{-+}$, for the parameter set $\omega = 0.5$ GeV, $D = 16$ GeV, $m_u = m_d = 5$ MeV, $m_s = 115$ MeV and $m_c = 1130$ MeV, corresponding references of other groups and experimental values, in units of GeV. "g.s.","1st" and "2nd" stand for groundstate, the first and the second radial excitations. The "–" for the D groundstate means that no boundstate for the employed parameters could be found; accordingly, there is also no solution for the radial excitations.

	Results	Reference	Exp. [44]
$M_{\pi,g.s.}$	0.137	0.137 [2]	0.140
$M_{\pi,1st}$	0.986		1.300
$M_{\pi,2nd}$	1.369		1.812
$M_{K,g.s.}$	0.492	0.492 [2]	0.494
$M_{K,1st}$	1.162		1.460
$M_{s\bar{s},g.s.}$	0.693		
$M_{s\bar{s},1st}$	1.278		
$M_{s\bar{s},2nd}$	1.572		
$M_{D,g.s.}$	–		1.870
$M_{D_s,g.s.}$	2.075		1.968
$M_{D_s,1st}$	2.313		
$M_{\eta_c,g.s.}$	2.984		2.984
$M_{\eta_c,1st}$	3.278		3.639
$M_{\eta_c,2nd}$	3.557		

which is in agreement with [26] and also with [43]. It has been calculated with Eq. (4.6) from Section 4.4.

Another quantity which has been examined in this thesis is the pseudoscalar decay constant of the pion f_π. With the found groundstate mass $M_{\pi,0}$ Eq. (3.25) can be used to find iterative the solution of the truncated Bethe-Salpeter equation. This solution has been normalised as described in [2, 40]. The normalised solution has been inserted into formula (16) of [2] to obtain the decay constant f_π. The obtained value is

$$f_\pi = 0.133\,\text{GeV}, \tag{4.2}$$

which is in agreement with [2]. Unfortunately for kaons no meaningful and comparable values of f_K could be obtained.

Table 4.2: As Tab. 4.1 but for vector states, $J^{PC} = 1^{--}$.

	Results	Reference	Exp. [44]
$M_{\rho,g.s.}$	0.758	0.758 [2]	0.775
$M_{\rho,1st}$	1.041		1.465
$M_{\rho,2nd}$	1.287		1.720
$M_{K^*,g.s.}$	0.945	0.946 [2]	0.894
$M_{K^*,1st}$	1.264		1.414
$M_{\phi,g.s.}$	1.077	1.072 [2]	1.019
$M_{\phi,1st}$	1.402		1.680
$M_{\phi,2nd}$	1.598		2.175
$M_{D^*,g.s.}$	–		2.010
$M_{D_s^*,g.s.}$	–		2.112
$M_{J/\psi,g.s.}$	3.136		3.097
$M_{J/\psi,1st}$	3.346		3.686
$M_{J/\psi,2nd}$	3.593		3.773

With the values of $M_{\pi,0}$, $\langle q\overline{q}\rangle^{m_q=0}$ and f_π it can be checked if the Gell-Mann-Oakes-Renner (GMOR) relation [39],

$$f_\pi^2 M_{\pi,0}^2 = -2m_q\langle q\overline{q}\rangle^{m_q} = -2m_q\langle q\overline{q}\rangle^{m_q=0} + O(m_q^2) \tag{4.3}$$

is fulfilled (respecting the different definition of f_π in [39] which differs by a factor $\sqrt{2}$ from the definition in [2]). The value of $\langle q\overline{q}\rangle^{m_q}$ obtained with Eq. (4.3) is $(-0.255\,\mathrm{GeV})^3$, which is close to the calculated value for $\langle q\overline{q}\rangle^{m_q=0}$. That means the expression $O(m_q^2)/[2m_q\langle q\overline{q}\rangle^{m_q=0}] = 0.016$ is small, as it is supposed for small values of m_q. Therefore it can be said that the GMOR relation is fulfilled.

The calculations in general are not restricted to discrete values of m_{q_1} and m_{q_2}. If the parameters ω and D are determined (like above), m_{q_1} and m_{q_2} can be seen as continuous parameters to obtain meson masses and excitations. This has been done in [10] with one fixed quark mass and one running quark mass for groundstates of pseudoscalar mesons and in [2] with two running quark masses and the condition $m_{q1} = m_{q2}$ for groundstates of mesons with different J^{PC}. In Fig. 4.1, the pseudoscalar meson groundstates are plotted for two running quark masses $m_{x,y}$ from 0 GeV to 1.2 GeV. In Fig.

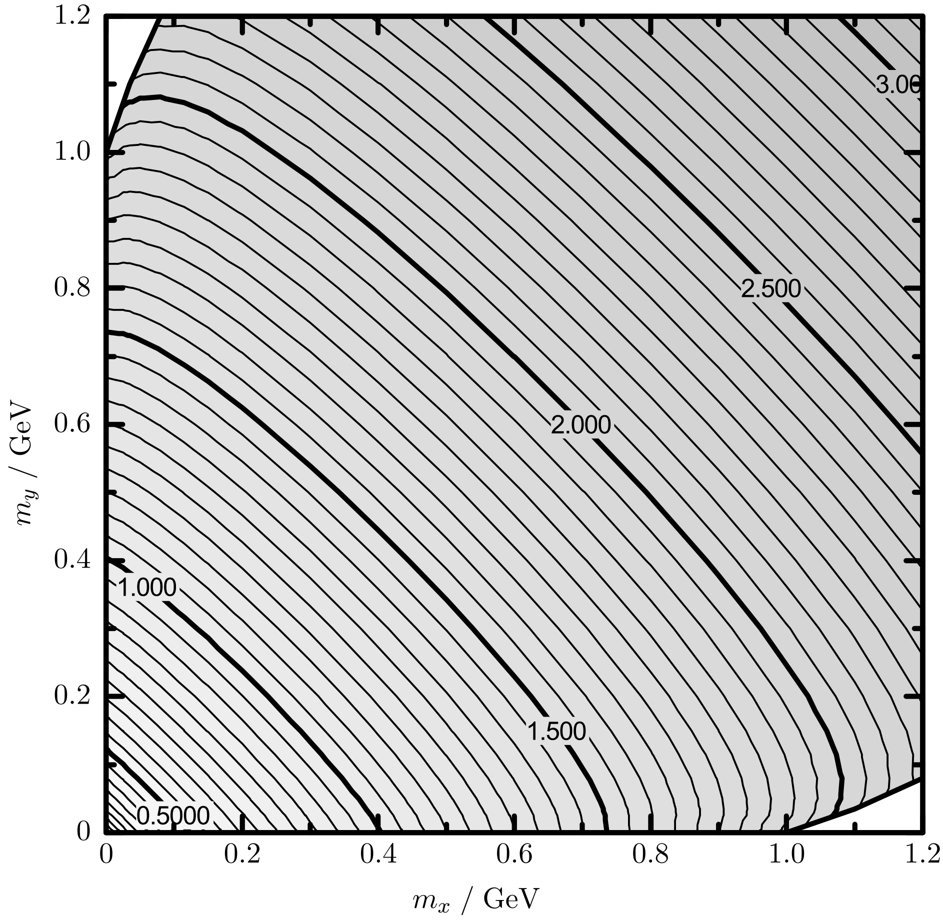

Figure 4.1: Contour plot of pseudoscalar meson groundstate mass M_{xy} in units of GeV for varying quark masses m_x and m_y. Parameters $\omega = 0.5$ GeV, $D = 16$ GeV^{-2}.

4.2, the corresponding first excitations are plotted. In Fig. 4.3, the vector meson groundstates are plotted for the same interval of quark masses, in Fig. 4.4 the first excitations of vector mesons are exhibited. All calculations have been done with optimal partitioning parameter η_{opt} (see Section 3.2.4 and Eq. (3.35)). The values of Fig. 4.1 and 4.3 on the diagonal $m_x = m_y$ are conform with [2]. All meson masses and excited states are smooth functions in m_x and m_y. In the white areas of the plots where no contour lines are located no meson eigenstates could be found, that means the determinant function of Eq. (3.30) has a minimum in the region of $\mathrm{M}_{\mathrm{q\bar{q}}}$ where the boundstate is expected, but no root. An interesting observation is that in some regions the groundstate mass $\mathrm{M}_{\mathrm{q\bar{q}}}$ rises in a non-intuitive way in de-

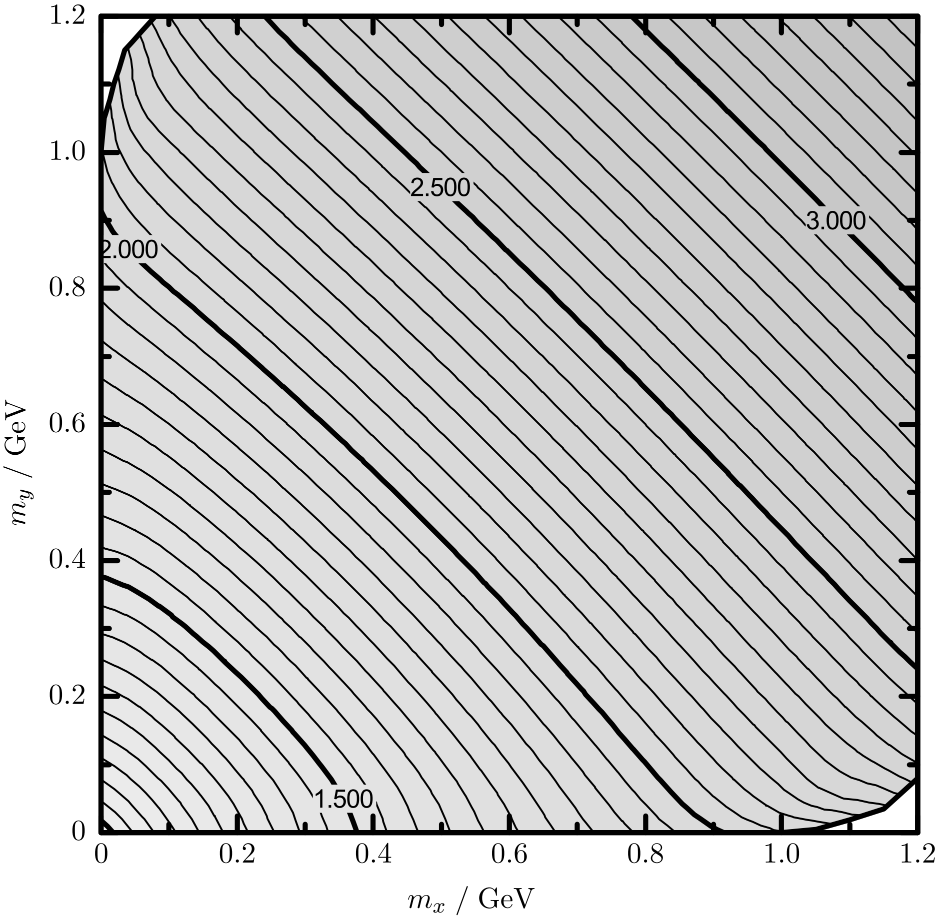

Figure 4.2: Contour plot of pseudoscalar meson 1st excited state mass M_{xy} in units of GeV for varying quark masses m_x and m_y. Parameters $\omega = 0.5$ GeV, $D = 16$ GeV^{-2}.

pendence of the quark masses $m_{x,y}$. In particular, if one quark mass is hold constant at $m_x \geq 0.8$ GeV for pseudoscalar mesons and the other quark mass m_y is varied in $[0, 0.2]$ GeV, then the minimum of $\mathrm{M}_{\mathrm{q}\bar{\mathrm{q}}}$ is not located at $m_y = 0$ GeV (or the smallest possible quark mass where boundstates are found), but somewhere in $[0, 0.2]$ GeV. This means that mesons with lighter constituent quark masses can have a larger boundstate mass. Especially if the c quark mass m_c is chosen in such a way to obtain groundstate masses for D and D_s mesons it yields $M_D > M_{D_s}$. This stands in contrast to the plotted values in [10] and [26], which may belong to some considerations illustrated in Appendix D.
The first excited states of pseudoscalar mesons (Fig. 4.2) show smooth be-

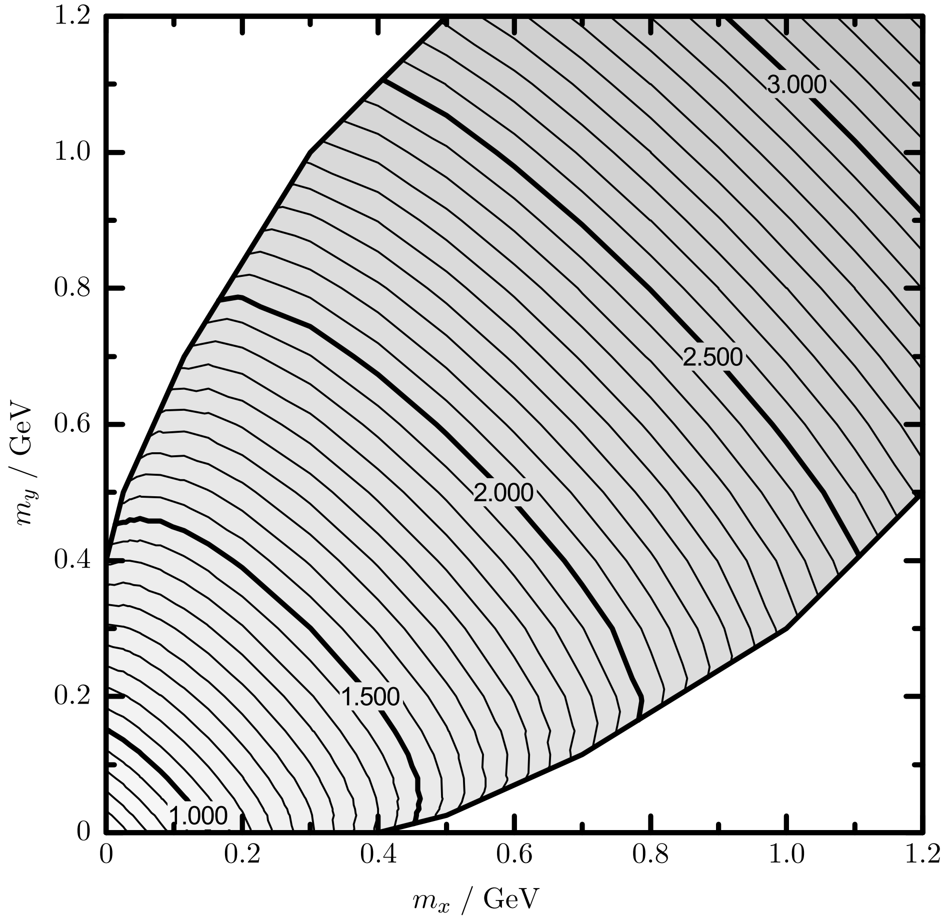

Figure 4.3: Contour plot of vector meson groundstate mass M_{xy} in units of GeV for varying quark masses m_x and m_y. Parameters $\omega = 0.5$ GeV, $D = 16$ GeV^{-2}. Outside of the grey region, a solution of the tBSE could not be found.

haviour in dependence of m_x and m_y without irregular effects. In the white area without contour lines again no $\mathrm{M_{q\bar{q}}}$ which fulfills condition (3.30) could be found (which is clear if a local minimum is located above the real x-axis then two roots are missing, compare Fig. 3.3). For vector mesons (Fig. 4.3) the white area, where no groundstates could be found, is larger than in the other two plots. This is due to the fact that the boundstates are located beyond the pole limit and they are no longer smooth functions in m_x and m_y (more about problems in the pole region below in Section 4.6). As in the pseudoscalar case again the irregular behaviour can be observed near the upper left and lower right boarder line, where the contour lines "turn back", that means for increasing $m_{x,y}$ the boundstate mass $\mathrm{M_{q\bar{q}}}$ decreases. The

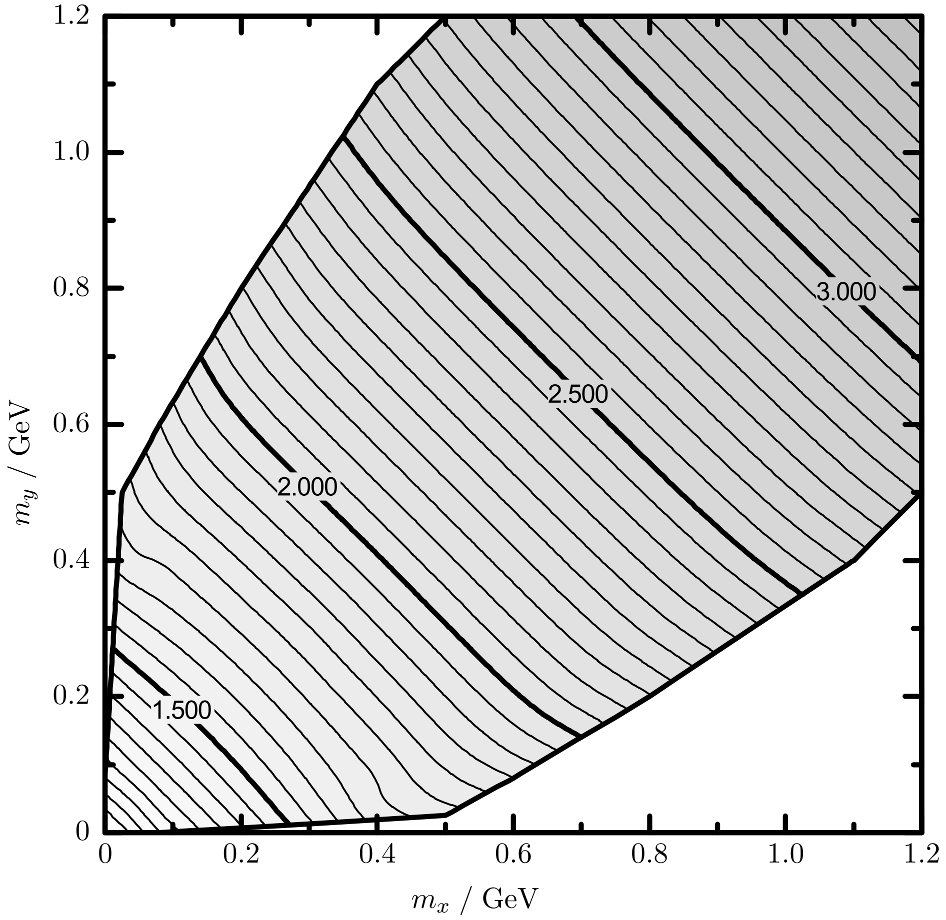

Figure 4.4: Contour plot of vector meson 1st excited state mass M_{xy} in units of GeV for varying quark masses m_x and m_y. Parameters $\omega = 0.5$ GeV, $D = 16$ GeV^{-2}. Outside of the grey region, a solution of the tBSE could not be found.

plot for the first radially excitations of vector mesons (Fig. 4.4) looks similar compared to the plot of pseudoscalar excitations, but with a larger white area where no boundstates have been found (with the same argumentation as made for the vector meson groundstates).
The mentioned irregular or unphysical behaviour seems to be model dependent concerning to the used kernel (2.10), because with similar interaction kernels (like kernel (2.9) used in [22]) this effect does not appear.

While one can attempt an optimisation of the parameters ω, D, m_u, m_s and m_c to find the best reproduction of masses of π, K, D, D_s and η_c as lowest boundstates of $u\bar{d}$ and mixture, $u\bar{s}$, $u\bar{c}$, $s\bar{c}$ and $c\bar{c}$ in the pseudoscalar channel

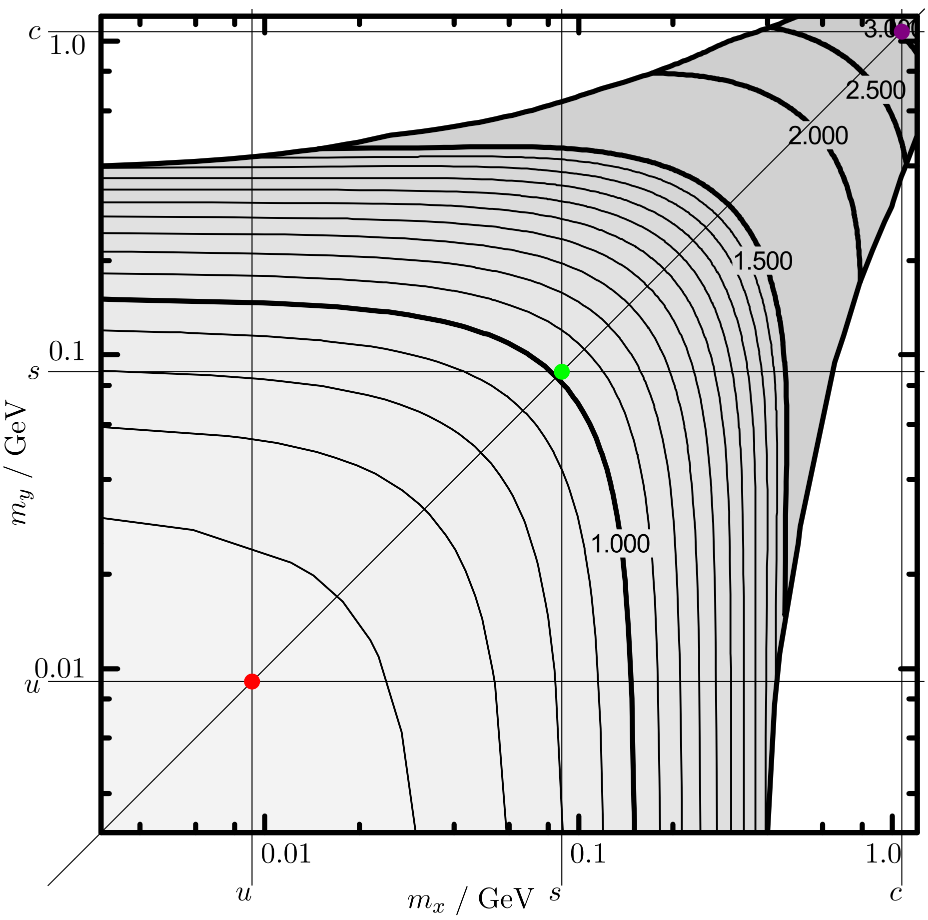

Figure 4.5: Contour plot of vector meson groundstate mass M_{xy} in units of GeV for varying quark masses m_x and m_y in logarithmic representation. Parameters $\omega = 0.5$ GeV, $D = 16$ GeV^{-2}. The coloured bullets denote the experimental values (see Tab. 4.2) of meson groundstates (red: ρ, green: ϕ, violet: J_ψ; all located on the diagonal $m_x = m_y$.) which could be used for extracting the bare quark masses (vertical and horizontal thin lines, labeled by the corresponding quark flavour); the corresponding value of m_c (1.110 GeV) can be compared with one suggested in the pseudoscalar channel, see Fig. 4.6, which was found there as 1.130 GeV.

as well as $\rho, K^*, \phi, D^*, D_s^*$ and J/ψ as lowest boundstates of $u\bar{d}$ and mixture, $u\bar{s}$, $s\bar{s}$, $u\bar{c}$, $s\bar{c}$ and $c\bar{c}$ in the vector channel, some survey on the achieved accuracy is provided by the following procedure:

(i) Since a pure pseudoscalar $s\bar{s}$ state does not exist in nature start with the vector channel and display in the contour plot, Fig. 4.3, a diagonal

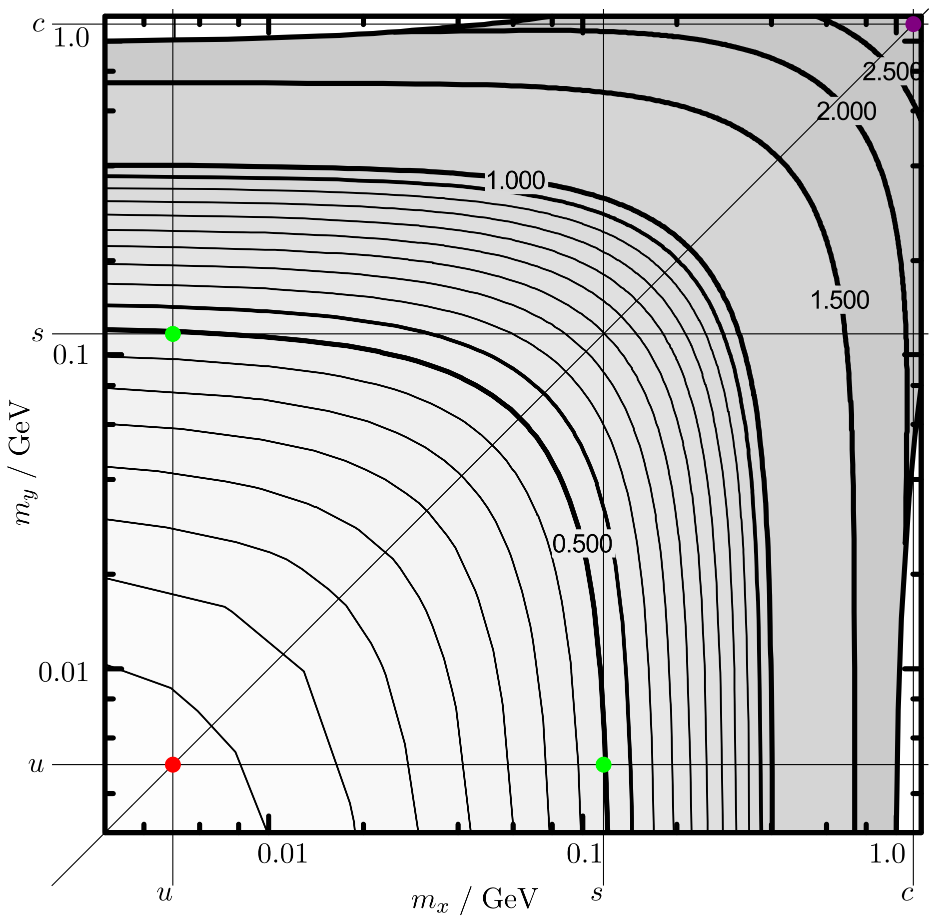

Figure 4.6: Contour plot of pseudoscalar meson groundstate mass M_{xy} in units of GeV for varying quark masses m_x and m_y in logarithmic representation. Parameters $\omega = 0.5$ GeV, $D = 16$ GeV^{-2}. The coloured bullets denote the experimental values (see Tab. 4.1) of meson groundstates (red: pion, green: kaon, violet: η_c) which were used for extracting the bare quark masses (vertical and horizontal thin lines, labeled by the corresponding quark flavour). Pion and η_c must be located on the diagonal $m_x = m_y$.

with symbols at the crossings with contour curves at the respective meson masses. Read off the required masses $m_{u,s,c}$.

(ii) Make a grid of horizontal and vertical lines emerging from each of the symbols determined in item (i). The crossings of these lines “predict” the masses of further mixed-quark meson states: $u\bar{s}$, $u\bar{c}$ and $s\bar{c}$.

The comparison of the found meson masses with experimental values is not overwhelming since the $u\bar{c}$ and $s\bar{c}$ states are in the white region where the

employed kernel (2.10) with parameters $D = 16\,\mathrm{GeV}^{-2}$ and $\omega = 0.5\,\mathrm{GeV}$ does not deliver boundstates, see Fig. 4.5. The "predicted" K^* mass is 0.914 GeV, to be compared with the experimental value of 0.894 GeV.
One may proceed with the same strategy in the pseudoscalar channel, which, however, delivers in step (i) only m_u and m_c. A comparison with the quark masses from the vector channel shows small differences: in the vector channel the quark masses are $m_u = 10\,\mathrm{MeV}$ and $m_c = 1110\,\mathrm{MeV}$, in the pseudoscalar channel the quark masses are as given in the caption of Tab. 4.1. The mass of the predicted $u\bar{c}$ state has to be compared with the D groundstate mass of 1.870 GeV. As in the vector channel with the same parameters ω and D this $u\bar{c}$ state is in the white region where no boundstates are delivered. One can then extract from the crossing of either a "c line" or a "u line" with the contour curve of either 1.968 GeV (D_s) or 0.494 GeV (K) the needed value of m_s. Fig. 4.6 exhibits that the crossing of the "c line" with a 1.968 GeV contour curve is missed, i.e. the crossing of the "u line" is to be used to construct additionally the "s lines" and inspect the "predicted" masses at $s\bar{c}$ crossing: 2.075 GeV.
Various mixtures of such simple cross checks are considerable; go with the quark masses determined in one channel into the other channel and compare the "predictions" with experimental values. The overall impression is that the kernel delivers a quite good description of the groundstate meson masses in both considered channels. This is, of course, not a surprise hence the kernel has been originally designed just to do such a job.

The literature reports some notorious difficulties for other channels and sometimes remarks are made the kernel (2.10) is less appropriate for excited states, but the information is spare, cf. [2]. In fact, inspecting the contour plot in Fig. 4.2 for the first radial excitation of the pseudoscalar channel or the contour plot in Fig. 4.4 for the first radial excitation of the vector channel one becomes aware of severe deviations of predicted and experimental values. Therefore, now it is turned to the question whether variations of the partitioning parameter η or variations of D and ω of the kernel (2.10) remedy the discrepancy.

4.2 Dependency of the partitioning parameter

In principle, the results must be independent of the partitioning parameter η. Anyway, the hyperspherical decomposition with truncation at a finite value of N_{gegbau} causes a violation of relativistic covariance, which could result in η dependent observables. It is important to check whether such a dependence appears and how large the deviations are. In Fig. 4.7 the groundstate masses of pions and ρ mesons are plotted in dependence on η for different numbers N_{gegbau}. Clearly, the curves are symmetric, because the quark masses are equal. In Fig. 4.8 the groundstate masses of kaons and D_s mesons are plotted. All these curves are smooth. It is well seen that the higher the number N_{gegbau} the smaller are the variations of the individual graphs. It appears that $N_{gegbau} \geq 3$ is required to obtain meaningful values for convenient values of η (i.e. η_{opt}, compare Eq. (3.35)).

Table 4.3: Variation of groundstate meson masses (in units of MeV) for $\eta \in [0, 1]$ for various values of N_{gegbau}

N_{gegbau}	ΔM_π	ΔM_ρ	ΔM_{K}	ΔM_{Ds}
1	8.8	13.6	60.1	133.0
2	0.11	5.8	26.4	63.0
3	0.009	1.9	3.5	33.4
4	0.009	0.3	0.4	7.2
5	0.03 e-3	0.04	0.07	1.2
6	0.03 e-3	0.02	0.03	0.24
7	0.03 e-3	0.02	0.03	0.22

In Tab.4.3 the variations deduced from the plots in Fig. 4.7 and 4.8 are exhibited. The values for ρ and D_s, in principle, have to be larger, because the considered range of η was reduced by the appearance of the propagator poles. Looking at the numbers shows that the deviations are smaller for light mesons with light quarks and for mesons with nearly equal-mass quarks. It also shows that it is preferable to use at least $N_{gegbau} = 6$ to be sure getting results with MeV precision. Especially in the pion column it seems that there is a limit (here at $N_{gegbau} = 5$), at which the results do not become better with further increasing number of harmonics. This comes from the other numerical parameters and routines and does not play a role, since it is not our goal to improve the precision beyond a few MeVs.

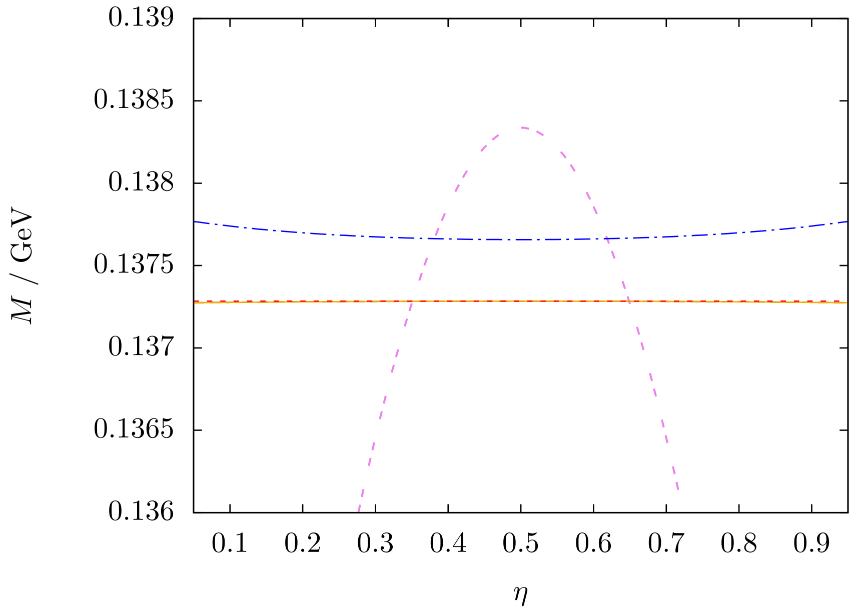

(a) π

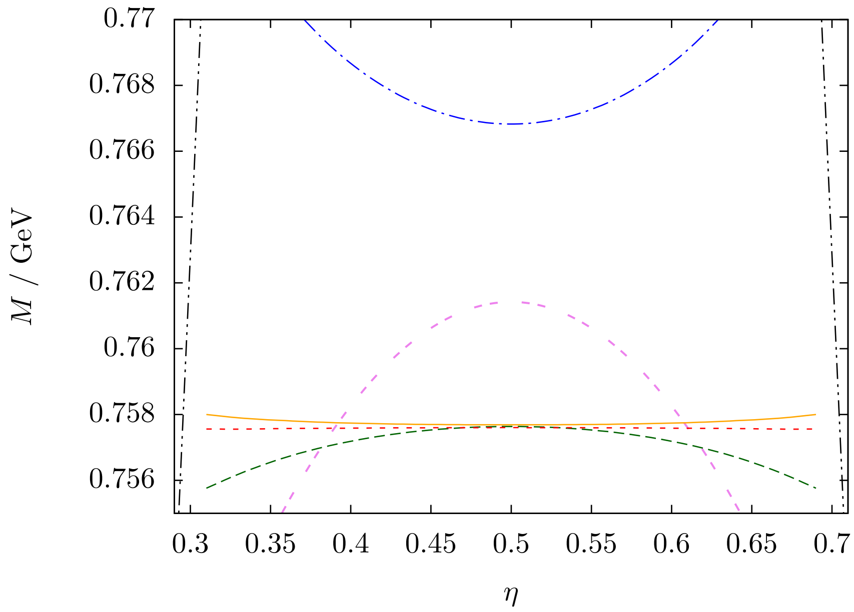

(b) ρ

Figure 4.7: Dependency of pion (upper panel) and ρ meson (lower panel) groundstate mass (in units of GeV) on the partitioning parameter η for different numbers of included Gegenbauer polynomials N_{gegbau}: dashed-dashed violet: $N_{gegbau} = 1$, dashed-dotted blue: $N_{gegbau} = 2$, dashed green: $N_{gegbau} = 3$, solid orange: $N_{gegbau} = 4$, dotted red: $N_{gegbau} = 5$. The black dashed-dot-dotted curves represent the limitation by the pole structure (see Fig. 3.4).

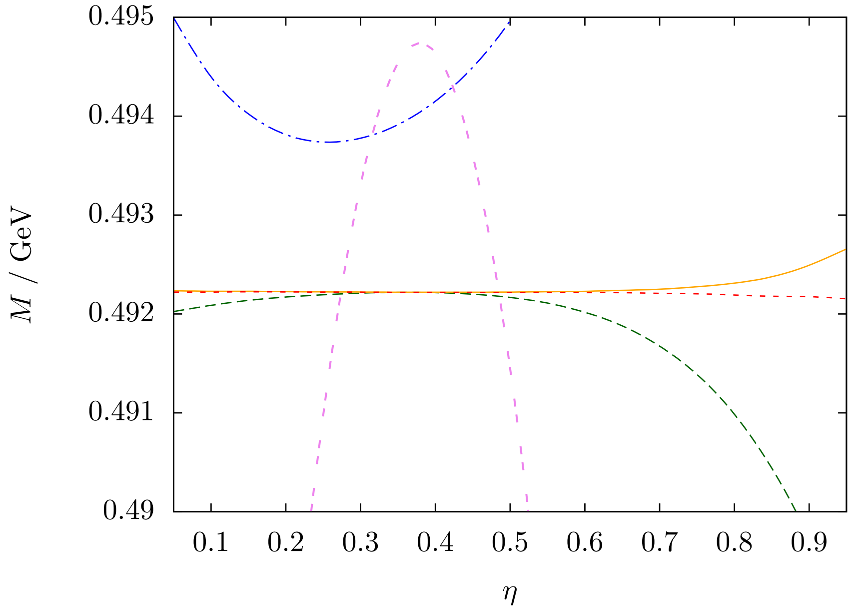

(a) K

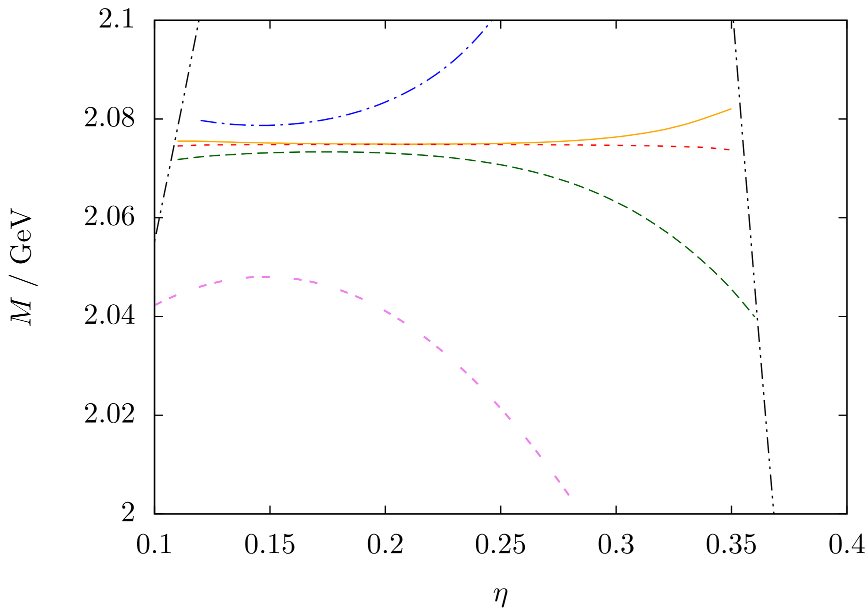

(b) D_s

Figure 4.8: As Fig. 4.7, but for kaons (upper panel) and D_s mesons (lower panel).

4.3 Variations of the parameters ω and D

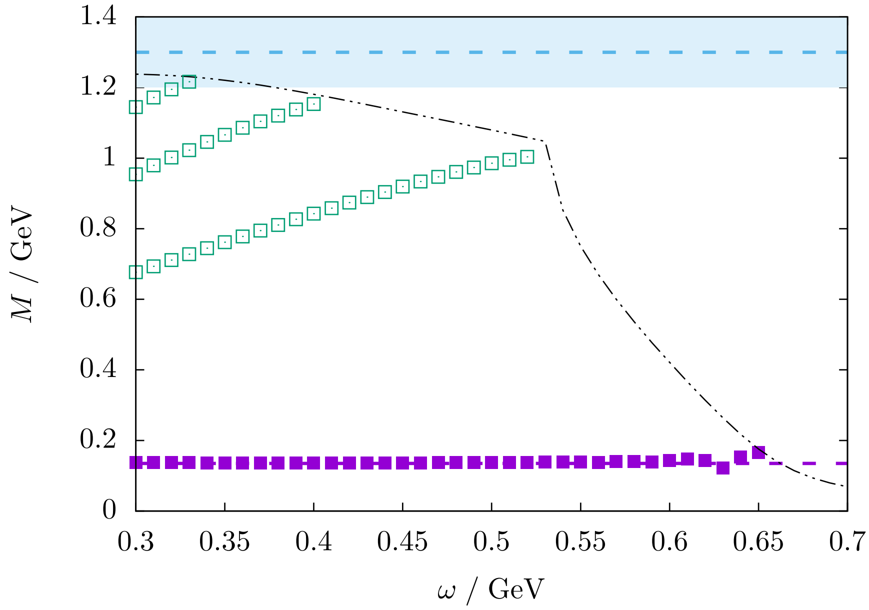

Figure 4.9: Variations of pion groundstate masses (filled violet boxes) and radially excited states (empty green boxes) as a function of ω for $a = 0.5\ \text{GeV}^3$. The dashed violet line represents the experimental value of the pion groundstate and the blue bar represents the experimental value of the first excitation of the pion. The dashed-dot-dotted curve depicts the limitation by the pole structure, i.e. for higher masses the poles are inside the integration domain (see Fig. 3.4).

The previous section has evidenced that the groundstates of π, K, ρ, K^*, ϕ, η_c and J/ψ could be described fairly accurately with the benchmark parameters ω and D. That is the description of seven groundstate masses by the adjustment of the five parameters ω, D, $m_{u/d}$, m_s and m_c. The excited states of these mesons are all too small compared to the experimental values. For the heavy-light mesons either no values of groundstates are found (e.g. D, D^*, D_s^*) or they are too large (e.g. D_s).

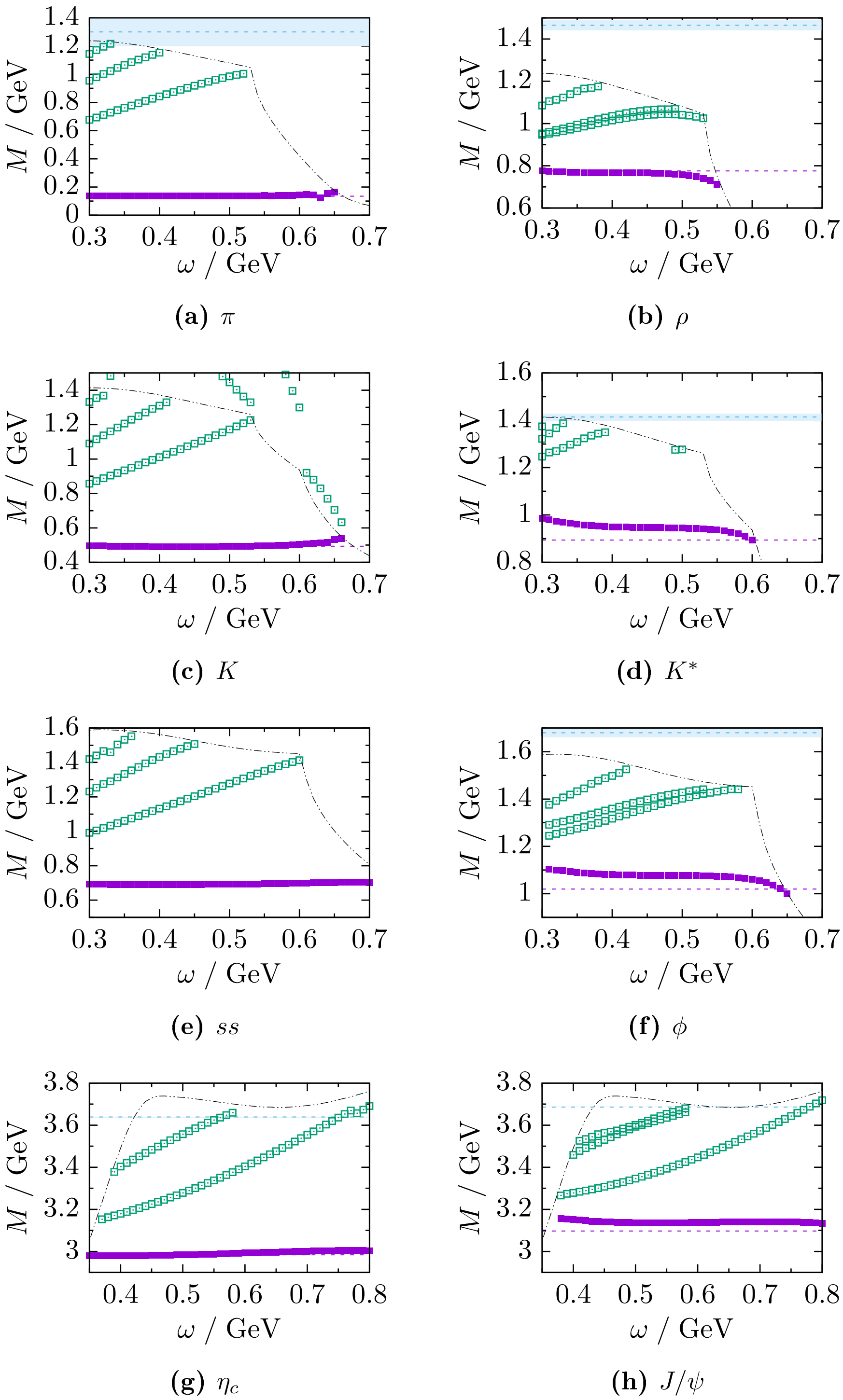

Figure 4.10: As Fig. 4.9 for different pseudoscalar mesons (left column) and vector mesons (right column).

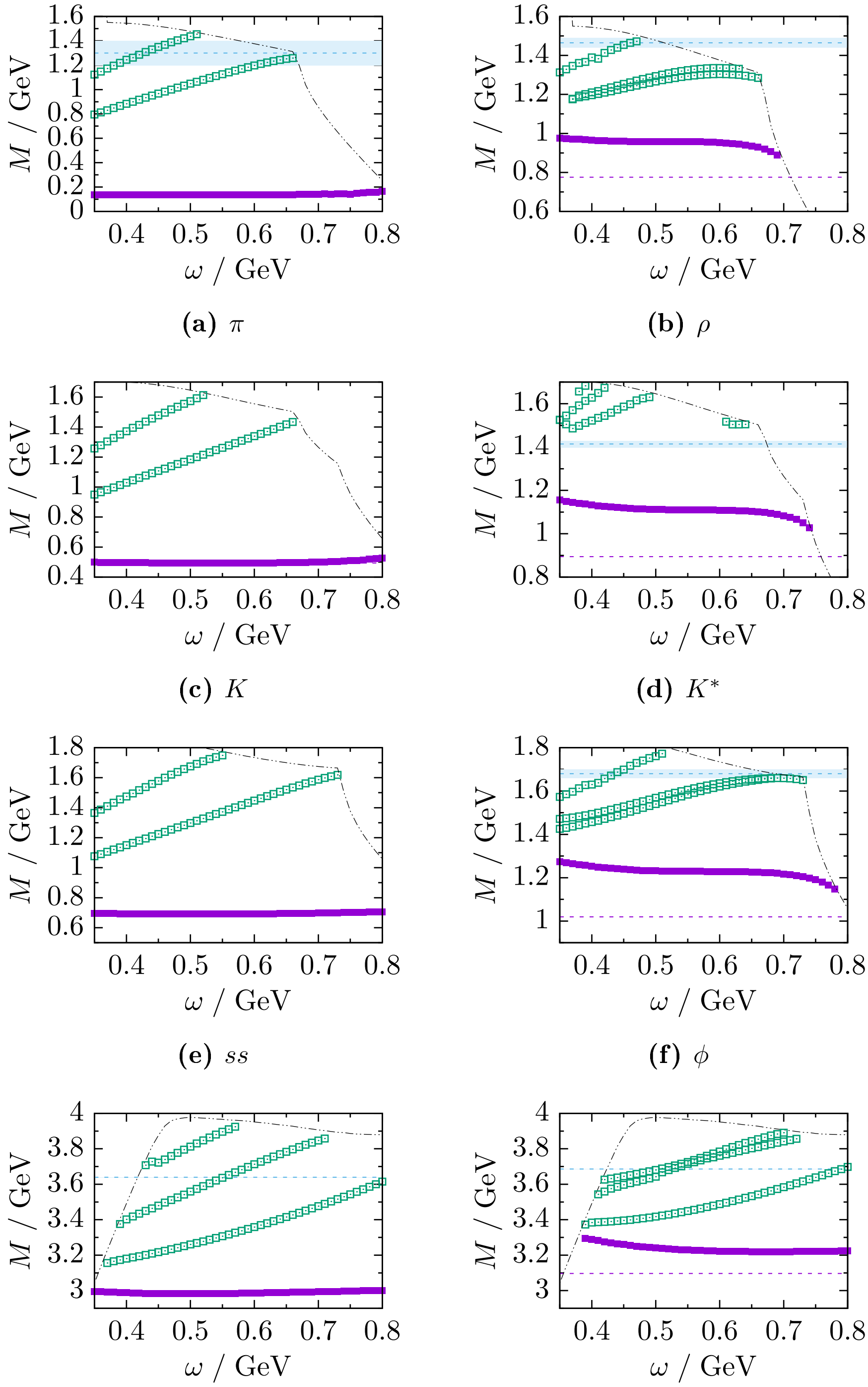

(a) π **(b)** ρ

(c) K **(d)** K^*

(e) ss **(f)** ϕ

(g) η_c **(h)** J/ψ

Figure 4.11: As Fig. 4.10 but for $a = 1\,\mathrm{GeV}^3$. The quark masses were fixed at $\omega = 0.5$ GeV to $m_u = 0.004\,\mathrm{GeV}, m_u = 0.095\,\mathrm{GeV}, m_u = 1.043\,\mathrm{GeV}$.

In [32, 37] it was found that the groundstates of pseudoscalar and vector mesons are nearly constant within the MT model (2.9) for $\omega\overline{D}$ hold at a constant value in the interval $\omega \in [0.3, 0.5]$ GeV. $\overline{D} = \omega^4 D$ is an equivalent and often used definition for D with $[\overline{D}] = \text{GeV}^2$. It is expected that the AWW kernel (2.10) provides this property, too. Therefore a new quantity is introduced:

$$a \;=\; \omega\overline{D} \;=\; \omega^5 D. \tag{4.4}$$

For the above benchmark, a has the value 0.5 GeV^3. If a is hold constant, one model parameter remains, where ω is treated as a variable and D is respectively adjusted. In Fig. 4.9, 4.10 and 4.11 the results for quark combinations $u\bar{u}$, $u\bar{s}$, $s\bar{s}$ and $c\bar{c}$ for different values of a are exhibited. The quark masses were fixed at $\omega = 0.5$ to obtain the experimental values for the groundstate masses of pion, kaon and η_c. For $a = 0.5$ GeV^3 the groundstate masses are nearly constant with only less variations. The deviation of the groundstate masses to their experimental values are small and the relative deviations are smaller than ten per cent. The radially excited states of the pseudoscalar mesons (left column of Fig. 4.10 and 4.11) are well arranged in separable trajectories. For the vector mesons (right column of Fig. 4.10 and 4.11) the excited states are also arranged in trajectories, but with a few gaps, especially for ϕ. The difference between the first and the second radially excited states of ρ and K^* and the difference between the second and third radially excited states of J/ψ are very small compared to the distances between all other boundstates. All trajectories are rising for increasing ω. For η_c the first radially excitation coincides with the experimental value (blue dashed lines) at about $\omega = 0.75$ GeV, the gap between groundstate and first excited state of J/ψ coincides with the experimental value near $\omega = 0.8$ GeV. Besides the $c\bar{c}$ states all radially excitations are smaller than their experimental values. The trajectories are limited by the propagator pole structure, which is represented in several plots by the black dashed-dot-dotted line. With the method introduced in Section 3.2.5 the boundstates beyond the pole limit could be determined, but they are not stable enough under variations of the partitioning parameter η (see Section 4.6).

The trajectories for groundstates and radially excited states have been studied for different values of a, Fig. 4.11 shows exemplary the results for $a = 1$ GeV^3. The structure is in principle similar to Fig. 4.10: the groundstates are more or less constant for varying ω and the radially excited states are located on trajectories. The range of ω and M where boundstates could be found is enhanced due to the fact that the pole structure is different and the pole limit is shifted to higher values of χ, compare Eq. (3.15). The first excitation of the pion is close to the experimental value for $\omega = 0.65$ GeV. Concerning the vector mesons the deviations between groundstates and experimental values are enlarged compared to the case of $a = 0.5$ GeV^3. The relative deviation rises up to 30 per cent for the ϕ meson. It turned out that for $a \approx 0.5$ GeV^3 at least the groundstates of the considered mesons in Fig. 4.10 and 4.11, pseudoscalar and vector mesons, can be described best.

In Fig. 4.12 the results for D and D_s mesons are exhibited, in the upper panel (Fig. 4.12a) for $a = 0.5$ GeV^3 and in the lower panel (Fig. 4.12b) for $a = 1$ GeV^3. In Fig. 4.12a boundstates for D meson could be found only for a small interval of ω. All the found groundstates are larger than the groundstate masses of the D_s meson, they have the irregular behaviour as mentioned in Section 4.1. The D_s groundstates for $\omega > 0.42$ GeV form a smooth trajectory which is more or less closed to the experimental value with a deviation between 50 and 150 MeV. The groundstates for $\omega \leq 0.42$ GeV form another trajectory with continuous slope. They are obtained by finding the first root of the determinant function (3.30), but in principle they belong to the trajectory of the second radially excitations (compare Fig. 3.3). Fig. 4.12b concerning $a = 1$ GeV^3 is similar to Fig. 4.12a: the two trajectories in the upper left region, one for D and one for D_s groundstate, correspond systematically to the trajectories of the second radially excitations. The groundstate masses for D_s for $\omega > 0.44$ GeV are not as closed to the experimental value as in the case $a = 0.5$ GeV^3. For D meson, more boundstates are found, and in the interval $\omega \in [0.54, 0.75]$ GeV the irregular behaviour $M_D > M_{D_s}$ is reversed.

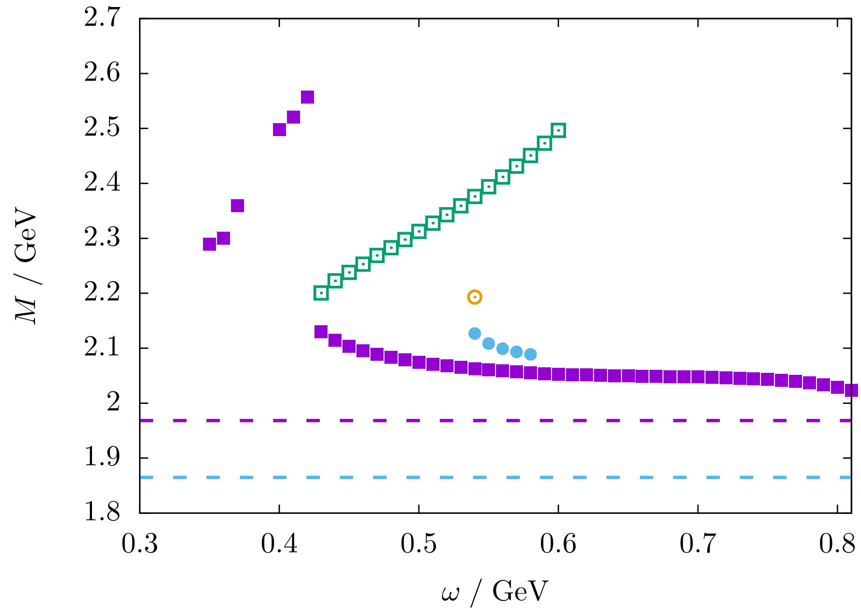

(a) $a = 0.5\ \mathrm{GeV}^3$

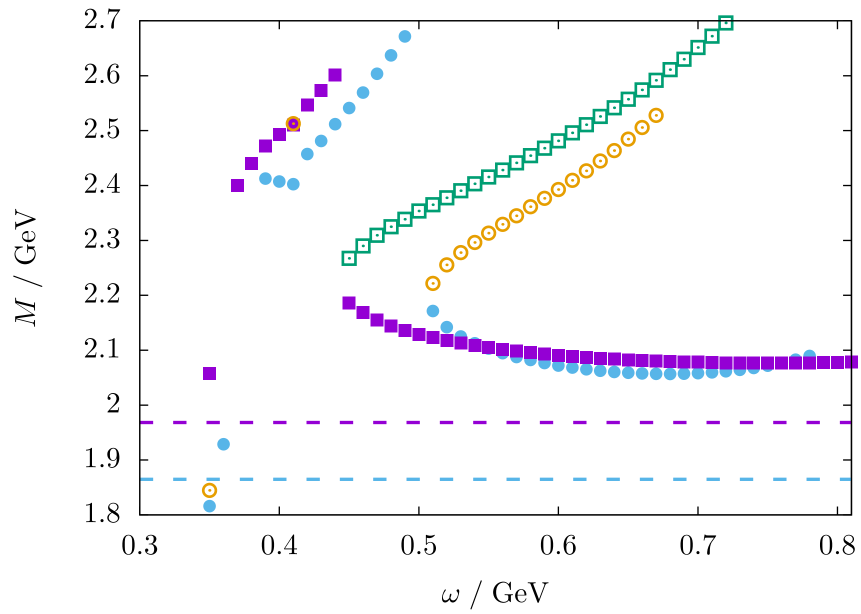

(b) $a = 1\ \mathrm{GeV}^3$

Figure 4.12: Variations of D (filled blue circles) and D_s (filled violet boxes) groundstate masses and radially excited states (empty yellow circles for D and empty green boxes for D_s) as a function of ω for $a = 0.5\ \mathrm{GeV}^3$ in the upper panel and $a = 1\ \mathrm{GeV}^3$ in the lower panel. Dashed blue line: experimental value of D groundstate mass, dashed violet line: experimental value of D_s groundstate mass.

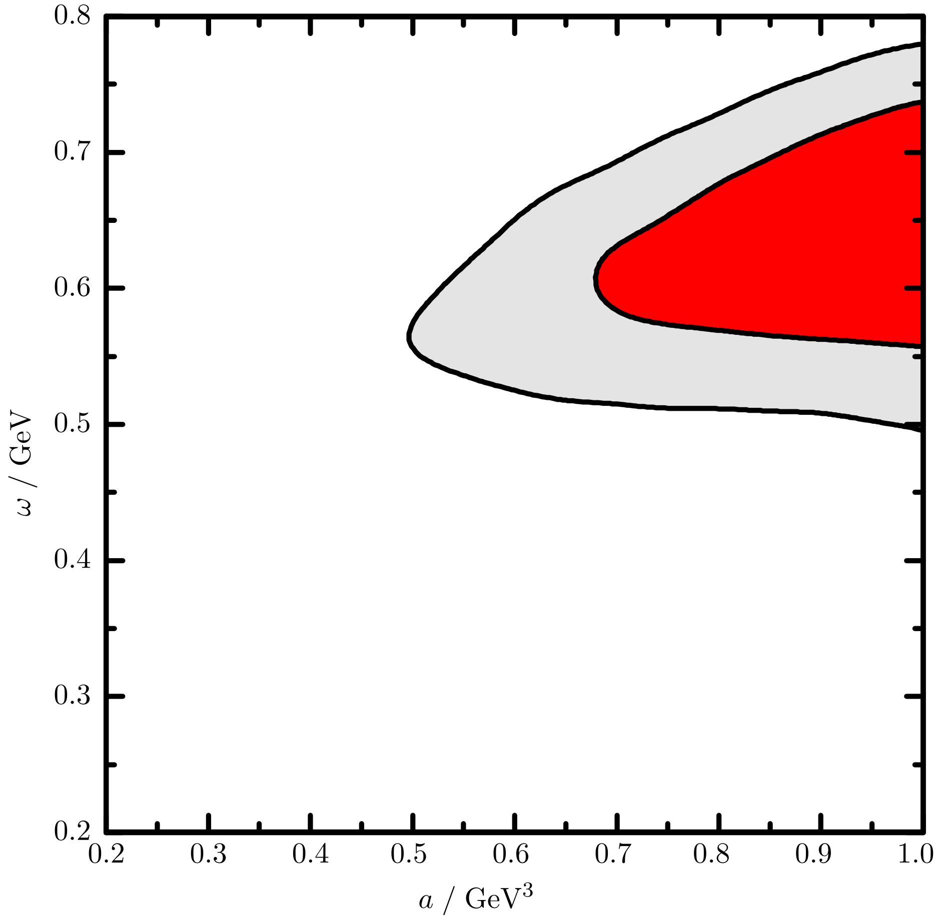

Figure 4.13: Selected regions concerning D and D_s mesons as function of ω and a. White: no D groundstate, grey: D groundstate with $M_D > M_{D_s}$, red: D groundstate with $M_D < M_{D_s}$

The existence of a D groundstate and the reversing of the irregular behaviour can be analysed a bit more in the parameter space of a and ω , see Fig. 4.13. In the white region no groundstate for the D meson could be found. In the grey region D groundstates are found, but the mass M_D is smaller than the D_s meson mass M_{D_s}. Only in the red region both, D and D_s groundstates could be found and the relation $M_D < M_{D_s}$ is fulfilled. With this observation it is better to say the irregular or unphysical behaviour is parameter dependent and not model dependent at all, as mentioned in the first section of this chapter. For obtaining the quark masses m_u, m_s and m_c the procedure introduced in Section 4.1 and illustrated in Fig. 4.6 has been used.

In [27] [1] the masses of D and Ds have been calculated at $\omega = 0.6$ and $a = 0.6$ with the relation $M_D < M_{D_s}$, which seems to be in contrast to the result depicted in Fig. 4.13. It must be taken into account that in [27] the c quark mass m_c is adjusted with the experimental value of the D mass M_D instead of using η_c. This example shows that with different procedures for fixing and optimising the model parameters ω, D, m_u, m_s and m_c the results and conclusions can be different.
Anyway, no set of parameters ω and a could be found, where the groundstates of pion, kaon and η_c could be used for fixing the quark masses m_u, m_s and m_c to obtain a good description of the D and D_s states close to their experimental data. Also no boundstates of D^* and D_s^* mesons could be found without increasing $\mathrm{M_{q\bar{q}}}$ to be beyond the pole limit.

An interesting idea has been picked up in [56] and used e.g. in [28]: The parameters ω and D are not unique, but can depend on the energy scale of the meson masses. That means, for each quark-antiquark combination, the parameters are a little bit different. This represents the scale dependency of α_{QCD}, which is implicitly included in the interaction kernel [56].
To find for each meson a own set of parameters, which can make useful "predictions", it is necessary to have more experimental boundstates for comparing, that means more J^{PC} channels must be included. In the present thesis only pseudoscalar and vector mesons are considered. But anyway, it is possible to use three of the four $c\bar{c}$ states $\eta_{c,0}$, $\eta_{c,1}$, J/ψ_0 and J/ψ_1, to fix the model parameters ω, D and m_c, take a look at the fourth radially excited boundstate and then apply these parameters to the light mesons containing u and s quarks.

In an explicit calculation, m_c and ω are fixed at the experimental values of $\eta_{c,0}$ and $\eta_{c,1}$ from PDG [44]. Then, a was varied to minimise the variance between calculated and experimental values of J/ψ_0 and J/ψ_1. The result is

$$\omega = 0.779\mathrm{GeV},\ a = 0.495\mathrm{GeV}^3\,(D = 1.726\mathrm{GeV}^{-2}),\ m_c = 1.120\mathrm{GeV}. \tag{4.5}$$

[1] As an additional check all the results from [27] which are calculated with the AWW kernel have been recalculated with the implementation of this thesis and they coincide.

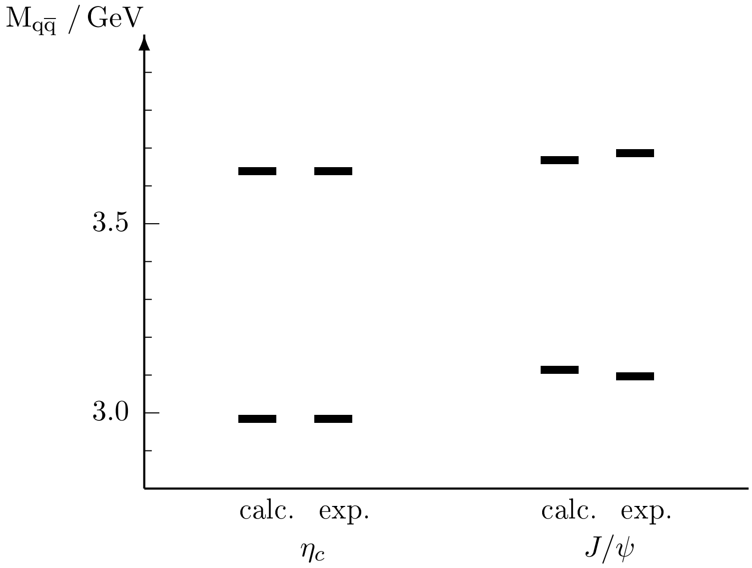

Figure 4.14: Pseudoscalar and vector meson $c\bar{c}$ boundstates for the optimised parameters ω, a and m_c of Eq. (4.5). Two parameters have been used to fix the masses of the groundstate and the first radially excited state of η_c to the experimental values, the third parameter was varied to minimise the variance between the J/ψ boundstates and their experimental values.

The corresponding meson masses are plotted in Fig. 4.14. The difference between the vector states and their experimental reference [44] is around 18 MeV, which is quite low. Applying this parameters to the heavy-light mesons it was possible to find a D_s groundstate at about 2 GeV for $m_s \geq 65$ MeV; a D boundstate has not been found. Searching for light mesons has been done with less success, not even one boundstate could be found for quark masses $m_u, m_s \leq 200\,\text{MeV}$. For understanding this observation the next section will be helpful.

The conclusion of this section is that the groundstates of pseudoscalar and vector mesons can be reproduced best for the choice $a = (0.5 \pm 0.005)\,\text{GeV}^3$. With this fixation of the parameter a the other model parameter ω can be varied over a large range obtaining stable groundstate results which are close to the experimental values within a deviation smaller than 100 MeV. For pions, kaons, ρ, K^*, ϕ and the $c\bar{c}$ meson groundstates the range of ω is only limited by the pole structure, for D_s meson the range is $\omega \in [0.5, 0.8]\,\text{GeV}$. The parameter ω could be adjusted to obtain the experimental mass of the first radially excited state of the mesons. Unfortunately, only for the $c\overline{c}$ mesons the first radially excitation can be found without passing the pole limit. It only can be guessed that the virtual extension e.g. of the trajectory of the first pion excitations crosses the experimental value at $\omega \approx 0.7...0.8\,\mathrm{GeV}$. It is also of value to think about the idea that not every theoretical boundstate is found in experiment, but for example each second state. If the second radially excitation corresponds to the experimental first radially excitation, the chosen value of ω for the $c\overline{c}$ mesons would be $\omega \approx 0.56\,\mathrm{GeV}$. It could be guessed that one trajectory of pion, ρ and ϕ meson crosses the experimental value of the first radially excitation in the region of this value of ω. Nevertheless a good statement about the adjustment of ω can be only done if the higher radially excitations of all mesons are calculated explicitly and this will be continued in Section 4.6. Beside the D_s meson it turned out that the boundstate masses of the heavy-light pseudoscalar and vector mesons can not be described very well regardless of the choice of the model parameters. It seems that the chosen model is limited in this point and only for mesons where the difference of the current quark masses is not to large a good description of the mass spectrum could be found. This is not too much amazing, because the model underlies the introduced truncation scheme and it could be expected that it exists a limit, up to which it works quite good and beyond this limit it works not so well.

4.4 Chiral condensate $\langle \overline{q}q \rangle^0$

The chiral condensate $\langle \overline{q}q \rangle^0$ is nothing else than the trace over the propagator of a massless quark,

$$\langle \overline{q}q \rangle^0 = -\frac{3}{2\pi^2} \int k^3 \sigma_s(k) dk. \tag{4.6}$$

Fig. 4.15 shows the chiral condensate in dependence of the model parameters ω and D. The violet dashed curve depicts a renormalisation point independent reference calculated in [43]. This curve is very nearby the often used value of $a = 0.5\,\mathrm{GeV}^3$ in the interval $\omega \in [0.3, 0.5]$ GeV. The green dotted curve depicts another reference [21], which is a current lattice QCD value. In the red coloured area for larger values of ω the condensate is more and more vanishing. A vanishing chiral condensate indicates that DCSB is not longer fulfilled and it could not be expected to get trustable results for light

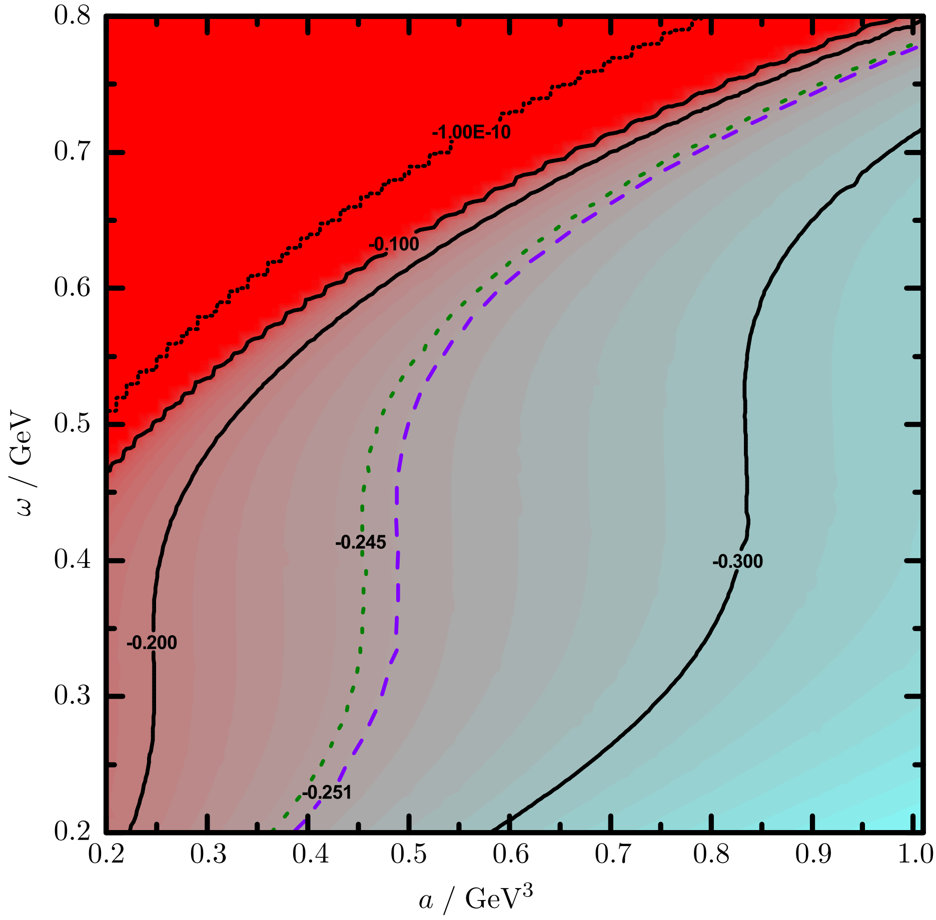

Figure 4.15: Contour plot of the chiral condensate $(\langle \bar{q}q \rangle^0)^{1/3}$ in units of GeV for $m = 0\,\mathrm{MeV}$ as a function of ω and a. The coloured curves represent calculated values from the literature (long-dashed violet: [43], short-dashed green: [21])

meson states in this region. For larger ω and constant value of a the peak in the scalar kernel function (2.10) becomes wider and more flat, which is unfavourable for forming boundstates. Comparing with Fig. 4.10 it can be seen that, in the region where the chiral condensate vanishes, the pole structure comes closer to small quantities of $\eta\,\mathrm{M}_{\mathrm{q\bar{q}}}$ and constrains the localisation of boundstates. In contrast, heavy mesons can be good described in the region where the condensate $\langle \bar{q}q \rangle^0$ vanishes. It could be found groundstates and radially excitations, even with the right gap between the first excitation and the groundstate (see the latter section). The pole structure does not change in a manner that it disturbs the calculations of $c\bar{c}$ masses. It can be argued that DCSB does not affect heavy mesons as much as light mesons. The bare mass of the c quarks is larger than the dynamical generated mass in $c\bar{c}$ boundstates. The important role of DCSB is to explain the masses of light mesons, especially the pion.

4.5 Regge behaviour

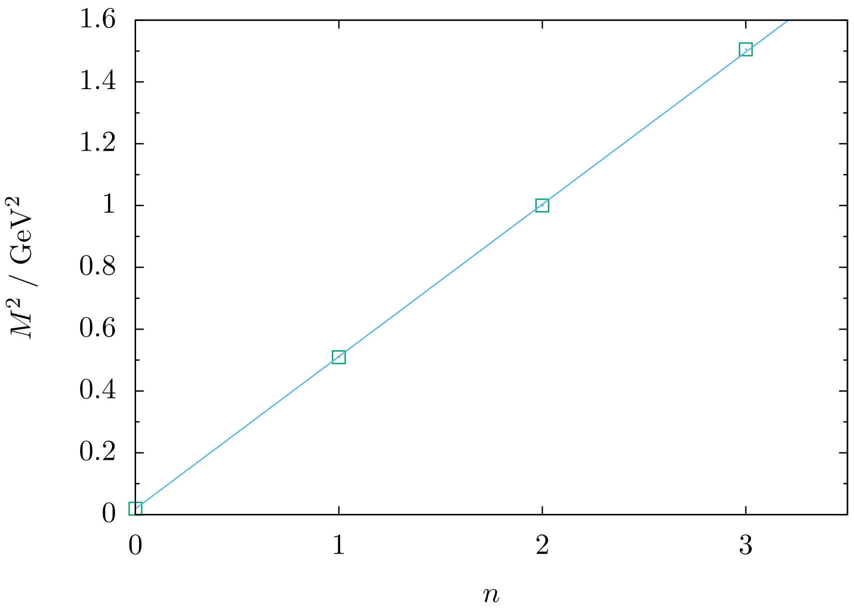

Figure 4.16: Regge trajectory for pion boundstates, $\omega = 0.32$ GeV, $a = 0.5$ GeV^3. The blue empty boxes represent the boundstates, n is the number of radially excitation. The blue line depicts the fitted Regge trajectory.

If at least three boundstates for a meson are found they can be used to fit a Regge trajectory (2.11). In particular, a function $M^2(n) = a + \beta n + cn^2$ can be fitted to the squared boundstate masses (see Fig. 4.16), where a is the intercept, β represents the slope of the Regge trajectories and c is a measure for the quality of them, quantifying the deviation from a linear trajectory.
In Fig. 4.17 the quadratic masses of the pseudoscalar boundstates from Fig. 4.10 and the corresponding Regge coefficients are plotted. For all considered mesons the coefficients β are much larger than the coefficients c which means that Regge behaviour can be asserted. For every meson, a value of ω exists, where the ratio c/β becomes minimal. For the pion it is $\omega = 0.33$ GeV, for

the kaon $\omega = 0.31$ GeV, for the hypothetical $s\bar{s}$ state $\omega = 0.36$ GeV and for η_c $\omega = 0.52$ GeV. The same considerations have been done for the pseudoscalar boundstates of Fig. 4.11, see Fig. 4.17. In the case of $a = 1\,\text{GeV}^3$ the range of ω, where at least three boundstates can be found, is larger than in the case of $a = 0.5\,\text{GeV}^3$. The values of ω, where the ratio c/β becomes minimal are as follows: For pions $\omega = 0.39$ GeV, for kaons $\omega = 0.4$ GeV, for the hypothetical $s\bar{s}$ state $\omega = 0.41$ GeV and for η_c $\omega = 0.63$ GeV. The trend is, for mesons with larger quark masses $m_{q_{1,2}}$ the value of ω with the best regge trajectory becomes larger.
For the vector meson boundstates from Fig. 4.10 and 4.11 it is also possible to calculate the Regge coefficients a, β and c. As mentioned in Section 4.3 for ρ, ϕ and J/ψ the difference between two boundstates is much smaller than the difference between the other boundstates. Therefore the ratio $|c/\beta|$ becomes much larger than in the pseudoscalar case which means that Regge behaviour can not be asserted.

It is hard to decide how accurately Regge behaviour is implemented in the experimental values of pseudoscalar mesons. Only for pions at least three boundstates are known with $M_{\pi_0} = 0.140$ GeV, $M_{\pi_1} = (1.300 \pm 0.100)$ GeV and $M_{\pi_2} = (1.812 \pm 0.012)$ GeV [44]. Because of the large uncertainty of M_{π_1} it is possible to find a Regge trajectory for this boundstates.

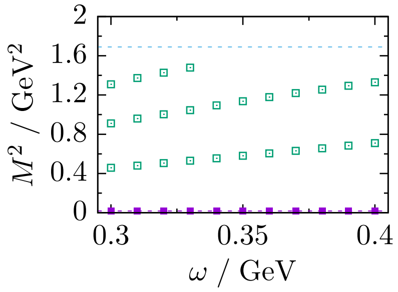

(a) π

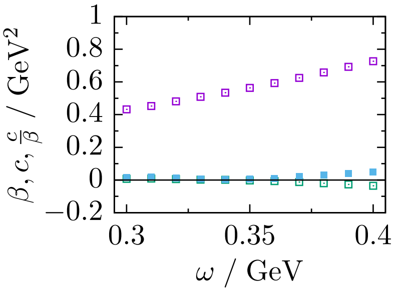

(b) Regge coefficients π

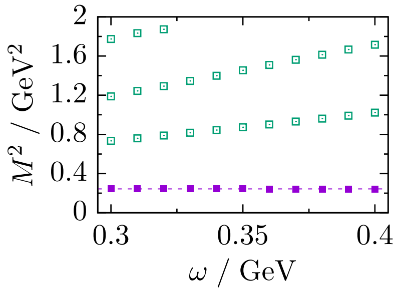

(c) K

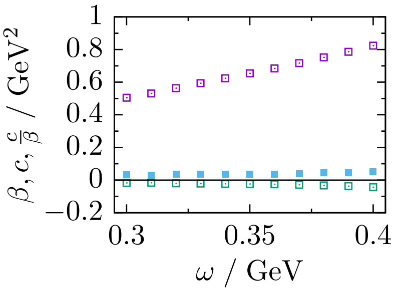

(d) Regge coefficients K

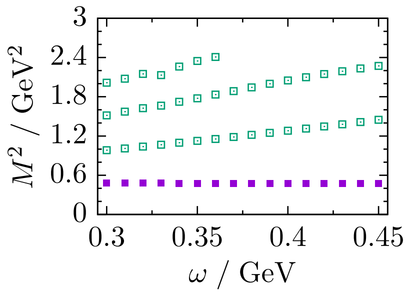

(e) $s\bar{s}$

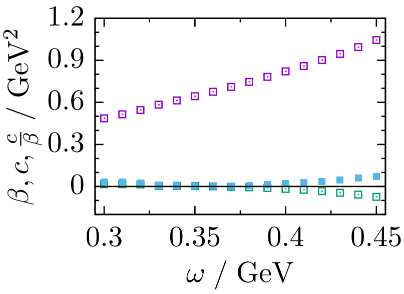

(f) Regge coefficients $s\bar{s}$

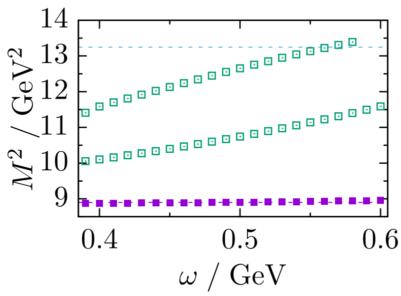

(g) η_c

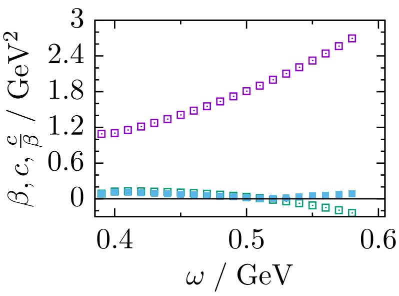

(h) Regge coefficients η_c

Figure 4.17: Regge behaviour for $a = 0.5\,\mathrm{GeV}^3$ and varying ω; left column: squared masses of boundstates in units of GeV^2, right column: Regge coefficients β (empty violet), c (empty green) and $|c/\beta|$ (filled blue); a is identical to M_0^2.

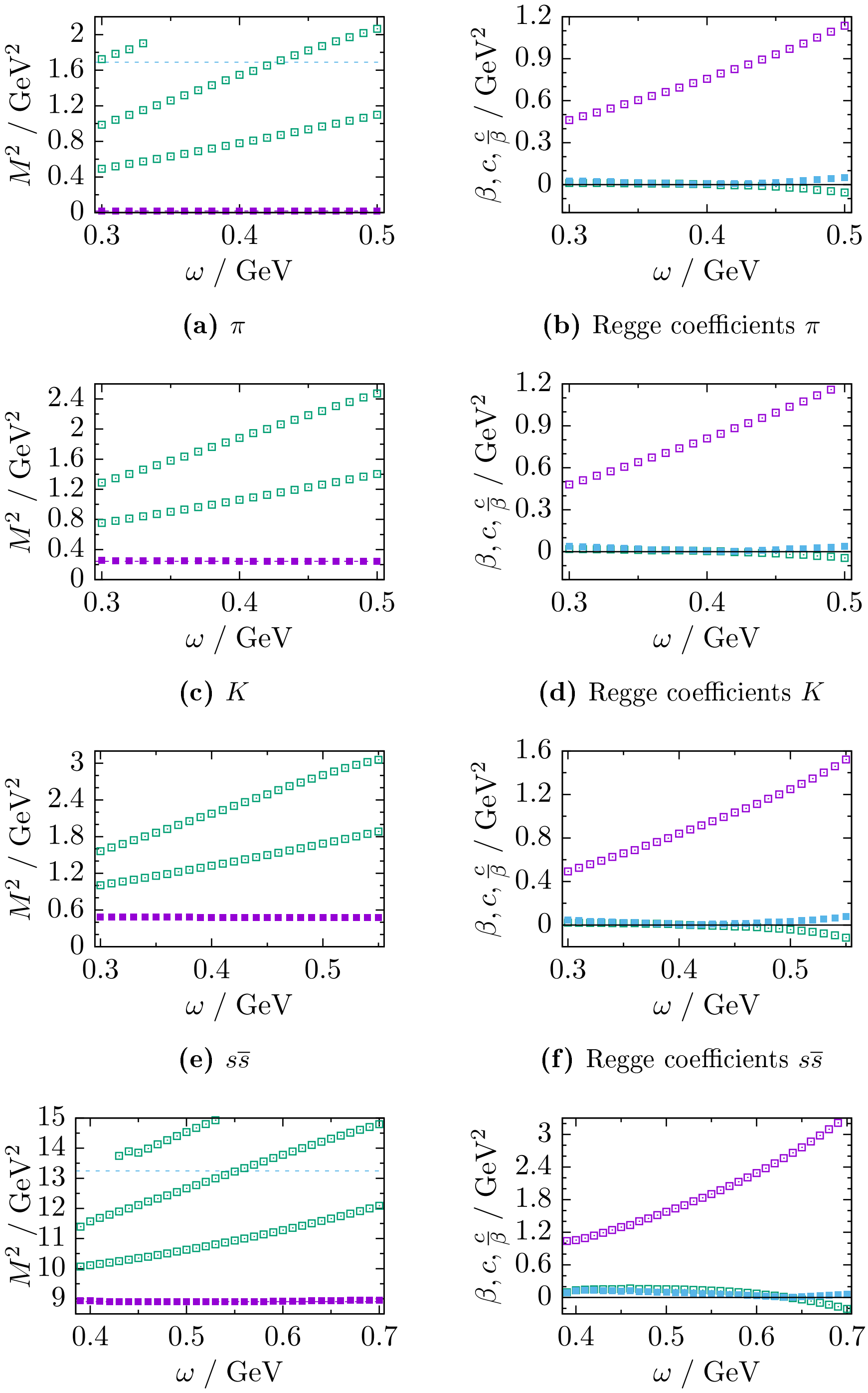

(a) π **(b)** Regge coefficients π

(c) K **(d)** Regge coefficients K

(e) $s\bar{s}$ **(f)** Regge coefficients $s\bar{s}$

(g) η_c **(h)** Regge coefficients η_c

Figure 4.18: As Fig. 4.17 but for $a = 1\,\mathrm{GeV}^3$.

4.6 Unstable results beyond the pole limit

One of the goals in this thesis it was to handle the pole structure explicitly. As mentioned at some places in the last sections, some unstable results appeared in the sense of varying values of meson masses for different choices of the partitioning parameter η. In the following, two examples are given where these unstable results have been observed.

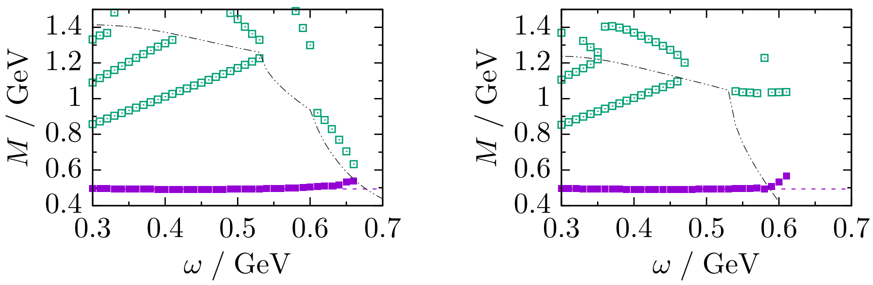

(a) optimal η **(b)** $\eta = 1/2$

Figure 4.19: Comparing the calculated boundstates (groundstates: violet filled boxes, excited states: empty green boxes) of $K = u\bar{s}, \bar{u}s$ for different partitioning parameter η. Beyond the pole limits (black dashed-dot-dotted curves) the structure is completely different. In the right panel, the pole limit is determined by the u quark poles, in the left panel the limit is determined as described in Subsection 3.2.4.

In Fig. 4.19, again the groundstate masses and the first few radial excitations of the kaon in dependence on the model parameter ω are plotted (the left side is for optimal $\eta = \eta_{opt}$ and the right side for constant $\eta = 0.5$). It can be seen that below the pole limit (black dashed-dot-dotted curves) the trajectories of the boundstates are identical except numerical deviations smaller than 0.1 MeV. But beyond the pole limit the trajectories suddenly change. Their straight-line behaviour vanishes and the further trend is completely different in both plots.

In Fig. 4.20, the determinant function (3.30) of the pion for different η at the common benchmark from Section 4.1 is plotted. The logarithmic scale is chosen because for boundstate masses $\mathrm{M}_{\mathrm{q}\bar{\mathrm{q}}} > 1$ GeV the value of the determinants has a completely different scale. The roots can be identified at the sharp peaks which point in direction of the x-axis. It can be seen that the curves are on top of each other in the region without poles ($\mathrm{M}_{\mathrm{q}\bar{\mathrm{q}}} < 0.9$ GeV).

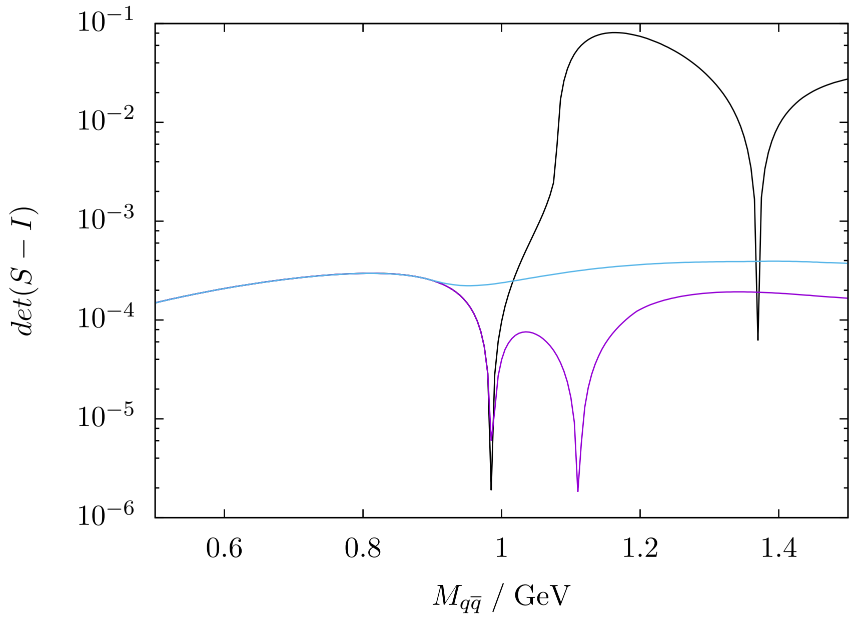

Figure 4.20: Determinant function (3.30) of pions for different partitioning parameter η in the range $\mathrm{M}_{\mathrm{q\bar{q}}} \in [0.5, 1.5]$ GeV at the benchmark from section 4.1. Black curve: $\eta = 0.5$, violet curve: $\eta = 0.55$, blue curve: $\eta = 0.6$

Then, going to larger values of $\mathrm{M}_{\mathrm{q\bar{q}}}$ the curve for $\eta = 0.6$ is separated, exactly at the mass $\mathrm{M}_{\mathrm{q\bar{q}}}$ which corresponds, via relation (3.13), to the first pole of the u quark. The curve continues smoothly without roots in the considered region. Just behind the first excitation of the other both curves the curve for $\eta = 0.55$ is separated analogously. The roots for the second excitation are completely different for $\eta = 0.55$ and $\eta = 0.5$.

The above examples give an indication for an incorrectness of the done calculations in the pole region. The method introduced in Section 3.2.5 reproduces the boundstate spectrum of all considered mesons accurately in the region without poles, no matter how many poles are taken into account, compared to the calculations without poles. Even the propagator functions $\sigma_{s,v}(p^2)$ for arbitrary complex arguments, which are consistent with the considerations in Appendix B, coincide, independently of whether they are calculated directly with the “brute force” method or with Eq. (3.10). The analytically properties of Eq. (3.39) are well known and the corresponding numerical parameters and routines are tested more than adequate, so the method from Section 3.2.5 works.

For finding the reason of the unusual behaviour in Fig. 4.19 and 4.20 it is helpful to go back to Eq. (2.6). After the introduced truncations are done, the BSE has been transformed into the Euclidean space by using Equations (C.1)-(C.4) to obtain the tBSE (2.8). This is the usual procedure which is found in many publications (e.g. [7, 8]) concerning to tDSE and tBSE; often the tBSE in Euclidean space is taken for granted without derivation (e.g. [16, 31]). After applying and implementing Eq. (3.11) for the propagator functions $\sigma_{s,v}(p^2)$ it is known, that they have poles in the region $\mathrm{Re}(p^2) < 0$. For the calculations in this thesis only a finite number of poles is important, but in principle it can not be said that the number of poles is finite and it could be guessed that there is an infinite number of poles. But anyway, the poles $\tilde{k}^2_{0,i}$ can be sorted systematically by the value of χ_i (3.13). In the following, only the poles of one quark are considered. The poles are located in the complex $\tilde{k}^2$ plane of the Euclidean vector k^E. Translated into the complex k_0 plane,

$$\tilde{k}^2_{0,i} = -(k_0 + \eta_1 \, \mathrm{M}_{\mathrm{q\bar{q}}})^2 + \vec{k}^2 \tag{4.7}$$

$$k_0 + \eta_1 \, \mathrm{M}_{\mathrm{q\bar{q}}} = \sqrt{\vec{k}^2 - \tilde{k}^2_{0,i}} \tag{4.8}$$

$$k_0 = -\eta_1 \, \mathrm{M}_{\mathrm{q\bar{q}}} \pm \sqrt{\vec{k}^2 - \tilde{k}^2_{0,i}} \equiv k_{0,i}^{I,II}, \tag{4.9}$$

a pole at $\tilde{k}^2_{0,i}$ results into two poles $k^I_{0,i}$ and $k^{II}_{0,i}$. The argument of the square root in Eq. (4.9) has a positive real part, because $\vec{k}^2$ is positive and $\mathrm{Re}(\tilde{k}^2_{0,i})$ is always negative. From Section 3.1.3 it is known that each pole arises as pair of poles together with $\tilde{k}^{2*}_{0,i}$. The corresponding poles in the k_0 plane are

$$k_0 = -\eta_1 \, \mathrm{M}_{\mathrm{q\bar{q}}} \pm \sqrt{\vec{k}^2 - \tilde{k}^{2*}_{0,i}} \tag{4.10}$$

$$= -\eta_1 \, \mathrm{M}_{\mathrm{q\bar{q}}} \pm \sqrt{\vec{k}^2 - \tilde{k}^2_{0,i}}^{\,*} \equiv k_0^{III,IV}, \tag{4.11}$$

where $k^{III}_{0,i} = k^{I*}_{0,i}$ and $k^{IV}_{0,i} = k^{II*}_{0,i}$.

The couple of four poles $k_{0,i}^{(I-IV)}$ in the k_0 plane correspond to the pair of poles $\tilde{k}^2_{0,i}$ and $\tilde{k}^{2*}_{0,i}$ in the Euclidean $\tilde{k}^2$ plane. For fixed $\vec{k}^2 = 0$ this couple is illustrated in Fig. 4.21. The structure is similar to a cross (square root terms) with the crossing point on the real axis, shifted by $-\eta_1 \, \mathrm{M}_{\mathrm{q\bar{q}}}$.

If $\vec{k}^2 \neq 0$, the position of the poles $k_{0,i}^{(I-IV)}$ changes, see Fig. 4.22. It can be seen that for rising $\vec{k}^2$ the absolute value of the square root $\sqrt{\vec{k}^2 - \tilde{k}^2_{0,i}}$ rises

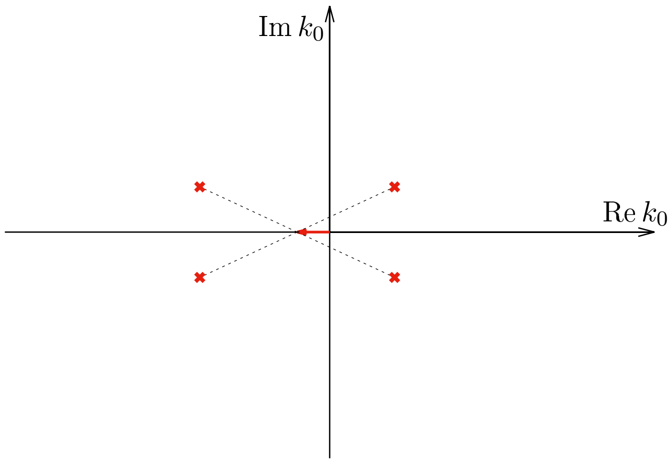

Figure 4.21: Couple of four poles in the complex k_0 plane. The black dotted lines represent the contribution of the square root terms in Eq. (4.9) and (4.11). The red arrow depicts the shift of the crossing by $-\eta_1\, \mathrm{M}_{\mathrm{q\bar{q}}}$.

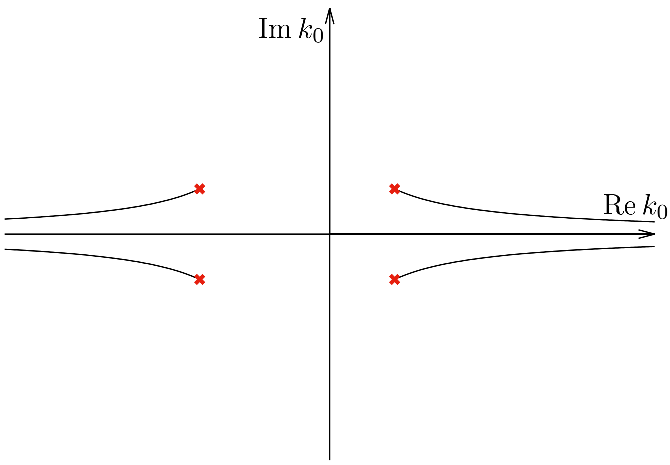

Figure 4.22: Trajectories of one couple of poles in the complex k_0 plane for rising $\vec{k}^2$ from 0 to ∞. For large $\vec{k}^2$ each trajectory stays in one quadrant and does not cross an axis of the coordinate system.

and the phase angle of the argument $\arctan[\mathrm{Im}(arg)/\mathrm{Re}(arg)]$ decreases and goes to zero for $\vec{k}^2 \Rightarrow \infty$.

As mentioned above, the number of poles can be arbitrary large, so each pair of complex conjugated poles $\tilde{k}^2_{0,i}$ gives a couple of four poles in the k_0

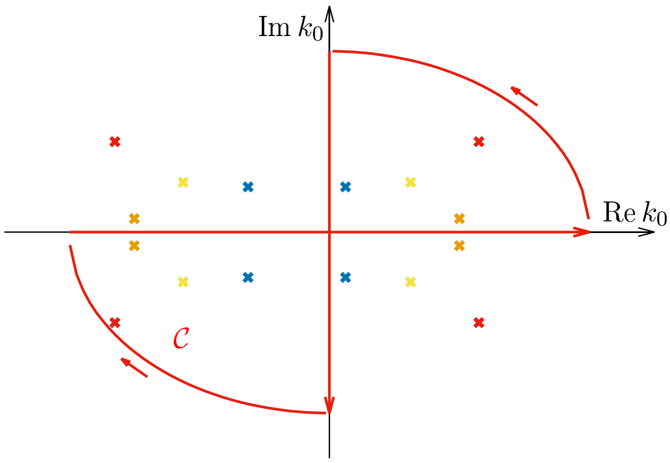

Figure 4.23: Integration contour for Wick's rotation in the complex k_0 plane with an arbitrary number of couples of poles (crosses).

plane, as illustrated in Fig. 4.23 by different colours for different couples. In Fig. 4.23 also the integration contour $\mathcal{C}$ for Wick's rotation is depicted in red, for details see Appendix C. Each pole, which is located inside the contour $\mathcal{C}$, gives a contribution to the integral $\int dk_0$ or $\int dk_4$. It has to be shown that the contributions of two k_0 poles of the same couple, which are located in two opposite (diagonal) quadrants, cancel each other. It is intuitive that they cancel each other and practically it turned out that there are no contributions, because almost η independent results are obtained. The other two poles of each couple are outside the integration contour and do not contribute to Wick's rotation. Therefore, if the poles are located in such a way, that for each $\vec{k}^2$ each of the four poles is located in a different quadrant, the transition rule (C.1) is correct and hence (2.8) applies.

Although it is not proven exactly that the contributions in the above case cancel each other, a systematically different case occurs if the couple of poles is shifted as far as two of them cross the imaginary axis, see Fig. 4.24. That means, it exists a $\chi_{crit} = \eta_1 \, \mathrm{M}_{q\bar{q}}$, where two poles are located on the imaginary axis (for $\vec{k}^2 = 0$) and for $\chi > \chi_{crit}$ it exists a $\vec{k}^2_{crit}$, where in the range $\vec{k}^2 \in [0, \vec{k}^2_{crit}]$ the two considered poles are across the imaginary axis (in this case, where we consider the poles of the first quark, two poles are located in the upper left quadrant and two poles are located in the lower left

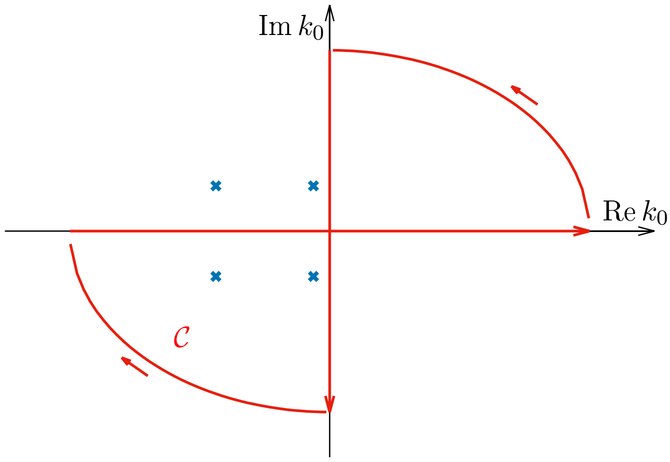

Figure 4.24: Integration contour for Wick's rotation in the complex k_0 with one couple of poles (crosses) for $\chi > \chi_{crit}$.

quadrant). It can be shown that $\chi_{crit} = \chi_i$, where χ_i is the characteristically quantity of the pole $\tilde{k}^2_{0,i}$, and $\vec{k}^2_{crit}$ is given by

$$\vec{k}^2_{crit} = \chi^2_{crit} + \mathrm{Re}(\tilde{k}^2_{0,i}). \tag{4.12}$$

For this pole structure the contributions to Wick's rotation change. The upper right pole leaves the contour $\mathcal{C}$ and the lower right pole enters the contour. It can be supposed that the contributions of the two poles in the lower left quadrant do not cancel each other anymore.

For the above considerations the assumption has been made that the singularities found in the Euclidean propagator functions can be transformed into Minkowski space by using $k^2_M = -k^2_E$. In principle, to be sure that the propagator functions in Minkowski space have a corresponding pole structure as found in the Euclidean space, the Dyson-Schwinger equation has to be solved directly in Minkowski space or an analytically continuation has to be found [48]. For solving the Dyson-Schwinger equation directly in Minkowski space, the kernel (2.10) has to be transformed into Minkowski space, which means that the exponent in the exponential function becomes positive and the integral diverges. Until yet many attempts have been made to find an analytically continuation of the propagator functions (e.g. by using Nakanishi representation [42]), which are not completely successful. Anyway, to justify the assumption as an example the undressed propagator in Minkowski space

$$D_M(p^2) = \frac{1}{p_M^2 - M^2} \tag{4.13}$$

is considered. It has a pole at $p_M^2 = M^2 \to p_0 = \pm\sqrt{M^2 + \vec{p}^2}$. The Wick-rotated propagator in the Euclidean space reads

$$D_E(p^2) = \frac{-1}{p_E^2 + M^2}, \tag{4.14}$$

and has a pole at $p_E^2 = -M^2 \to p_4 = \pm i\sqrt{M^2 + \vec{p}^2} = ip_0$. The propagators are different in Minkowski space and in Euclidean space, but the poles can be transformed with the use of $k_M^2 = -k_E^2$.

Up to here only the poles of the first quark propagator are considered, but each pair of conjugated poles of the second quark propagator leads also to a couple of four poles in the complex k_0 plane. Their positions can be described with Eq. (4.9) and (4.11), replacing $\eta_1\,\mathrm{M}_{\mathrm{q\bar{q}}}$ by $-\eta_2\,\mathrm{M}_{\mathrm{q\bar{q}}}$ and the corresponding pole positions. That means in the case of equal quark masses $m_{q_1} = m_{q_2}$ and $\eta_1 = \eta_2$ the structure of poles in the k_0 plane of the second quark is similar to the one depicted in Fig. 4.21 but the "cross" is shifted to the right and not to the left. When raising the value of $\chi = \eta_1\,\mathrm{M}_{\mathrm{q\bar{q}}} = \eta_2\,\mathrm{M}_{\mathrm{q\bar{q}}}$ above χ_{crit} two poles of the first quark cross the imaginary axis from the right to the left at the same point when two poles of the second quark cross from the left to the right. In this case the contributions to Wick's rotation cancel each other, because both propagators have the same pole structure with the same residues. It seems that in the equal mass case with $\eta_1 = \eta_2$ the value of $\mathrm{M}_{\mathrm{q\bar{q}}}$ could be raised arbitrarily large without getting problems caused by pole contributions from Wick's rotation. But exactly this case has been excluded for the calculations in this thesis because of the argumentation made in the last paragraph of Section 3.2.5 (also discussed in [10]).

At last here is a short idea what to do if such a couple of poles adds a contribution to the Bethe-Salpeter equation. The resulting system would not have the simple form of Eq. (3.28), but could read

$$X_1 = S_{11}X_1 + S_{12}X_2 \tag{4.15}$$

$$X_2 = S_{21}X_1 + S_{22}X_2, \tag{4.16}$$

where X_1 is similar to X from Eq. (3.29) (if the hyperspherical decomposition is applicable) with dimension $N = N_1 = \alpha_{max} \times N_{gegbau} \times N_G$ and X_2 is the reduced tBSE solution with $p_0 = k_0^I$, which means X_1 has the dimension $N_2 = \alpha_{max} \times N_G$. Therefore S_{11} is of dimension $N_1 \times N_1$, S_{12} is of dimension $N_1 \times N_2$, S_{21} is of dimension $N_2 \times N_1$ and S_{22} is of dimension $N_2 \times N_2$. A comparable solving structure can be found in [35], concerning poles of a various kernel (a few additional comments can be found in [23], a classification of poles and their behaviour within Wick's rotation is exemplary given in [45]).

5 | Summary and Outlook

In this thesis, the non-perturbative formalism of Dyson-Schwinger equations and Bethe-Salpeter equation for finding mesonic QCD boundstates has been presented. The quark Dyson-Schwinger equation has been used for finding the solution of the quark propagator. The Bethe-Salpeter equation has been used as a gap equation for finding the boundstate masses of pseudoscalar and vector mesons with u/d, s and c quarks as constituent quarks.
In the first part of this thesis a model interaction has been recalled to solve both, the Dyson-Schwinger equation and the Bethe-Salpeter equation consistently with taking care of the axial-vector Ward-Takahashi identity and the Goldstone theorem. This model contains three parameters for the truncated Dyson-Schwinger equation (current quark mass, interaction strength and interaction range) and an additional parameter in the truncated Bethe-Salpeter equation (current quark mass of second quark). In the second part the implementation of the two integral equations has been illustrated. All technical relevant steps have been explained. The appearance of the pole structure of the propagator functions was emblazed and a new method for handling the singularities has been commented. All numerical implementations have been reapplied, that means while already Fortran implementations exist for solving tDSE and tBSE a new C++ implementation has been established. In the main part of this thesis the results are presented. First, the model parameters were set to values other groups used previously to check the correct implementation of the solving procedure. The concordance of the extracted values for meson boundstates indicates that the implementation has been done correctly. Then the model parameters have been varied systematically. The variation of the current quark masses leads to a smooth function of the boundstate masses of groundstates and excited states. In some regions some unphysical effects appeared which are in contrast to ob-

servations of other groups and which are specific for the chosen parameters of the interaction model. The variation of the two remaining model parameters showed that one parameter could be fixed to obtain stable groundstate results for mostly all considered mesons. The parameter of the interaction range then could be varied to obtain the radially excited states of certain mesons. For adding an additional constraint to the parameter space the chiral condensate has been introduced and calculated for massless quarks. It appeared a region in the parameter space, where the chiral condensate vanished. This is an indicator that chiral symmetry is restored and these parameters are not suitable for describing light mesons like the pion. The spectrum of mesons has been tested for Regge behaviour, and the interaction range parameter has been fixed for different pseudoscalar mesons to obtain a preferably linear Regge trajectory. It could be shown that the introduced method for handling the pole structure of the propagator functions works only in the region without poles and leads to unstable results in the region of poles. It could be argued that the method itself is correct, but the initial truncated Bethe-Salpeter equation in Euclidean space is incomplete in the presence of poles. It turned out that, with respect to the meson mass spectrum, the chiral condensate and the Regge trajectories for each case a different set of parameters was necessary to obtain reasonable results. Further, all these sets of parameters could not reproduce the meson spectrum of the heavy-light mesons with the correct arrangement. Therefore it can be said that the considered AWW kernel [2] is able to reproduce certain groundstate masses of pseudoscalar and vector mesons, but is not able to describe the whole meson spectrum with radially excitations by using an unique set of parameters.

In future (and even present) studies the simple AWW kernel has to be replaced by a more reliable kernel like the MT kernel [36] or the Qin-Chang kernel [46] for finding a more detailed and accurate meson spectrum. This kernels provide the correct behaviour for large momenta, which was neglected in the AWW approach. The rainbow approximation is also a very simple approach, which can be replaced by the Ball-Chiu vertex, which fulfills the full Ward-Takahashi identity [48]. But the AWW kernel should not be discarded at all. The simpleness of this kernel is also the power to gain access for handling the pole structure explicitly. Whenever a truncation scheme is applied to the Dyson-Schwinger and Bethe-Salpeter formalism unphysical singularities will appear in the solutions of the quark propagators. In the last section of the main part of this thesis an idea has been introduced, which could solve the pole problem and the AWW kernel is the most convenient starting point for exploring the applicability of this procedure. As a next step it has to be proven to which extent this method can be applied and then an implementation must show if it provides reasonable results and how stable these results are.

A | Different interaction kernels

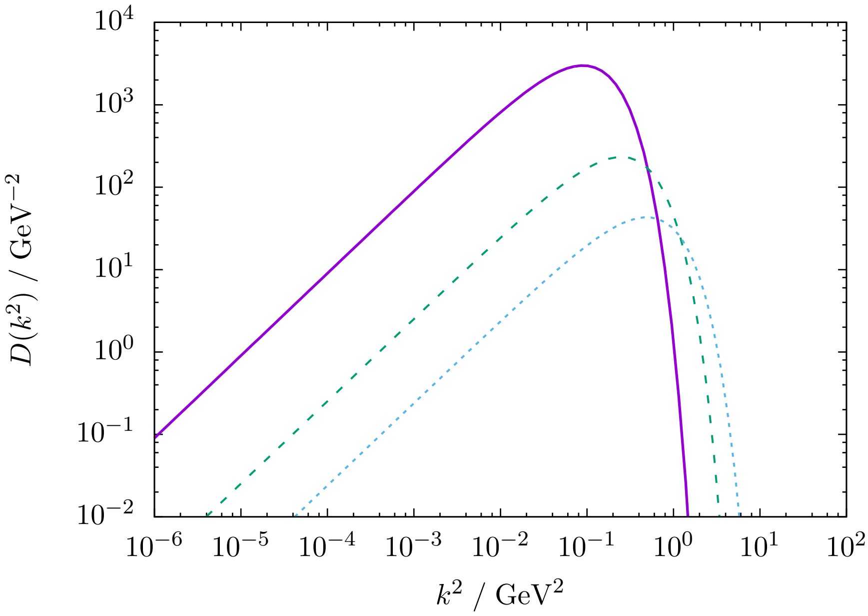

Figure A.1: Scalar kernel function (2.10) for different values of the parameters D and ω with $D\omega^5 = 0.5$ (solid violet: $\omega = 0.3\,\text{GeV}$, long-dashed green: $\omega = 0.5\,\text{GeV}$, short-dashed blue: $\omega = 0.7\,\text{GeV}$).

In Fig. A.1 the Alkofer-Watson-Weigel kernel (2.10) is plotted for different parameters D and ω with $a = D\omega^5 = 0.5\,\text{GeV}^3$. The shape of the scalar kernel function (2.10) is similar for different choices of the model parameters. The interaction range parameter ω determines the location of the peak, while the interaction strength parameter D acts only as an overall constant factor. In Fig. A.2 the AWW kernel (solid) is compared to other common used

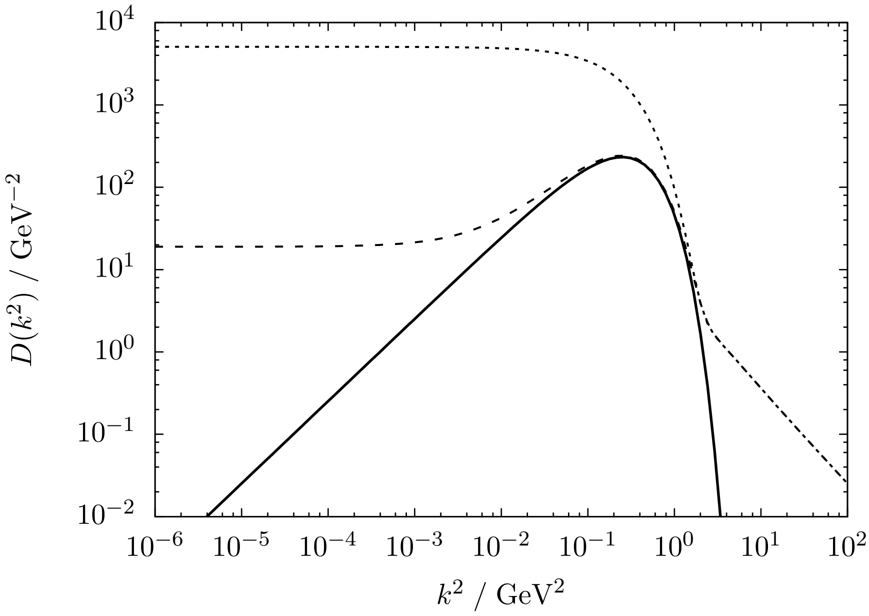

Figure A.2: Different scalar kernel functions (solid curve: AWW kernel (2.10), long-dashed curve: MT kernel (2.9), short-dashed curve: QC kernel [46]) for $D = 16\,\mathrm{GeV}^{-2}$ and $\omega = 0.5\,\mathrm{GeV}$.

kernels, the Maris-Tandy kernel (2.9) (long-dashed) and the Qin-Chang(QC) kernel [46] (short-dashed). These two kernels (MT and QC) differ from the AWW kernel both for large k^2 and for $k^2 \to 0$. For large k^2 the MT kernel and the QC kernel have the same form dominated by the UV term (see Eq. (2.9)) obtained from perturbative calculations at one-loop order. With this kernels the integrand in Eq. (2.8) does not converge fast enough and therefore renormalisation constants and a cut-off in the integral of the truncated Bethe-Salpeter equation (2.8) have to be introduced, which is not necessary in case the AWW kernel is used. Further the logarithm in the UV term leads to additional singularities, so called branch points [1], if it is tried to use the "brute force" method from Section 3.1.2 for finding the propagator functions (3.2) and (3.1) in the complex plane. For $k^2 \to 0$ the MT kernel and the QC kernel do not vanish but converge to a finite value. This can lead to troubles when calculating the partial kernels $V_\kappa(\tilde{p}, \tilde{k})$ in Eq. (3.23). A attempt to avoid this troubles has been made in [18,26] by shifting the integration variable $\tilde{k}$ in Eq. (2.8) to $\tilde{p} - \tilde{k}$ to integrate over real gluon momenta.

B | Limits of the brute force method

As mentioned above in calculating the propagator functions in the complex plane, problems appear if the imaginary part of the argument becomes large. The critical expression is located in the AWW kernel (2.10), especially the exponential function inside. At a closer look it reads

$$
\begin{aligned}
e^{-(p-k)^2/\omega^2} &= e^{-[p^2+k^2-2pkt]/\omega^2} && \text{(B.1)}\\
&= e^{-[\mathrm{Re}(p)^2-\mathrm{Im}(p)^2+2i\mathrm{Re}(p)\mathrm{Im}(p)+k^2-2\mathrm{Re}(p)kt-2i\mathrm{Im}(p)kt]/\omega^2} && \text{(B.2)}\\
&= e^{-[\mathrm{Re}(p)^2-\mathrm{Im}(p)^2)]/\omega^2} e^{-[(k^2-2\mathrm{Re}(p)kt)]/\omega^2} e^{-2i\mathrm{Im}(p)[\mathrm{Re}(p)-kt]/\omega^2}. && \text{(B.3)}
\end{aligned}
$$

The last line contains three exponential terms. The first one is a constant real factor, which does not depend on the integration variables k and $t = \cos\chi_k$, $t \in [-1, 1]$. The second term is also real, but depends on k and t. The third term has a purely imaginary exponent which can be considered as a phase. This phase can be split into a constant phase $-2\mathrm{Im}(p)\,\mathrm{Re}(p)/\omega^2$ and a variable phase $2\mathrm{Im}(p)\,kt/\omega^2$, which leads to oscillations of the integrand. What does this mean for the calculation of the propagator functions? The integration in Eq. (3.3) is done numerically with a finite mesh of integration points. The general rule for choosing the density of this mesh is to use more points where the function suffers larger variations. For an oscillating function it has turned out that it is appropriate to use at least two integration points per oscillation with a Gaussian quadrature method [30]. That means, if we hold one integration variable constant the difference between two neighbouring points of the other variable must not be larger than the phase difference becomes larger than π:

$$|2\mathrm{Im}(p)\,\Delta k\, t| \leq \pi, \tag{B.4}$$

$$|2\mathrm{Im}(p)\,k\,\Delta t| \leq \pi. \tag{B.5}$$

For the inequality of Eq. (B.4), the maximum of the left side is reached if $t = \pm 1$. This leads to the condition

$$|\mathrm{Im}(p)\,\Delta k| \leq \frac{\omega^2}{2}\pi. \tag{B.6}$$

It can be seen that $\mathrm{Im}(p)$ can not be chosen arbitrarily large. To check whether both inequalities are fulfilled in the present calculations the quantities have to be specified. For all $k \leq 2$ GeV, Δk is at most 0.0163 GeV with respect to a Gaussian mesh with 96 points in an interval $[0, 1]$. k itself is also at most 2 GeV; for larger values a parametrisation method is used. All calculations have been done for meson masses $\mathrm{M}_{\mathrm{q}\bar{\mathrm{q}}} \leq 4$ GeV. A consequence of this is that the maximal $\mathrm{Im}(p)$ is $\pm\,2$ GeV. It follows that condition (B.6) is fulfilled for $\omega \geq 0.1441$ GeV. The other condition depends on Δt, which depends on the number of points of the Chebyshev mesh,

$$n_{ch} = 16 \;\Rightarrow\; \Delta t_{max} = 0.1845 \;\Rightarrow\; \omega \geq 0.6854\ \mathrm{GeV}, \tag{B.7}$$

$$n_{ch} = 32 \;\Rightarrow\; \Delta t_{max} = 0.0952 \;\Rightarrow\; \omega \geq 0.4924\ \mathrm{GeV}, \tag{B.8}$$

$$n_{ch} = 64 \;\Rightarrow\; \Delta t_{max} = 0.0483 \;\Rightarrow\; \omega \geq 0.3507\ \mathrm{GeV}. \tag{B.9}$$

These numbers show that the numerical calculations must be controlled very carefully.

C | Wick's rotation

To transform functions from Minkowski space to Euclidean space the following rules [48] can be used:

$$\int^M d^4k^M \Rightarrow i \int^E d^4k^E, \tag{C.1}$$

$$\not{k} \Rightarrow i\gamma^E k^E, \tag{C.2}$$

$$k_\mu q^\mu \Rightarrow -k^E q^E, \tag{C.3}$$

$$k_\mu x^\mu \Rightarrow k^E x^E, \tag{C.4}$$

where $k^M = (k_0, \vec{k})$ and $k^E = (k_4, \vec{k})$.

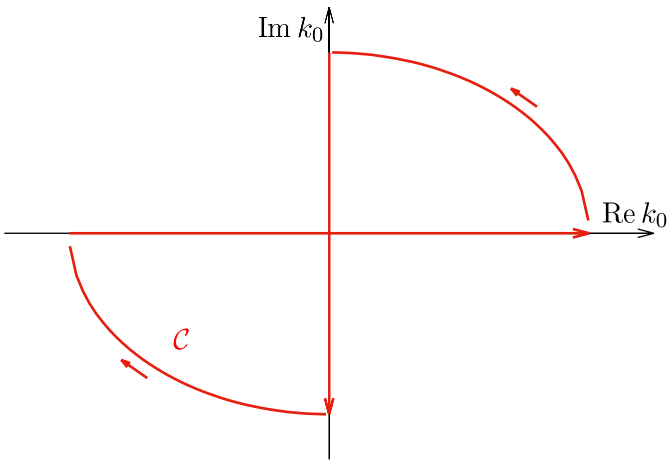

Figure C.1: Integration contour for Wick's rotation in the complex k_0 plane without poles.

The transformations are defined via Wick's rotation [55]. For a function $f(k^M) = f(\vec{k}, k_0)$ the zeroth component k_0 of the Minkowskian four vector k^M is continued from the real axis to the complex plane and a closed integration contour is specified, see the red curve in Fig. C.1. Applying Cauchy's integral (3.7) leads to

$$0 = \oint_{\mathcal{C}} f(z)dz = \left(\int_{-\infty}^{+\infty} + \int_{arch,up} + \int_{i\infty}^{-i\infty} + \int_{arch,down} \right) f(z)dz. \quad \text{(C.5)}$$

The two contributions from the the upper right arch $\int_{arch,up}$ and the lower left arch $\int_{arch,down}$ vanish, if the integrand vanishes for infinite large momenta $|z| \to \infty$ (which is the case for the tDSE and tBSE in this thesis). It follows

$$\int dk_0 \Rightarrow i \int dk_0 = - \int dk_4 \quad \text{(C.6)}$$

with $ik_0 = k_4$. In the presence of poles $k_{0,pole}$ the transformation has to be

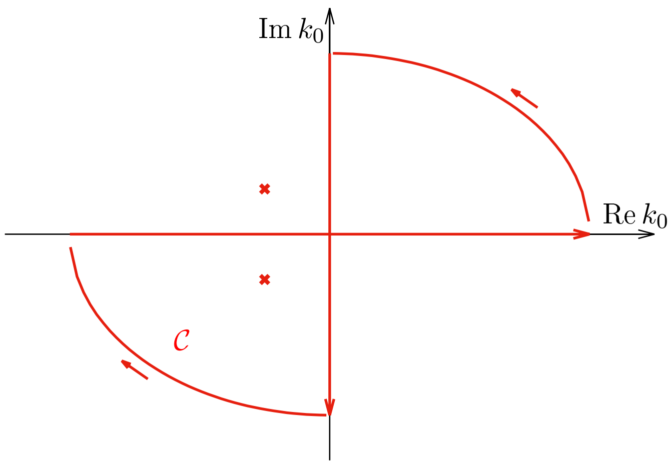

Figure C.2: Integration contour for Wick's rotation in the complex k_0 plane with two poles (red crosses).

done more carefully. The upper pole in Fig. C.2 does not contribute to the contour integral, the lower one is located inside the integration contour $\mathcal{C}$ and gives, referring to Eq. (3.8) a contribution to Eq. (C.5) and (C.6):

$$\int dk_0 f(k_0) \Rightarrow i \int dk_0 f(ik_0) + 2\pi i \ \text{res}[f(k_0 = k_{0,pole})], \quad \text{(C.7)}$$

where res$[f(k_0 = k_{0,pole})]$ is the residue of $f(k_0$ at $k_0 = k_{0,pole}$. It is not possible to change the integration contour $\mathcal{C}$ in a simple way to omit the poles and the corresponding residues.

D | Determinant function with complex arguments

For finding the determinant of a matrix $A^{n \times n}$ of dimension $n \gg 3$ it is not convenient anymore to use simply Leibniz formula. Instead a more efficient algorithm must be chosen. Then it has to be implemented or a good implementation has to be found. In this thesis the LU-decomposition [1] has been chosen and has been implemented for complex arguments. The existing C++ routines are either much too slow or they are written only for real arguments. The implemented routine has been tested with a couple of the existing routines and the results coincide.

Practical calculations show that some meson masses can be obtained with high accuracy even if the arguments of the determinant function are chosen to be real (i.e. the imaginary parts of the entries of Eq. (3.26) are neglected). Fig. D.1 illustrates that for quarkonia with $m_{q_1} = m_{q_2}$ it does not make a difference whether the determinant function (3.30) has complex arguments or only the real parts of them. Even for kaons with $m_{q_1} = 5$ MeV and $m_{q_2} = 115$ MeV the difference of both cases is only around 1 MeV. Of course, it is not exact to neglect the imaginary parts in S, but someone could guess that the meson mass results are independent of these imaginary parts by observing a couple of values in the expectable region and continues the calculations with the real parts, which may be more comfortable. Looking at the heavy-light mesons (D, D_s) shows that this does not hold anymore. For D mesons with $m_{q_1} = 5$ MeV and $m_{q_2} \approx 1000$ MeV the difference is about 100 MeV. It is interesting to note that with this "wrong" method the

[1] Each regular matrix A can be decomposed into $A = LU$, where L is a lower triangular matrix with $diag(L) = (1, 1, ..., 1, 1)$ and U is an upper triangular matrix. This decomposition is useful because $det(A) = det(LU) = det(L) \cdot det(U) = 1 \cdot det(U)$ and $det(U)$ is just the product of the elements on the diagonal of U.

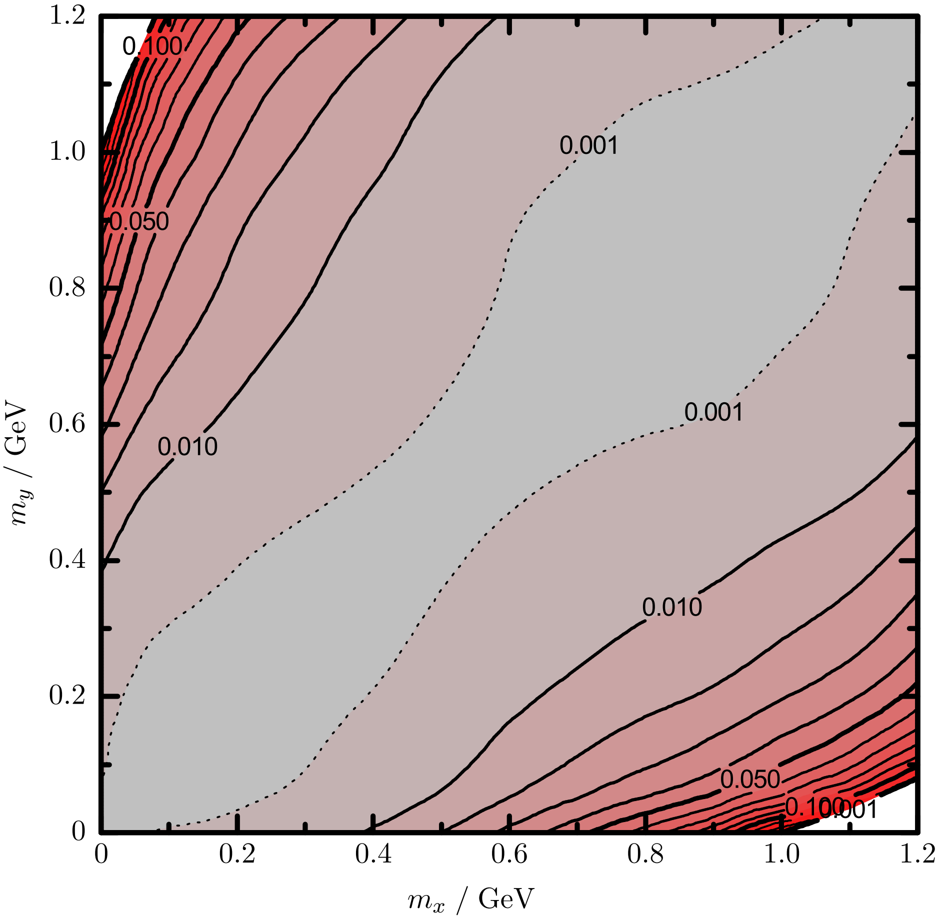

Figure D.1: Contour plot of the difference of pseudoscalar meson groundstate mass M_{xy} in units of GeV calculated once with complex arguments (see Fig. 4.1) and once only with the real parts of S from Eq. (3.28) for varying quark masses m_x and m_y. Parameters $\omega = 0.5$ GeV, $D = 16$ GeV^{-2}.

effect $M_D > M_{D_s}$ can not be observed, whether the quark masses $m_{q_{1,2}}$ are a little bit different or not. Also the values of D and D_s meson masses are closer to their experimental values. Hence, if somebody starts calculations in this manner it is hard to find out that the results are not correct if they are not explicitly tested.

E | tDSE solutions and tBSE expansion coefficients

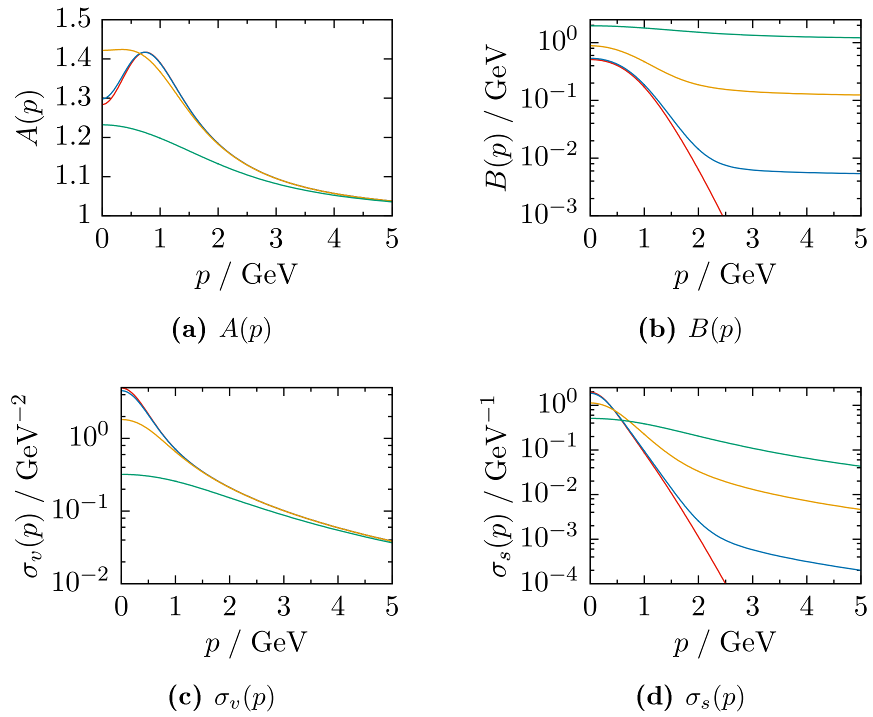

Figure E.1: Propagator functions from Eq. (3.1) and (3.2) for model parameters $\omega = 0.5\,\text{GeV}$ and $D = 16\,\text{GeV}^{-2}$, red curve: $m_q = 0\,\text{MeV}$ (chiral limit), blue curve: $m_q = 5\,\text{MeV}$, yellow curve: $m_q = 115\,\text{MeV}$, yellow curve: $m_q = 1130\,\text{MeV}$.

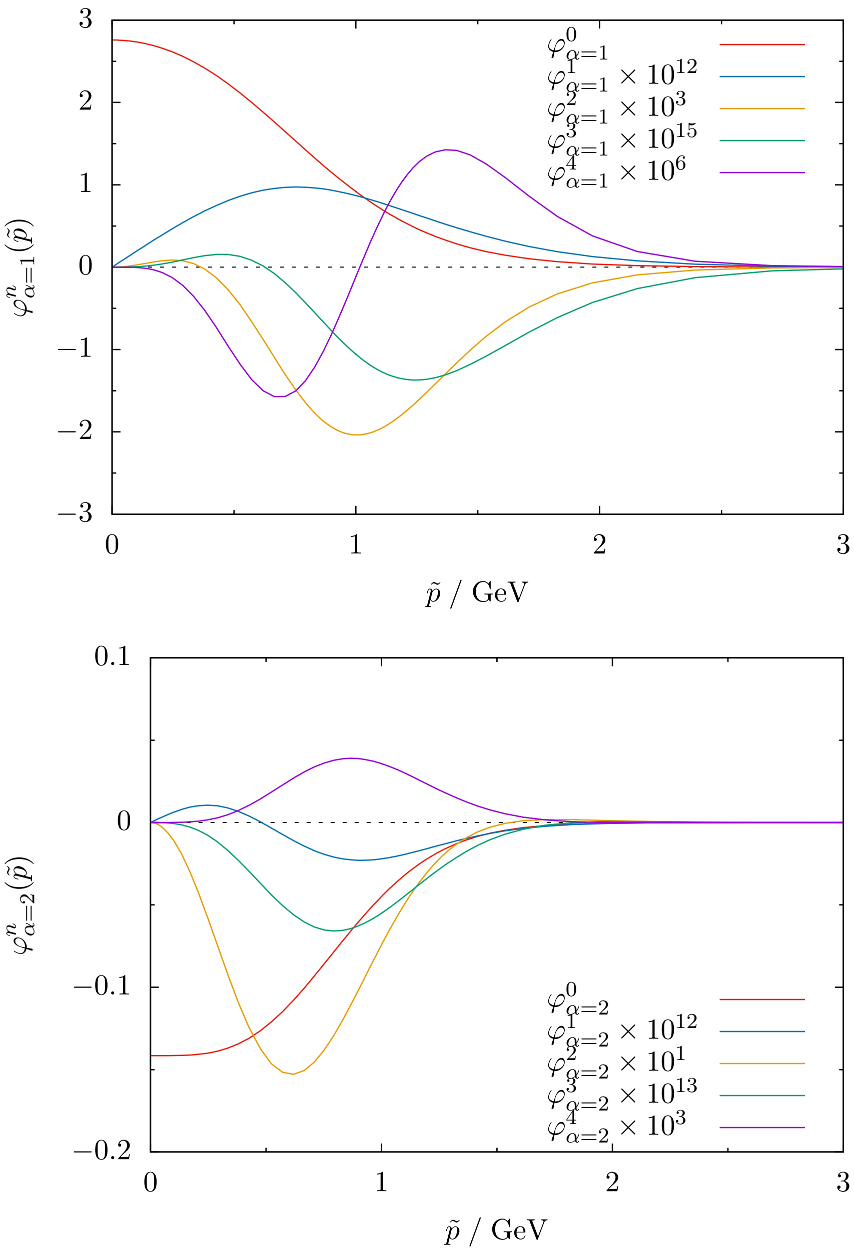

Figure E.2: Expansion coefficients $\varphi^n_\alpha(\tilde{p})$ (Eq. (3.25)) of pion ($m_q = 5\,\mathrm{MeV}$) for $\alpha = \{1, 2\}$. The model parameters are $\omega = 0.5\,\mathrm{GeV}$ and $D = 16\,\mathrm{GeV}^{-2}$.

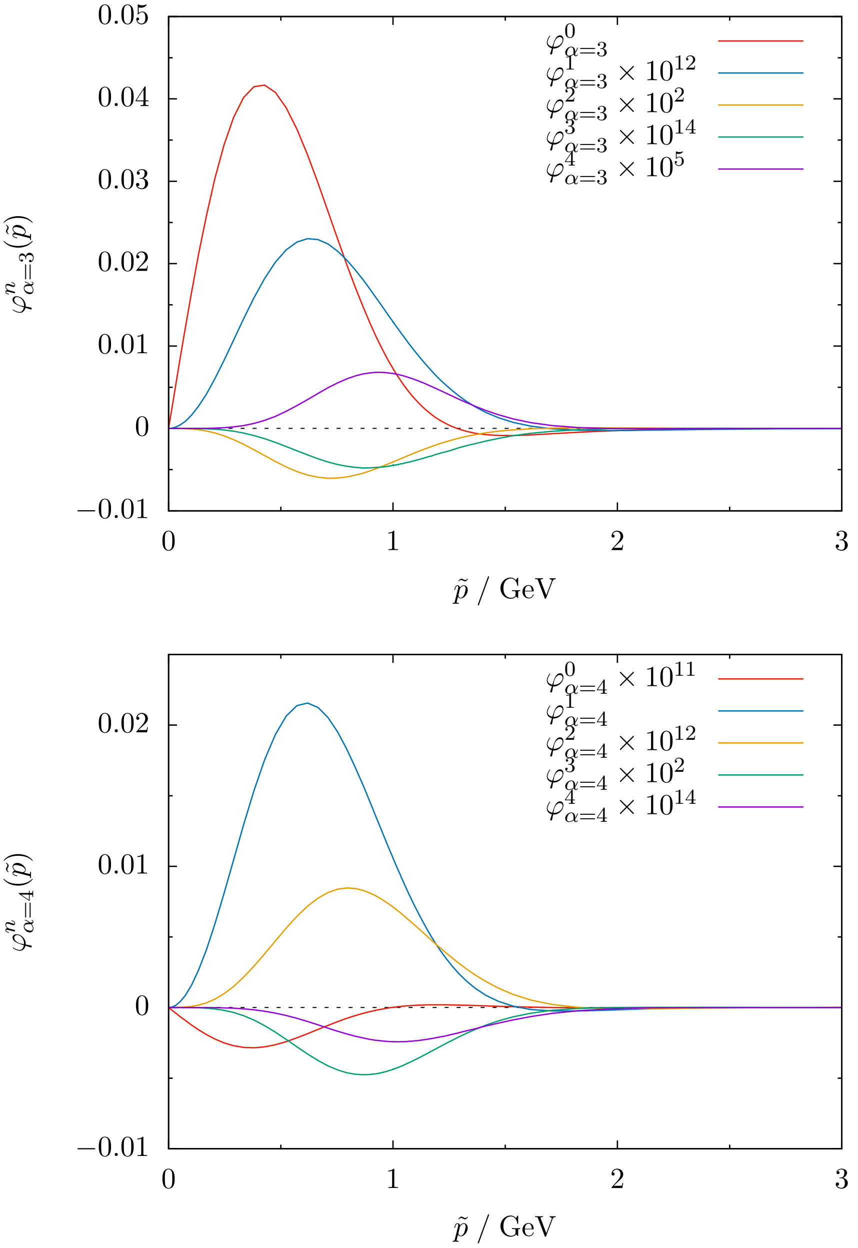

Figure E.3: As Fig. E.2 but for $\alpha = \{3, 4\}$.

List of Tables

List of Figures

Bibliography

[1] R. Alkofer, W. Detmold, C. S. Fischer, and P. Maris. Analytic properties of the Landau gauge gluon and quark propagators. *Phys. Rev.*, D70:014014, 2004.

[2] R. Alkofer, P. Watson, and H. Weigel. Mesons in a Poincare covariant Bethe-Salpeter approach. *Phys. Rev.*, D65:094026, 2002.

[3] A. Bender, C. D. Roberts, and L. Von Smekal. Goldstone theorem and diquark confinement beyond rainbow ladder approximation. *Phys. Lett.*, B380:7–12, 1996.

[4] M. Blank. *Properties of quarks and mesons in the Dyson-Schwinger/Bethe-Salpeter approach.* PhD thesis, Graz U., 2011.

[5] C. H. C.H Llewellyn-Smith. A relativistic formulation of the quark model for mesons. *Annals of Physics*, 53(3):521 – 558, 1969.

[6] L. Chang and C. D. Roberts. Sketching the Bethe-Salpeter kernel. *Phys. Rev. Lett.*, 103:081601, 2009.

[7] S. M. Dorkin, M. Beyer, S. S. Semikh, and L. P. Kaptari. Two-Fermion Bound States within the Bethe-Salpeter Approach. *Few Body Syst.*, 42:1–32, 2008.

[8] S. M. Dorkin, L. P. Kaptari, C. Ciofi degli Atti, and B. Kampfer. Solving the Bethe-Salpeter Equation in Euclidean Space. *Few Body Syst.*, 49:233–246, 2011.

[9] S. M. Dorkin, L. P. Kaptari, T. Hilger, and B. Kämpfer. Analytical properties of the quark propagator from a truncated Dyson-Schwinger equation in complex Euclidean space. *Phys. Rev.*, C89:034005, 2014.

[10] S. M. Dorkin, L. P. Kaptari, and B. Kämpfer. Accounting for the analytical properties of the quark propagator from the Dyson-Schwinger equation. *Phys. Rev.*, C91(5):055201, 2015.

[11] J. J. Dudek, R. G. Edwards, B. Joó, M. J. Peardon, D. G. Richards, and C. E. Thomas. Isoscalar meson spectroscopy from lattice qcd. *Phys. Rev. D*, 83:111502, Jun 2011.

[12] F. J. Dyson. The s matrix in quantum electrodynamics. *Phys. Rev.*, 75:1736–1755, Jun 1949.

[13] D. Ebert, R. N. Faustov, and V. O. Galkin. Mass spectra and Regge trajectories of light mesons in the relativistic quark model. *Phys. Rev.*, D79:114029, 2009.

[14] L. D. Faddeev. Scattering theory for a three particle system. *Sov. Phys. JETP*, 12:1014–1019, 1961. [Zh. Eksp. Teor. Fiz.39,1459(1960)].

[15] C. S. Fischer, S. Kubrak, and R. Williams. Mass spectra and Regge trajectories of light mesons in the Bethe-Salpeter approach. *Eur. Phys. J.*, A50:126, 2014.

[16] C. S. Fischer, S. Kubrak, and R. Williams. Spectra of heavy mesons in the Bethe-Salpeter approach. *Eur. Phys. J.*, A51:10, 2015.

[17] C. S. Fischer, P. Watson, and W. Cassing. Probing unquenching effects in the gluon polarisation in light mesons. *Phys. Rev.*, D72:094025, 2005.

[18] C. S. Fischer, P. Watson, and W. Cassing. Probing unquenching effects in the gluon polarization in light mesons. *Phys. Rev. D*, 72:094025, Nov 2005.

[19] Z. Fodor and C. Hoelbling. Light Hadron Masses from Lattice QCD. *Rev. Mod. Phys.*, 84:449, 2012.

[20] M. R. Frank and C. D. Roberts. Model gluon propagator and pion and rho meson observables. *Phys. Rev.*, C53:390–398, 1996.

[21] L. Giusti, F. Rapuano, M. Talevi, and A. Vladikas. The QCD chiral condensate from the lattice. *Nucl. Phys.*, B538:249–277, 1999.

[22] M. Gomez-Rocha, T. Hilger, and A. Krassnigg. Effects of a dressed quark-gluon vertex in pseudoscalar heavy-light mesons. *Phys. Rev.*, D92(5):054030, 2015.

[23] P. R. Graves-Morris. Fredholm Method for Bethe-Salpeter Equation. *Phys. Rev. Lett.*, 16:201–203, 1966.

[24] R. Gupta. Introduction to lattice QCD: Course. In *Probing the standard model of particle interactions. Proceedings, Summer School in Theoretical Physics, NATO Advanced Study Institute, 68th session, Les Houches, France, July 28-September 5, 1997. Pt. 1, 2*, pages 83–219, 1997.

[25] C. Gutierrez, V. Gigante, T. Frederico, G. Salmè, M. Viviani, and Lauro Tomio. Bethe–Salpeter bound-state structure in Minkowski space. *Phys. Lett.*, B759:131–137, 2016.

[26] T. Hilger. *Medium Modifications of Mesons*. PhD thesis, Dresden, Tech. U., 2012.

[27] T. Hilger and A. Krassnigg. Quasi-exotic open-flavor mesons. 2016.

[28] T. Hilger, C. Popovici, M. Gomez-Rocha, and A. Krassnigg. Spectra of heavy quarkonia in a Bethe-Salpeter-equation approach. *Phys. Rev.*, D91(3):034013, 2015.

[29] L. P. Kaptari, A. Yu. Umnikov, S. G. Bondarenko, K. Yu. Kazakov, F. C. Khanna, and B. Kämpfer. Bethe-salpeter amplitudes and static properties of the deuteron. *Phys. Rev. C*, 54:986–1005, Sep 1996.

[30] M. Knap and C. Heil. Numerische integration. `https://itp.tugraz.at/LV/sormann/NumPhysik/Skriptum/kapitel6.pdf`. Accessed: 2010-10-02.

[31] A. Krassnigg. Excited mesons in a Bethe-Salpeter approach. *PoS*, CONFINEMENT8:075, 2008.

[32] A. Krassnigg, C. D. Roberts, and S. V. Wright. Meson spectroscopy and properties using Dyson-Schwinger equations. *Int. J. Mod. Phys.*, A22:424–431, 2007.

[33] J. J. Kubis. Partial-wave analysis of spinor bethe-salpeter equations for single-particle exchange. *Phys. Rev.*, D6:547–564, 1972.

[34] S. Kubrak, C. S. Fischer, and R. Williams. Regge behaviour within the Bethe-Salpeter approach. *J. Phys. Conf. Ser.*, 599(1):012013, 2015.

[35] M. Levine, J. Tjon, and J. Wright. Nonsingular bethe-salpeter equation. *Phys. Rev. Lett.*, 16:962–964, May 1966.

[36] C. D. Maris, P.and Roberts. Pi- and K meson Bethe-Salpeter amplitudes. *Phys. Rev.*, C56:3369–3383, 1997.

[37] P. Maris, A. Raya, C. D. Roberts, and S. M. Schmidt. Facets of confinement and dynamical chiral symmetry breaking. *Eur. Phys. J.*, A18:231–235, 2003.

[38] P. Maris and C. D. Roberts. Dyson-Schwinger equations: A Tool for hadron physics. *Int. J. Mod. Phys.*, E12:297–365, 2003.

[39] P. Maris, C. D. Roberts, and P. C. Tandy. Pion mass and decay constant. *Phys. Lett.*, B420:267–273, 1998.

[40] P. Maris and P. C. Tandy. Bethe-Salpeter study of vector meson masses and decay constants. *Phys. Rev.*, C60:055214, 1999.

[41] P. Maris and P. C. Tandy. QCD modeling of hadron physics. *Nucl. Phys. Proc. Suppl.*, 161:136–152, 2006. [,136(2005)].

[42] N. Nakanishi. A General survey of the theory of the Bethe-Salpeter equation. *Prog. Theor. Phys. Suppl.*, 43:1–81, 1969.

[43] S. Narison. A fresh look into $m_{c,b}$ and precise $f_{D_(s),B_(s)}$ from heavy-light QCD spectral sum rules. *Phys. Lett.*, B718:1321–1333, 2013.

[44] K. A. Olive et al. Review of Particle Physics. *Chin. Phys.*, C38:090001, 2014.

[45] A. Pagnamenta and J. G. Taylor. Wick Rotation in the Bethe-Salpeter Equation. *Phys. Rev. Lett.*, 17:218–220, 1966.

[46] S. Qin, L. Chang, Y. Liu, C. D. Roberts, and D. J. Wilson. Interaction model for the gap equation. *Phys. Rev.*, C84:042202, 2011.

[47] C. D. Roberts. Strong QCD and Dyson-Schwinger Equations. 2012.

[48] C. D. Roberts and A. G. Williams. Dyson-Schwinger equations and their application to hadronic physics. *Prog. Part. Nucl. Phys.*, 33:477–575, 1994.

[49] E. Rojas, B. El-Bennich, and J. P. B. C. de Melo. Exciting flavored bound states. *Phys. Rev.*, D90:074025, 2014.

[50] E. E. Salpeter and H. A. Bethe. A relativistic equation for bound-state problems. *Phys. Rev.*, 84:1232–1242, Dec 1951.

[51] J. S. Schwinger. On the Green's functions of quantized fields. 1. *Proc. Nat. Acad. Sci.*, 37:452–455, 1951.

[52] J. S. Schwinger. On the Green's functions of quantized fields. 2. *Proc. Nat. Acad. Sci.*, 37:455–459, 1951.

[53] N. Souchlas. A dressed quark propagator representation in the Bethe–Salpeter description of mesons. *J. Phys.*, G37(11):115001, 2010.

[54] L. v. Smekal, A. Hauck, and R. Alkofer. A solution to coupled dyson–schwinger equations for gluons and ghosts in landau gauge. *Annals of Physics*, 267(1):1–60, 1998.

[55] G. C. Wick. Properties of bethe-salpeter wave functions. *Phys. Rev.*, 96:1124–1134, Nov 1954.

[56] R. Williams. The quark-gluon vertex in Landau gauge bound-state studies. *Eur. Phys. J.*, A51(5):57, 2015.

[57] M. J. Zuilhof and J. A. Tjon. Electromagnetic properties of the deuteron and the bethe-salpeter equation with one-boson exchange. *Phys. Rev. C*, 22:2369–2382, Dec 1980.

Danksagung

Ich möchte mich herzlich bei Prof. Dr. B. Kämpfer bedanken, der es mir ermöglichte, diese äußerst interessante Thematik zu bearbeiten und meine Masterarbeit am Helmholtz-Zentrum Dresden-Rossendorf auf diesem Gebiet anzufertigen. Ich bedanke mich weiterhin für die sehr gute Betreuung, die nützlichen richtungsweisenden Hinweise und das offene Ohr für alle meine Fragen sowie die Ermöglichung meines mehrwöchigen Gastaufenthaltes am Bogoljubov-Institut.

Besonders bedanken möchte ich mich auch bei Leonid Kaptari und Sergey Dorkin für die Einführung in die Thematik und die sehr herzliche Betreuung während meines Gastaufenthaltes am Bogoljubov-Institut. Ich bedanke mich für die vielen unermüdlichen Versuche mich in die technischen Details der Problematik einzuweisen und für die vielen daraus entstandenen Erfahrungen, die ich in die Zukunft mitnehmen kann.

Ich möchte mich auch bei Tobias N., Thomas H., Thomas B. und Uwe H. A. bedanken, für die stets schnellen und guten Antworten auf meine Fragen und die unzähligen Hinweise, die dazu beitrugen, diese Arbeit in dieser Form fertigzustellen.

Des weiteren danke ich Prof. Dr. D. Stöckinger für die Zweitkorrektur meiner Masterarbeit, der, nachdem er bereits Betreuer meiner Bachelorarbeit war, nun ein zweites Mal die von mir geschriebenen Zeilen auf Sinnhaftigkeit prüfen muss.

Ich möchte meinen Eltern für die jahrelange moralische und finanzielle Unterstützung danken und dafür, dass sie über meine ganze Kindheit hinweg den Grundstein dafür gelegt haben, heute dieses Studium mit dieser Masterarbeit erfolgreich abzuschließen.

Nicht zuletzt gilt mein Dank aber meiner Familie, die mich mit viel Verständnis und Liebe täglich am meisten unterstützt hat.

Erklärung

Hiermit versichere ich, dass ich die vorliegende Arbeit ohne unzulässige Hilfe Dritter und ohne Benutzung anderer als der angegebenen Hilfsmittel angefertigt habe. Die aus fremden Quellen direkt oder indirekt übernommenen Gedanken sind als solche kenntlich gemacht. Die Arbeit wurde bisher weder im Inland noch im Ausland in gleicher oder ähnlicher Form einer anderen Prüfungsbehörde vorgelegt.

Robert Greifenhagen
Dresden, 01.11.2016